

**SURFACELET-BASED HETEROGENEOUS MATERIALS  
MODELING**

A Dissertation  
Presented to  
The Academic Faculty

by

Wei Huang

In Partial Fulfillment  
of the Requirements for the Degree  
Doctor of Philosophy in the  
School of Mechanical Engineering

Georgia Institute of Technology  
August 2014

**COPYRIGHT 2014 BY WEI HUANG**

# **SURFACELET-BASED HETEROGENEOUS MATERIALS MODELING**

Approved by:

Dr. Yan Wang, Advisor  
School of Mechanical Engineering  
*Georgia Institute of Technology*

Dr. Edmond Chow  
School of Computational Science and  
Engineering  
*Georgia Institute of Technology*

Dr. Xiaoming Huo  
School of Industrial and Systems  
Engineering  
*Georgia Institute of Technology*

Dr. David W. Rosen  
School of Mechanical Engineering  
*Georgia Institute of Technology*

Dr. Suresh K. Sitaraman  
School of Mechanical Engineering  
*Georgia Institute of Technology*

Date Approved: [June 30, 2014]

## ACKNOWLEDGEMENTS

I would like to especially thank my advisor, Dr. Yan Wang, for offering me the opportunity to engage in this exciting research, his continuous guidance throughout my entire Ph.D study and financial support for three years and five months. Without any of these, I would not have survived through the Ph.D study or accomplished these research outputs. In addition, he always tried to train me to be a researcher instead of a student. He also always patiently taught me how to effectively write technical papers. I would never forget any of these.

I would like to thank Dr. David W. Rosen for his guidance and partial financial support for two years and five months in this National Science Foundation project. I learned a lot from the discussions with him. I also like his style of guiding students as a professor.

I would like to thank Dr. David W. Rosen, Dr. Suresh K. Sitaraman, Dr. Edmond Chow and Dr. Xiaoming Huo for serving as my committee members. Their precious comments and suggestions given during my dissertation proposal are very helpful for the improvement of this dissertation.

I would also like to acknowledge the support from the National Science Foundation throughout my Ph.D. research by Grant No. CMMI-1030385 and CMMI-1001040.

Finally, I would like to thank Georgia Tech and the George W. Woodruff School of Mechanical Engineering for providing me this world-class environment for research and study.

# TABLE OF CONTENTS

	Page
ACKNOWLEDGEMENTS	iii
LIST OF TABLES	viii
LIST OF FIGURES	ix
SUMMARY	xiv
CHAPTER 1 INTRODUCTION	1
1.1 Multi-Scale Modeling	1
1.1.1 The importance of multi-Scale modeling	1
1.1.2 Multi-scale heterogeneous material modeling	2
1.1.3 Multi-scale CAD systems	4
1.2 Key Concepts and Issues in Multi-scale Heterogeneous Material Modeling	6
1.3 The Image Representation of Material Compositions	7
1.3.1 The linear relationship between two-phase material composition and grayscale value	8
1.3.2 The image representation of multi-phase materials compositions	9
1.4 Surfacelet and Surfacelet Transform	10
1.4.1 The surfacelet	10
1.4.2 Surfacelet transform	11
1.5 Research Objective of the Dissertation	12
1.6 Detailed Tasks of the Dissertation	13
1.7 Technical Contributions	14
CHAPTER 2 RELATED WORK	16
2.1 The Surfacelet Basis	16
2.1.1 Wedgetlet, curvelet, and surflet	16
2.1.2 Surfacelet	17
2.2 Material Characterization and Image Reconstruction Methods	19

2.2.1	Radon transform and its inverse	19
2.2.2	Material characterization and image reconstruction from physical projections	20
2.2.3	Analytical algorithms for image reconstruction	24
2.2.4	Regularization of linear inverse problems	24
2.2.5	Iterative algorithms for image reconstruction	25
2.2.6	Conjugate-gradient-based iterative algorithms	28
2.3	Image-Based Feature Recognition Methods	29
2.4	Computer-Aided Heterogeneous Materials Modeling and Design Methods	30
2.4.1	Computer-aided heterogeneous materials modeling methods	30
2.4.2	Computer-aided heterogeneous materials design methods based on structure–property relations	31
2.5	Limitations of Existing Literatures in the Applications on Multi-scale Heterogeneous Materials Modeling	32
CHAPTER 3 INVERSE SURFACELET TRANSFORM		34
3.1	The Significance of Material Image Data Compression and Dimensionality Reduction	35
3.2	The General Idea of Inverse Surfacelet Transform	36
3.3	The Inverse Surfacelet Transform without Constraints	38
3.4	The Inverse Surfacelet Transform with Constraints	39
3.4.1	General procedure of inverse surfacelet transform with constraints	39
3.4.2	Inverse surfacelet transform with soft constraints	42
3.4.3	Inverse surfacelet transform with rigid constraints	42
3.4.4	Inverse surfacelet transform with semi-rigid constraints	44
3.5	Examples And Results	45
3.5.1	Without Constraints	47
3.5.2	With Constraints	49
3.5.3	Semi-rigid constraints	56
3.6	Evaluation and Comparison	59

3.7	Conclusion and Future Work	61
CHAPTER 4 COMPOSITE SURFACELETS		63
4.1	Cubic Surfacelet	64
4.1.1	The construction of a cubic surfacelet	64
4.1.2	The derivation of the cubic implicit surface function with three dimensional translation and rotation	67
4.2	V-joint Surfacelet	70
4.3	Feature Identification with the Cubic and V-joint Surfacelets	73
4.3.1	Feature identification with the cubic surfacelet	74
4.3.2	Feature identification with the v-joint surfacelet	75
4.4	Demonstrations and Results	79
4.4.1	Cubic surfacelet to identify nano-C60 particles	80
4.4.2	V-joint surfacelet to identify Al <sub>2</sub> O <sub>3</sub> -Fe composite	84
4.5	The Improvement of Surfacelet Location Evaluation based on the Consideration of Pixel Variation	90
4.5.1	The implementation with the original AFM image	95
4.5.2	The implementation with the contrast-increased AFM image	108
4.5.3	The implementation with the contrast-increased AFM image and different surfacelet shape parameters	110
4.5.4	Conclusion of comparison results of the three formulas	112
4.6	Conclusion and Future Work	114
CHAPTER 5 APPLICATION OF SURFACELETS IN MATERIALS MODELING		116
5.1	The General Procedure of Approximating Material Composition or Local Property Distributions with Surfacelets	118
5.2	The Wavelet Transform	119
5.3	An Example and Results	120
5.4	Analysis of the Result Accuracy	125
5.5	Discussions and Future Extensions	126

CHATPER 6 A MULTI-SCALE MATERIALS DESIGN METHOD WITH SEAMLESS ZOOMING CAPABILITY	128
6.1 The Collocation Method for Zoom-in Operation	132
6.1.1 Interpolation and extrapolation in the surfacelet space	132
6.1.2 Collocation for zoom-in and zoom-out operations	138
6.2 Multi-scale Materials Design Process	146
6.2.1 The combination of the distribution model in the surfacelet space and the visualization model in the image space	146
6.2.2 Detailed design steps	146
6.3 Examples and Results	149
6.3.1 Bi-sectional grid	149
6.3.2 Golden-ratio grid	161
6.4 A Property-Oriented Materials Design Process based on the Proposed Specification Scheme	165
6.4.1 The general process of property-oriented materials design	166
6.4.2 Prediction of effective physical properties of heterogeneous materials	168
6.5 Discussions and Future Work	171
CHATPER 7 CONCLUSION AND FUTURE WORK	174
7.1 Summary of the Dissertation	174
7.2 Contributions of the Dissertation	175
7.3 Future Work	176
7.3.1 Further image compression based on the feasibility of interpolation and extrapolation in the surfacelet space	176
7.3.2 Multiscale material modeling with multiscale wavelet approximation	176
REFERENCES	178
VITA	185

## LIST OF TABLES

	Page
Table 1 Rigid constrained conjugate gradient algorithm	43
Table 2 The comparison among different methods	60
Table 3 Measure properties of the datum boundary	94
Table 4 Measure properties for Figure 48(f)	96
Table 5 Measure properties for Figure 49(f)	97
Table 6 Measure properties for Figure 50(f)	99
Table 7 Measure properties for Figure 50(g)	99
Table 8 Measure properties for Figure 53(e)	101
Table 9 Measure properties for Figure 53(f)	101
Table 10 Measure properties for Figure 54(e)	102
Table 11 Measure properties for Figure 54(f)	102
Table 12 Measure properties for Figure 57(g)	105
Table 13 Measure properties for Figure 57(h)	106
Table 14 Measure properties for Figure 59(e)	107
Table 15 Measure properties for Figure 64(a)	111
Table 16 Measure properties for Figure 64(c)	111
Table 17 The resulting errors between the surfacelet model and the original values for different wavelet transforms	126
Table 18 Pixel values of the box region indicated in Figure 96	160
Table 19 Existing analytical models for effective properties of two-component materials	170



## LIST OF FIGURES

	Page
Figure 1 The materials innovation infrastructure in the Material Genome Initiative [1]	3
Figure 2 Olson's three-link chain model of the central paradigm of materials science and engineering [2]	4
Figure 3 The future CAD scheme with Multi-Scale Heterogeneous Material Modeling	5
Figure 4 The illustration of material microstructure and composition	7
Figure 5 A pixel grayscale of the fiber represents the averaged sub-grayscales of all details in the region that covers [3]	9
Figure 6 The representation of compositions of three materials by the relative compositions of every two materials	10
Figure 7 The process of surfacelet transform	11
Figure 8 The structure of the tasks for multiscale heterogeneous materials modeling	14
Figure 9 Geometric interpretation of surfacelets	18
Figure 10 Examples of microstructural data that can be obtained with synchrotron X-ray methods	22
Figure 11 3D reconstruction of the austenite phase in a commercial austenitic stainless steel alloy AL-6XN [25].	23
Figure 12 The process of coupled surfacelet transform and inverse surfacelet transform	35
Figure 13 The full and down-sized images of nano-fiber composites	46
Figure 14 The original nine slices of the 3D image of nano-fiber composites for reconstruction	47
Figure 15 The full reconstruction result with the least-square method. The error is $e=0$ .	48
Figure 16 The full reconstruction result with the conjugate gradient method. The error is $e=0$ .	49
Figure 17 The cylindrical surfacelet overlapped with a fiber surface has the maximum integral	50
Figure 18 The reconstruction results of soft boundary constraints with the least-square method (first slices only)	52
Figure 19 The reconstruction results of soft boundary constraints with the conjugate gradient method (first slices only)	52
Figure 20 The reconstruction results of soft fiber boundary and inner constraints (first slices only)	53

Figure 21 The reconstruction results of rigid fiber boundary constraints (first slices only)	54
Figure 22 The full reconstruction result of rigid fiber boundary constraints in the case of $Q=25 \times 25 \times 3=1875$ . The error is $e=13.2$ .	55
Figure 23 The reconstruction results of rigid fiber boundary and inner constraints (first slices only)	55
Figure 24 The full reconstruction result of semi-rigid constraints with penalty weights for boundary pixels equal to $1 \times 10^{10}$ and for inner pixels equal to 10. The error is $e=13.2$ .	57
Figure 25 The full reconstruction result of semi-rigid constraints with penalty weights for boundary pixels equal to $1 \times 10^{10}$ and for inner pixels equal to $1 \times 10^3$ . The error is $e=12.9$ .	58
Figure 26 The full reconstruction result of semi-rigid constraints with penalty weights for both boundary and inner pixels equal to $1 \times 10^{10}$ . The error is $e=16.5$ .	59
Figure 27 The reconstruction results of Quasi-Newton method with line search with fiber boundary constraints (first slices only)	60
Figure 28 The scheme for the construction of the cubic surfacelet from three sets of two parallel ridgelets perpendicular to x-, y-, and z-axis	64
Figure 29 The construction of a column along z-axis with rectangular cross-section from two sets of two parallel planes in x- and y- axis	66
Figure 30 The three dimensional translation and rotation of a cubic implicit surface	67
Figure 31 Microstructure of $Al_2O_3$ and $Al_2O_3$ -Fe composites [109]	71
Figure 32 The construction of v-joint composite surfacelet based on two cubic surfacelets composites	73
Figure 33 Graphic illustration of the feature identification process with the v-joint surfacelet	78
Figure 34 The process of the feature identification with the v-joint surfacelet	79
Figure 35 The 3D images of nano-C60 particle	81
Figure 36 Identifying a rectangular feature with a cubic surfacelet with matching shape parameters	82
Figure 37 Identifying rectangular features with cubic surfacelets in smaller size	83
Figure 38 Image reconstruction results with different constraints of cubic surfacelets	84
Figure 39 The two example images of $Al_2O_3$ -Fe composites for testing the v-joint surfacelet	85
Figure 40 Features identified after STEP 1, with different numbers of largest integrals	86
Figure 41 The intermediate results during the process of the feature identification	87
Figure 42 The identification result for the image with multiple grains	87

Figure 43 The identification result with thickness recognition for the image with one grain	88
Figure 44 The identification result with thickness recognition for the image with multiple grains	88
Figure 45 The original AFM image of carbon fiber reinforced polymer composites (CFRPs) and the one with increased contrast	91
Figure 46 The results of different boundary recognition methods	93
Figure 47 The calculation of the geometric properties of the datum boundary for comparison	95
Figure 48 Feature identification results when $w = 10$	96
Figure 49 Feature identification results when $w = 10^3$	97
Figure 50 Feature identification results when $w = 10^5$	98
Figure 51 Feature identification results when $w = 10^{10}$	99
Figure 52 Feature identification results when $w = 10^{15}$	100
Figure 53 Feature identification results when $w = 10$	101
Figure 54 Feature identification results when $w = 10^3$	102
Figure 55 Feature identification results when $w = 10^5$	103
Figure 56 Feature identification results when $w = 10$	104
Figure 57 Feature identification results when $w = 10^3$	105
Figure 58 Feature identification results when $w = 10$	106
Figure 59 Feature identification results when $d=1$	107
Figure 60 Feature identification results when $d=4$	108
Figure 61 Feature identification results when $d=6$	108
Figure 62 Feature identification results when $w = 10$	109
Figure 63 Feature identification results when $d=1$	110
Figure 64 Feature identification results when $w = 10$	111
Figure 65 Feature identification results when $w = 10^3$	112
Figure 66 Feature identification results when $w = 10^{10}$	112
Figure 67 The best feature identification result, when $t' = t - 10^3 \times \sqrt{\frac{1}{N} \sum_{i=1}^N (v_i - \delta)^2}$ with the largest 1800 integrals compared to result without considering the gradient information	113
Figure 68 The isotropic distribution of property along the radius directions of the material	117

Figure 69 The general procedure of approximating material composition or local property distributions with surfacelets	119
Figure 70 The discrete storage modulus data along the straight line indicated in Figure 68	121
Figure 71 The wavelet transformation results for the discrete storage modulus data shown in Figure 70	122
Figure 72 The 2D distribution in the middle plane of the surfacelet model from Mexican hat wavelet with 25 data points	123
Figure 73 The 2D distribution in the middle plane of the surfacelet model from Mexican hat wavelet with 50 data points	123
Figure 74 The 2D distribution in the middle plane of the surfacelet model from Beta wavelet with 25 data points	124
Figure 75 The 2D distribution in the middle plane of the surfacelet model from Beta wavelet with 50 data points	124
Figure 76 The derivation of the storage modulus values	125
Figure 77 The general procedure of the proposed materials specification method	130
Figure 78 An example 3D image of fiber-based composite	133
Figure 79 Result of cubic spline interpolation for parameter $\alpha$	135
Figure 80 Result of piecewise cubic Hermite interpolating polynomial for parameter $\alpha$	136
Figure 81 Result of cubic spline interpolation for parameter $\mu$	137
Figure 82 Result of 2D cubic spline interpolation for parameter $\mu$ and $\alpha$	138
Figure 83 Determination of the levels of collocation points	140
Figure 84 1D and 2D zoom-in examples	142
Figure 85 The illustration of golden ratio	145
Figure 86 Comparison between uniform and golden ratio grid in zoom-in operations for 2D and 3D domains	145
Figure 87 The general procedure of the computer-aided material microstructure design process	149
Figure 88 The specification result of locations and orientations of the three fibers in the surfacelet domain at STEP 2	152
Figure 89 The result of inverse surfacelet transform at STEP 3 (the size of the 3D image is $20 \times 20 \times 9$ )	153
Figure 90 The first slice of the resulting image of inverse surfacelet transform at Step 3 with enhanced resolution (the size is $50 \times 50 \times 9$ )	153
Figure 91 Zoom-in and details design of fiber-matrix interphase	155
Figure 92 The full resulting 3D image of STEP 4	156

Figure 93 The full reconstructed 3D image of the resulting surfacelets in STEP 5	157
Figure 94 The result of STEP 5	158
Figure 95 The result of STEP 7	158
Figure 96 The image reconstruction result in STEP 8	160
Figure 97 The resulting image of the zoom-out operation (the first slice only)	161
Figure 98 The user-specified isosurfaces for an ellipsoidal particle	163
Figure 99 The user-specified isosurfaces in the surfacelet space with golden-ratio grids	164
Figure 100 The interpolation of surface integrals with golden-ratio grids	164
Figure 101 The resulting image of the specification process	165
Figure 102 A property-oriented materials design process	167
Figure 103 The reverse engineering of the design process	168
Figure 104 The FEA mesh of an example 3D material image designed with the proposed method in this chapter	173

## SUMMARY

The application of heterogeneous materials has become common in modern product design such as composites and porous media. Computational design tools for such materials, with higher complexity than the traditional homogeneous ones, will be a critical component in the realization of the heterogeneity systematically. It is foreseen that computer-aided design (CAD) systems will include computer-aided materials design modules in future so that the design of functional materials and structures can be integrated for optimal product design. The traditional CAD systems model three-dimensional (3D) geometry at macro-scales with boundary representation (B-Rep), whereas computer-aided materials design is concerned with the specification of material composition at scales ranging from nano-, meso-, to micro-. Thus, multi-scale CAD systems are desirable for the integration of product and materials information. The existing B-Rep based modeling scheme needs to be extended to incorporate heterogeneous material compositions. The new modeling scheme should also support seamless zoom-in and zoom-out operations in multi-scale CAD systems.

Recently, a multi-scale model, dual-Rep, was proposed to represent geometry and material property distribution implicitly. The core part of dual-Rep is a new basis function called surfacelet. Surfacelet is able to represent boundary information more efficiently than the traditional wavelets, while keeping a unified form with wavelets so that the role exchange of boundary and internal structures during zooming operations is enabled. A surfacelet transform is able to represent microstructure distributions in 3D images with surfacelet coefficients. In this dissertation, three enabling techniques for

surfacelet-based heterogeneous materials modeling are developed. First, a method of inverse surfacelet transform is developed such that the original images can be reconstructed from the surfacelet coefficients. The surface integrals of voxel (i.e., volumetric pixel) values are obtained from the surfacelet coefficients using the one-dimensional inverse wavelet transform. The images are then reconstructed by solving linear equations from discretized surface integrals. The prior knowledge of material properties and distributions is applied to solve the under-constrained problems. Second, composite surfacelets with the combinations of different types of primitive surfacelets are created to increase the flexibility of the surfacelet transform with potentially fewer surfacelets and improved reconstruction accuracy. Third, a multi-scale materials modeling method is proposed to support interactive design and visualization of material microstructures at multiple levels of details. It has the capability to support seamless zoom-in and zoom-out. This method provides a feature-based design approach based on the surfacelet basis.

# CHAPTER 1

## INTRODUCTION

### *1.1 Multi-Scale Modeling*

#### **1.1.1 The importance of multi-Scale modeling**

Almost all of the problems in science and engineering are multi-scale in nature. Objects are made up of atoms and molecules at the atomistic scale, whereas their measurable geometric dimensions are usually at some length scale of a few orders larger. Similarly, atomic events occur at the time scale of femto-seconds ( $10^{-15}$  second), whereas the events of engineering interest typically take place at scales of orders of magnitude slower. In the context of multi-scale modeling, we usually refer to the macroscopic scale as the largest scale at which the overall properties and performances that are the most important to us. The smaller scales are referred to as microscopic scales. Although engineers are mostly interested in the objects or events at macroscopic scales, in some cases, understanding the detailed information locally at microscopic scales can help us to achieve the desirable macroscopic performances in a fundamental way. However, modeling the entire objects or events at the smallest scale with the most detailed information we want to understand and tweak is too complex and computationally expensive. Furthermore, the most detailed information about those uninteresting portions of objects or time periods is redundant. More importantly, the overall picture of the problem is easily lost at the smallest scale with the abundant and big data.

Therefore, a scheme that can simultaneously model the objects or events at both macroscopic and microscopic scales is needed. This is where multi-scale modeling comes in. By coupling macroscopic and microscopic models, we hope to take advantage of both



the simplicity and efficiency of the macroscopic models, as well as the accuracy of the microscopic models.

### **1.1.2 Multi-scale heterogeneous material modeling**

Among all scientific problems, the multi-scale modeling scheme is especially important in materials design, since designing materials for targeted performances requires multiple levels of information on material structures and compositions. Before the emergence of nanotechnology, multi-scale modeling was not as important for materials design as today. The reason is that, traditionally, new material properties were designed based on trying different processing methods. As a result, the microscopic structures and compositions were uniform, and we were not able to change them locally. In such cases, the materials are called “homogeneous”. However, with the advent of the nanotechnology, materials can be designed and realized a more flexible manner. Heterogeneous materials with more complex compositions and properties become available.

The government of the United States launched the Material Genome Initiative (MGI) [1] in June 2011, aimed at developing a materials innovation infrastructure to accelerate advanced materials discovery and deployment in the United States. The structure of this materials innovation infrastructure is shown in Figure 1, which includes:

*Computational tools:* software for predictive modeling, simulation, design and exploration

*Experimental tools:* synthesis and processing; quantitative characterization and analytic tools; accelerated testing and rapid prototyping; techniques to validate and advance materials theory

*Digital data*: data and interoperability standards for material properties; advanced data mining, analytic tools and open/proprietary data warehouses

*Collaborative networks*: integrated centers in computation, data informatics and experimentation; sharing of best practices across disparate centers via formal and informal networking; educational materials for the next generation workforce; public/private partnerships.

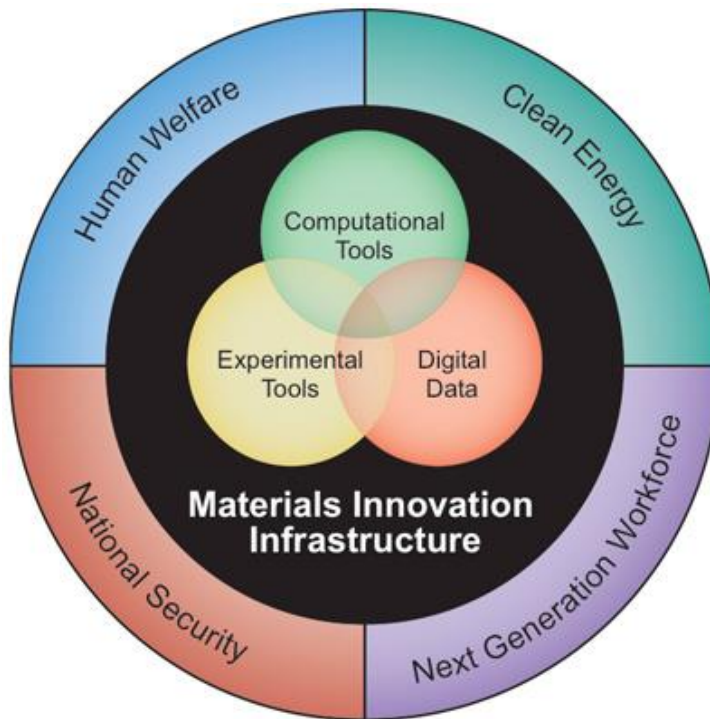


Figure 1 The materials innovation infrastructure in the Material Genome Initiative [1]

This dissertation is aimed at providing a fundamental methodology of material modeling and design that falls into the categories of *Computational Tools* and *Digital Data* in materials innovation infrastructure of MGI.

The concept of computational design of materials was proposed almost two decades ago. In 1997, Olson [2] proposed a top-down, goal-oriented material design strategy, as shown in Figure 2. This method is aimed at establishing the process-

structure–property–performance relations. In such strategy, material structure and composition are modeled at multiple scales.

The purpose of the proposed multi-scale materials design method in this dissertation is for the ease of structure–property relation construction, as indicated in Figure 2.

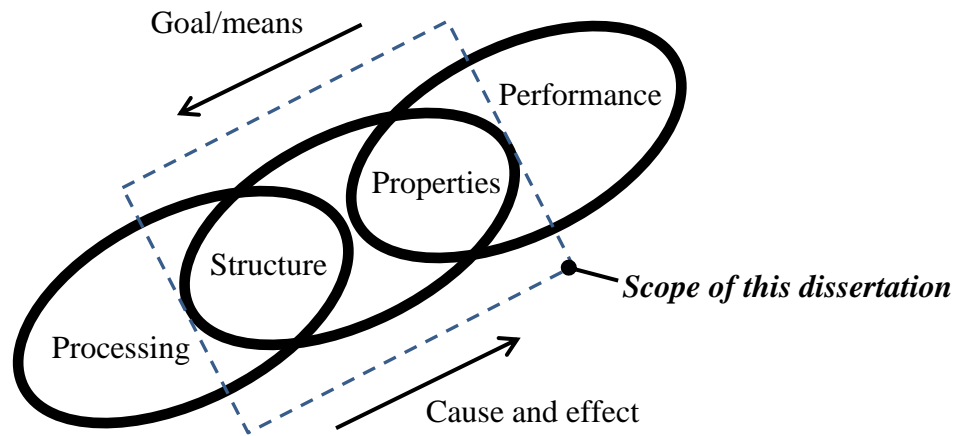


Figure 2 Olson's three-link chain model of the central paradigm of materials science and engineering [2]

### 1.1.3 Multi-scale CAD systems

In recent years, due to the high demand of functional materials in product design, the application of complex heterogeneous materials is becoming common. Computer-aided materials design has become a critical component in the realization of complex heterogeneity. It can be foreseen that, in future, computer-aided design (CAD) systems will include the computer-aided materials design modules so that the design of microscopic structures and materials can be integrated with macroscopic geometry for optimal product design, as illustrated in Figure 3. Within the same CAD systems, users can perform zoom-in and zoom-out operations to view and model at multiple scales.

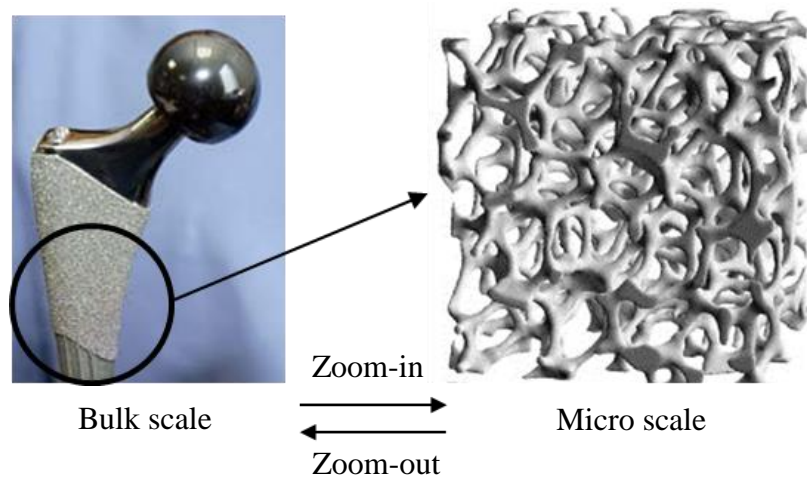


Figure 3 The future CAD scheme with Multi-Scale Heterogeneous Material Modeling

While traditional CAD systems only deal with the geometry in macro-scales or bulk scales ( $>10^{-3}$  m), computer-aided materials design deals with the specification of material compositions at scales ranging from nano- ( $10^{-9}\sim 10^{-8}$  m), meso- ( $\sim 10^{-7}$  m), micro- ( $10^{-6}\sim 10^{-4}$  m), to macro-scales. Accordingly, the future CAD systems are called multi-scale CAD systems, because the systems can not only define the product geometry and material property distribution in as large as macro-scales, but also capture the most detailed material compositions in as small as nano-scales.

Different from the traditional CAD systems, in multi-scale CAD systems, the specification of material composition distributions is as important as microscopic structures. The dependency of material properties on microscopic structures is more evident at nano-scales because the geometry and material property are one-to-one correspondent to each other.

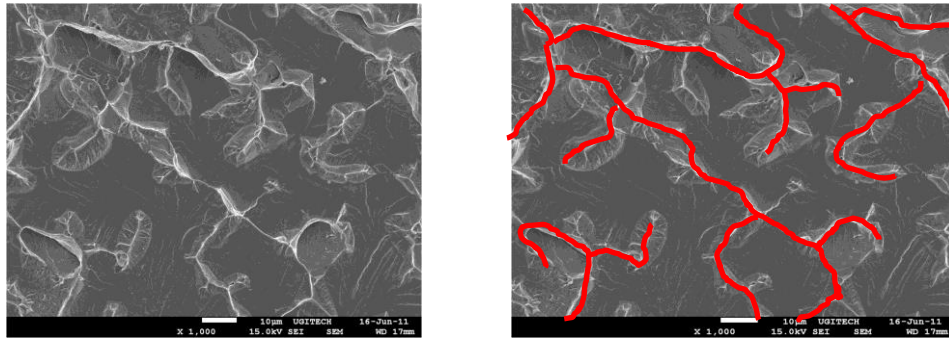
## ***1.2 Key Concepts and Issues in Multi-scale Heterogeneous Material Modeling***

Because the overall material properties can be affected by the details of microstructures and compositions at all scales, materials modeling modules in multi-scale CAD systems should support multi-scale modeling for design specifications across multiple scales. Material properties are mainly determined by material microstructures and compositions. Therefore, multi-scale materials modeling for the purpose of materials design is the major enabling technology to engineer materials. In heterogeneous materials, the microstructure is the network of boundaries between different grains or lattices, or sharp change of material compositions, as shown in Figure 4(b). Here, the term microstructure does not particularly refer to the internal material structures at the micrometer scale only, but to those at any scales that are suitable for describing material distributions. Microstructures can strongly influence the overall physical properties of a material, such as strength, ductility, hardness, toughness, wear and corrosion resistance, thermal behavior, and etc.

Material composition refers to the continuous material domains with the microstructure as its boundaries. It also plays an important role in the determination of physical properties of a material. The design of material microstructure forms the basis for the design of material composition. As the material microstructure defines the ‘skeleton’ or major material distributions, the material composition is more like the ‘flesh and skin’ in addition to the microstructural information. That is, compositions depend on structures. Take the fiber-based composite as an example. The positions and orientations of the fibers define the microstructure and outline the overall distribution of materials,

whereas the material composition information in the regions of fibers, matrix and the fiber-matrix interphases follow the overall trend defined by the fiber microstructures. Therefore, the core of multi-scale materials modeling is multi-scale microstructural modeling.

In the traditional bulk-scale geometric modeling, features are widely used to define geometries. In the domain of material microstructures, microstructures also show some patterns. Therefore, most of the microstructural information can be modeled by highlighting these patterns. These patterns are called microstructural features. The microstructural features are important in determining the material properties. Thus, how to effectively utilize microstructural features in materials design is key in multi-scale materials modeling.



(a) SEM image

(b) Illustration of material microstructure

Figure 4 The illustration of material microstructure and composition

### ***1.3 The Image Representation of Material Compositions***

Different from the classic geometric modeling, heterogeneous materials modeling uses material images as the essential medium for both design and reverse engineering processes. Images of either material microstructures (optical or scanning electron microscope) or characterized properties have the most comprehensive and basic data about the materials. They also provide visual information of materials for engineers. As a

result, it is a common practice that in the reverse engineering process, material models are constructed from the images. On the other hand, in the materials design process, images constructed based on some underlying material models can also help engineers to visualize their design concepts during the process. Heterogeneous materials modeling typically uses grayscale images. In photography, a grayscale image is an image in which the value of each pixel shows the intensity information. Grayscale images are also known as black-and-white, varying from black at the weakest intensity to white at the strongest.

In this section, how material images represent material compositions is introduced. The grayscale image representation principles for two-phase materials and multi-phase materials are introduced in Section 1.3.1 and Section 1.3.2 respectively.

### **1.3.1 The linear relationship between two-phase material composition and grayscale value**

Since the brightness of pixels in an image varies when it captures two different materials such as in alloys and composites, the grayscale value of a pixel in a material image is able to give us the information of the material composition ratio at that location. However, this is true only for two-phase materials. The grayscale value of each pixel in the material image is linearly dependent on the material compositions or the volume or mass fraction of each material. Images of materials can be taken from multiple scales with different resolutions. The grayscale value of each image pixel at the higher scale is the average of the sub-grayscales of all details at the lower scale in the region that the pixel covers, as shown in Figure 5. If the grayscale pixel value is regarded as the composition, the pixel value at the higher scale is related to the ones at the lower scale by a linear combination relationship as

$$c = \Phi_1 \times a + \Phi_2 \times b;$$

where  $\Phi_1$  and  $\Phi_2$  are the mass or volume percentages of materials 1 and 2 respectively and  $\Phi_1 + \Phi_2 = 1$ ,  $a$  and  $b$  are the corresponding pixel values of the two materials in the lower scale image, and  $c$  is the pixel value in the higher scale image.

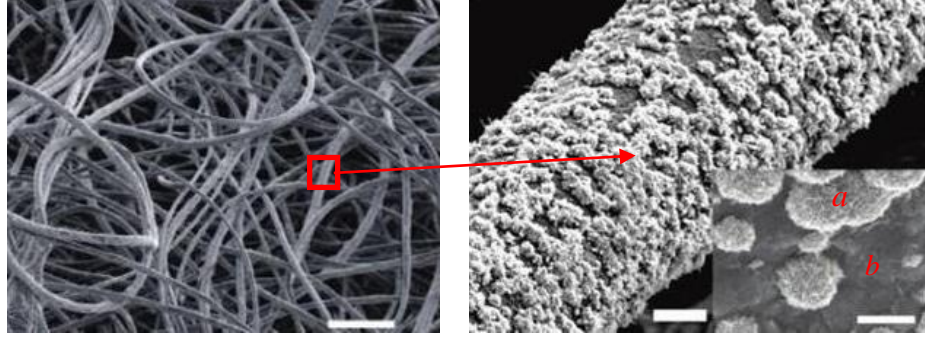


Figure 5 A pixel grayscale of the fiber represents the averaged sub-grayscales of all details in the region that covers [3]

### 1.3.2 The image representation of multi-phase materials compositions

The image representation of compositions of multi-phase materials (materials with more than two material components) is based on the separate representation of the relative compositions of every two materials. Suppose there are three materials,  $\Phi_1$  is the mass percentage of material 1,  $\Phi_2$  is the mass percentage of material 2, and  $\Phi_3$  is the mass percentage of material 3. By surfacelet modeling, the relative compositions of material 1 and 2, and of material 1 and 3 can be modeled. Therefore, it can be obtained that

$$\Phi_1 / \Phi_2 = a$$

and



$$\Phi_1 / \Phi_3 = b$$

Then the compositions of all three materials can be obtained from  $\Phi_1 / \Phi_2 / \Phi_3 = a$   
 $b / b / a$ . The graphic illustration is shown in Figure 6.

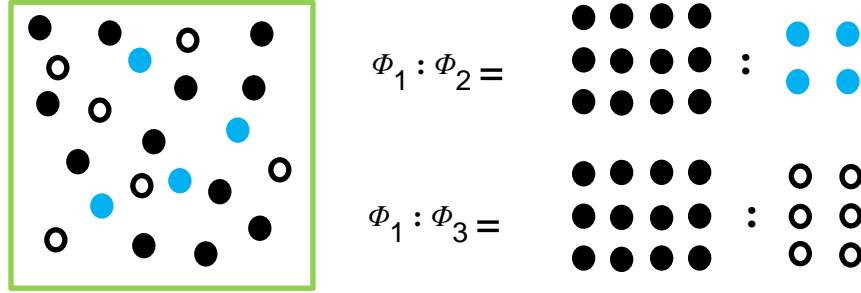


Figure 6 The representation of compositions of three materials by the relative compositions of every two materials

## 1.4 Surfacelet and Surfacelet Transform

It has been explained in Section 1.2 that the design of material microstructure forms the basis for the design of material composition. Both material microstructure and material composition play important roles in the determination of physical properties of a material. Therefore, in multi-scale heterogeneous material modeling, a basis function, which can effectively and simultaneously represent both microstructures and compositions, is desired.

### 1.4.1 The surfacelet

Wang & Rosen [4] proposed a so-called *dual representation* (dual-Rep) modeling approach. The core part of dual-Rep is a new basis function called surfacelet. A surfacelet is the combination of an implicit surface and a wavelet function. It is a 3D domain with wavelet distribution in the surface normal direction. The 3D surfacelet model is able to represent geometric boundary information or surface singularities more efficiently than

the wavelets, while keeping a unified form with wavelets. Since wavelet basis functions are better at modeling continuous distributions, a combination of wavelet and surfacelet basis functions is able to efficiently capture the boundary and internal structures at the same time. In addition, wavelet basis functions are multi-scale by nature: at larger scales, less wavelets are used for approximation with lower accuracy to show less detailed or global distribution; whereas, at smaller scales, more wavelets are used for approximation with higher accuracy to show more detailed or local distribution. Therefore, surfacelet is a good candidate for multi-scale material modeling.

The details of surfacelet will be introduced in Section 2.1.2.

### 1.4.2 Surfacelet transform

In general, the surfacelet transform is the 1D wavelet transform of the surface integrals. As shown in Figure 7, from a 3D materials distribution, the surface integrals on surfacelets are calculated and arranged in a 3D matrix with orientation parameters  $\alpha$  and  $\beta$ , and position parameter  $\mu$  as indices. Then 1D wavelet transforms along the  $\mu$  axis direction are performed for all  $\alpha$ 's and  $\beta$ 's. The results are surfacelet coefficients for a particular angle.

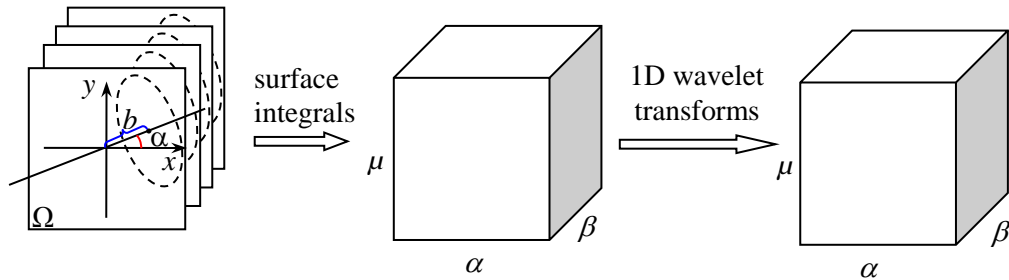


Figure 7 The process of surfacelet transform

The surfacelet transform constructs the surfacelet model from images. The reconstruction of the original material images during the heterogeneous materials design process is also desirable so that the generated material distribution before physical experiments can be visualized. In other words, the method of inverse surfacelet transform is needed. As shown in Figure 7, the surface integrals can be directly obtained from the surfacelet coefficients via the inverse 1D wavelet transform. However, it is not as straightforward to retrieve the individual image pixel values from the surface integrals. In this dissertation, numerical algorithms are proposed to calculate individual image pixel values from surface integrals by solving the constrained least-squared-error problems based on an iterative scheme.

### ***1.5 Research Objective of the Dissertation***

The overall goal of this dissertation is to provide the multi-scale modeling and design methodologies for microstructure and continuous distributions of materials. These achievements will provide the foundation of a unified tool that design engineers, analysts, manufacturers, materials scientists, and others can all use, and enable an integrated CAD/CAE/CAM environment where every artifact that is designed is physically meaningful. By having heterogeneous material models integrated into CAD, the foundation is established for engineering design, analysis, and manufacturing to be performed with a common model that respects the physics of the constituent materials. This integration will consequently enhance the scientific and technological understanding of the future CAD systems.

## ***1.6 Detailed Tasks of the Dissertation***

To achieve the research objective, four research tasks are conducted as enabling techniques of surfacelet-based heterogeneous materials modeling are developed for computer-aided materials design in future CAD systems. These four tasks are *inverse surfacelet transform*, *composite surfacelets*, *the application of surfacelets on material distribution modeling*, and *a multi-scale materials design process with seamless zooming capability* respectively. The structure of the tasks is shown in Figure 8. All of the four tasks are utilizing the transform basis or the implicit surface aspect of surfacelets. The tasks 3, which is the application of the surfacelet in materials modeling, is developed based on the combination of techniques of task 1 (the inverse surfacelet transform) and task 2 (composite surfacelets), with the approximation basis or the wavelet aspect of surfacelets.

In the following chapters of this dissertation, the four tasks will be developed. First of all, the background and related work will be introduced in Chapter 2. Second, the method of inverse surfacelet transform is developed such that the original images can be reconstructed from the surfacelet coefficients, as discussed in Chapter 3. Third, composite surfacelets with the combinations of different types of primitive surfacelets are proposed to increase flexibility of the surfacelet transform with potentially fewer surfacelets and improved reconstruction accuracy, as discussed in Chapter 4. Fourth, the application of surfacelets on material distribution modeling will be introduced in Chapter 5. Fifth, a multi-scale materials design process with seamless zooming capability will be developed. During the zoom-in and zoom-out operations, unevenly distributed grid points are created or chosen from the grids generated from the previous scale, as discussed in

Chapter 6. In the same chapter, the property-oriented materials design process will also be proposed. Last, the conclusions and future work will be discussed in Chapter 7.

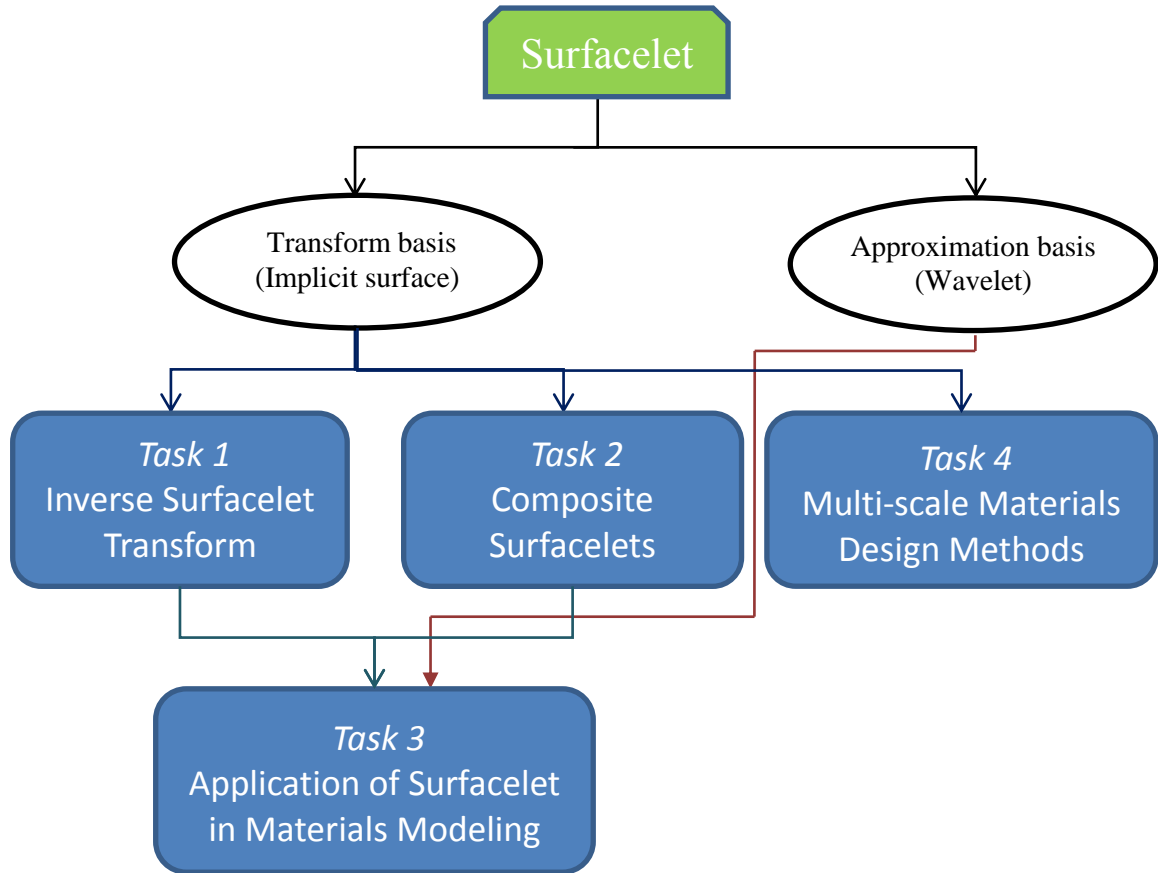


Figure 8 The structure of the tasks for multiscale heterogeneous materials modeling

### 1.7 Technical Contributions

This dissertation presents some fundamental methodologies for materials modeling and design. First of all, a general method of geometric feature identification from 3D material images based on the largest surface integrals is proposed. With this method, the high-level geometric information can be extracted from material microstructural images. Secondly, a method of image data compression based on the forward and inverse surfacelet transform is developed. Thirdly, a method of composite

surfacelet for the identification of complex feature geometries is proposed. Fourthly, a general method of approximating material composition and local property distributions with surfacelets is proposed for the reverse engineering of materials design. Lastly, a generic multi-scale materials modeling method is proposed to support interactive design specification and visualization of material microstructures at multiple levels of details with seamless zooming capability.

## CHAPTER 2

### RELATED WORK

In this chapter, the background and literatures related to the tasks of the dissertation are introduced. Because the multi-scale heterogeneous materials modeling and design methodology proposed in this dissertation is developed based on surfacelet, the concept of surfacelet, as well as its related work will be introduced in Section 2.1. As related work to the inverse surfacelet transform, material characterization and image reconstruction methods will be discussed in Section 2.2. Because the feature identification or recognition plays an important role in the proposed heterogeneous materials modeling and design methodology, related methods will be discussed in Section 2.3. In Section 2.4, existing heterogeneous materials modeling and design methods will be surveyed. In Section 2.5, limitations of the related work discussed in the previous sections will be explained.

#### *2.1 The Surfacelet Basis*

##### **2.1.1 Wedgetlet, curvelet, and surflet**

Wavelets perform well for objects with point singularities in dimension 1. However they are not effective in dealing with edge discontinuities in dimension 2. Several approaches have been proposed to solve this issue, including wedgelet [5] and curvelet [6], as well as their close relatives such as ridgelet [7], contourlet [8], beamlet [9,10], and platelet [11].

The wedgelet approach partitions 2D space into squares as building blocks bounded by line segments. 2D images then can be approximated by a collection of specifically chosen wedgelets. The curvelet function is an extension of the standard

wavelet function, which includes the concepts of statistical regression and a Radon transform. It was developed to compress images containing continuous line or curve segments, where the standard wavelets are not efficient. The basic idea is to introduce an angular element  $\theta$  in the wavelet function as

$$\psi_{a,b,\theta}(\mathbf{r}) = \psi_{a,b,\theta}(x, y) = \frac{1}{\sqrt{a}} \psi\left(\frac{x \cos \theta + y \sin \theta - b}{a}\right)$$

where  $\psi$  is the wavelet function,  $x, y$  are the 2D coordinates,  $a$  is the scaling parameter,  $b$  is the translation parameter, and  $\theta$  is the orientation parameter. If wavelets can be thought of as “fat” points with certain widths of local support, curvelets are “fat” needles.

In 3D analysis, Ying et al. [12] extended 2D curvelet transform to 3D with similar frequency space tilings. Similarly, Lu and Do [13] extended contourlets to three dimensions in a discrete space. Chandrasekaran et al. [14] extended wedgelets to high-dimensional space and approximate functions with polynomial building blocks, called surflets, instead of linear building blocks in wedgelets.

### 2.1.2 Surfacelet

A general surfacelet basis function [4] is defined as

$$\psi_{a,b,\mathbf{p}}(\mathbf{r}) = a^{-1/2} \psi(a^{-1} \rho_{b,\mathbf{p}}(\mathbf{r}))$$

where  $\mathbf{r} = (x, y, z)$  is the location in the domain  $\Omega$  in the Euclidean space,  $\psi : \mathbb{R} \rightarrow \mathbb{R}$  is a wavelet function,  $a \in \mathbb{R}^+$  is a non-negative scaling factor,  $\rho_{b,\mathbf{p}} : \mathbb{R}^3 \rightarrow \mathbb{R}$  is a surface function so that  $\rho_{b,\mathbf{p}}(x, y, z) = 0$  implicitly defines a surface, with the translation factor  $b \in \mathbb{R}$  and the shape parameter vector  $\mathbf{p} \in \mathbb{R}^m$  determining the location and shape of



surface singularity respectively. For instance, a 3D ridgelet that represents plane singularities is defined as

$$\psi_{a,b,\alpha,\beta}(\mathbf{r}) = a^{-1/2} \psi\left(a^{-1}(\cos \beta \cos \alpha \cdot x + \cos \beta \sin \alpha \cdot y + \sin \beta \cdot z - b)\right) \quad (2.1)$$

where  $\alpha \in [0, 2\pi)$  and  $\beta \in [-\pi/2, \pi/2]$  are angular parameters corresponding to rotations around z- and y-axes in the Euclidean space. Similarly, a cylindrical surfacelet (or cylinderlet) can be defined as

$$\psi_{a,b,\alpha,\beta,r_1,r_2}(\mathbf{r}) = a^{-1/2} \psi\left(a^{-1} \left[ \begin{array}{l} r_1 (\cos \beta \cos \alpha \cdot x + \cos \beta \sin \alpha \cdot y + \sin \beta \cdot z - b)^2 \\ + r_2 (-\sin \alpha \cdot x + \cos \alpha \cdot y)^2 \end{array} \right] \right) \quad (2.2)$$

And an ellipsoidal surfacelet (or ellipsoidlet) is defined as

$$\psi_{a,b,\alpha,\beta,r_1,r_2,r_3}(\mathbf{r}) = a^{-1/2} \psi\left(a^{-1} \left[ \begin{array}{l} r_1 (\cos \beta \cos \alpha \cdot x + \cos \beta \sin \alpha \cdot y + \sin \beta \cdot z - b)^2 \\ + r_2 (-\sin \alpha \cdot x + \cos \alpha \cdot y)^2 \\ + r_3 (-\sin \beta \cos \alpha \cdot x + \sin \beta \sin \alpha \cdot y + \cos \beta \cdot z)^2 \end{array} \right] \right) \quad (2.3)$$

The geometric interpretations of the isosurfaces for the three surfacelets for plane, cylindrical, and ellipsoidal singularities are shown in Figure 9.

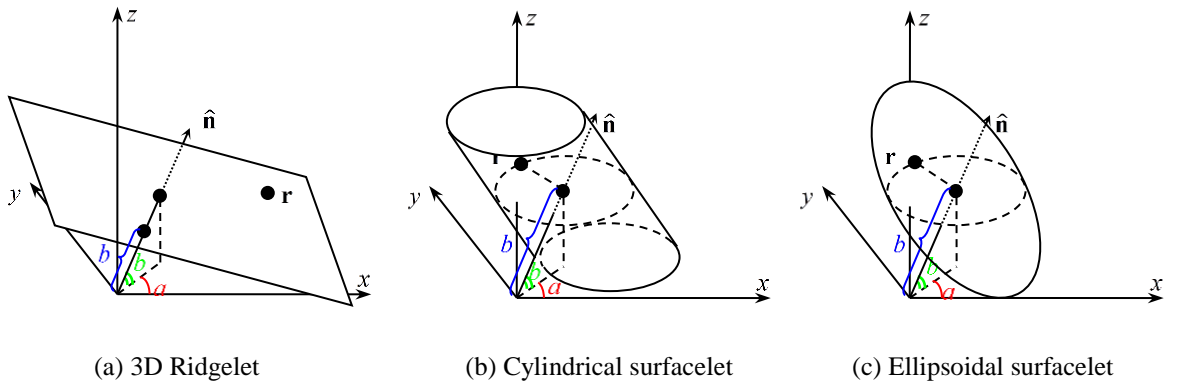


Figure 9 Geometric interpretation of surfacelets

As can be seen from the illustrations, the 3D surfacelet model is able to represent geometric boundary information or surface singularities more efficiently than the wavelets, while keeping a unified form with wavelets. Since wavelet basis functions are better at modeling continuous distributions, a combination of wavelet and surfacelet basis functions is able to efficiently capture the boundary and internal structures at the same time.

## ***2.2 Material Characterization and Image Reconstruction Methods***

### **2.2.1 Radon transform and its inverse**

The surfacelet transform is a generalization of Radon transform. Radon transform [15] is the mathematical basis for reconstructing tomographic images from measured projection, which is given by

$$p(\xi, \phi) = \int f(x, y) \delta(x \cos \phi + y \sin \phi - \xi) dx dy$$

where  $\delta$  is the Dirac delta function and the coordinates  $x$ ,  $y$ ,  $\xi$  and  $\phi$  are the horizontal coordinate, vertical coordinate, the intercept and the slope angle respectively. The geometric interpretation of the Radon transform is the integral along a straight line of  $x \cos \phi + y \sin \phi - \xi = 0$  projected throughout the scanned target. In the parallel-beam tomography,  $\xi$  is varied so that detector acquires parallel projections; rotate circularly around the scanned object so that  $\phi$  is varied, then integrals over the whole  $\xi - \phi$  domain can be obtained.

The task of tomographic reconstruction is to find  $f(x, y)$  given  $p(\xi, \phi)$ . Therefore, this process is also called inverse Radon transform or back projection. Mathematically, the inverse Radon transform is defined as

$$f(x, y) = \int p(\xi, \phi) \delta(x \cos \phi + y \sin \phi, \phi) d\phi d\xi$$

Geometrically, the inverse Radon transform simply propagates the  $\xi - \phi$  space back into the image space along the projection paths.

Since Radon obtained the inverse formula of Radon transform in 1917, many tomographic reconstruction techniques have been proposed. The most famous one is the Direct Fourier reconstruction method. In this method, the solution to the inverse Radon transform is based on the central slice theorem. The central-slice theorem states that the 2D Fourier transform of  $f(x, y)$  along a line at the inclination angle is given by the 1D Fourier transform of  $p(\xi, \phi)$ , that is

$$P(\nu, \phi) = F(\nu \cos \phi, \nu \sin \phi)$$

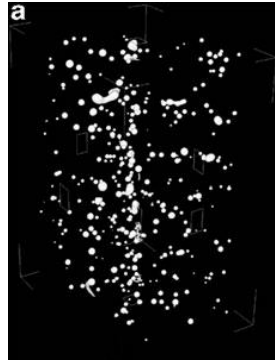
where  $P(\nu, \phi)$  is the 1D Fourier transform of  $p(\xi, \phi)$ ,  $F(\nu_x, \nu_y)$  with parameters  $\nu_x$  and  $\nu_y$  is the 2D Fourier transform of  $f(x, y)$ . Based on the central slice theorem, the inverse Radon transform can be realized by three steps: (1) 1D fast Fourier transform (FFT) of the projection to build a polar 2D Fourier space using the central-slice theorem; (2) Polar to Cartesian resampling; and (3) Inverse 2D-FFT to obtain the reconstructed slice.

### **2.2.2 Material characterization and image reconstruction from physical projections**

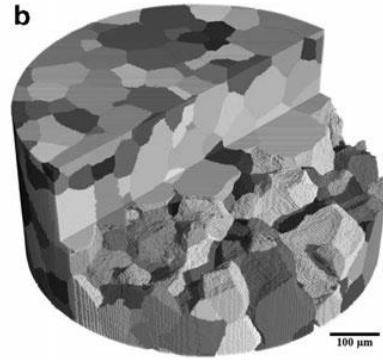
To understand the detailed information about materials, it is important that the mapping images of material characteristics are obtained by physical projections. Specifically, there are three main reasons for material characterization from physical projections: (1) to obtain the material composition information; (2) to obtain the material microstructural information; (3) to obtain the physical property information.

There are two main experimental methods to collect characteristic information of materials. The first is the use of X-rays, which are nondestructive and therefore allow for time-dependent studies that examine microstructural changes due to thermal or mechanical input, i.e., 4D experiments [16]. There are a number of different techniques that can be used to provide image contrast in X-ray tomography experiments [17]. The most common method obtains information by reconstructing a suite of transmission (absorption) images taken at various projections. This technique is very sensitive to differences in atomic number and density, so that microstructural features which are quite different in these characteristics, such as porosity relative to the matrix, can be readily detected. For example, the 3D reconstruction of the porosity in a cast single-crystal nickel base super alloy, CMSX-10, using transmission (absorption) X-ray tomography [18] is shown in Figure 10(a). The dimensions of the reconstructed volume are  $500 \times 500 \times 800 \mu\text{m}$ .

Other methods utilize diffraction contrast and either ray tracing methods [19,16,20] or other spatial localization methods [21,22] to define features such as individual grains from grain aggregates. These diffraction-contrast methods have been greatly advanced in the past few years, and 3D characterization data of grain ensembles can be obtained. As an example, the 3D reconstruction of the 3D grain structure of a tensile sample of  $\beta$ -21 titanium alloy [20] is shown in Figure 10(b). The reconstruction contains 1,008 grains, and was collected using X-ray differential contrast tomography.



(a) The 3D reconstruction of the porosity in CMSX-10 using transmission (absorption) X-ray tomography [18]



(b) 3D reconstruction of the 3D grain structure of a tensile sample of  $\beta$ -21 titanium alloy [20]

Figure 10 Examples of microstructural data that can be obtained with synchrotron X-ray methods

For opaque materials, serial sectioning has been the most widely used method to acquire raw 3D characterization data at the macro-to-micro scale. The first application of this methodology to examine the microstructure of structural metals was published over 90 years ago [23]. Tomographic serial sectioning experiments are conceptually simple, being composed of two steps that are iteratively repeated until completion of the experiment. The first step is to prepare a nominally flat surface, which can be accomplished by a variety of methods such as cutting, polishing, ablating, etching, and sputtering, where ideally a constant depth of material removal has occurred between each section. The second step is to collect two-dimensional (2D) characterization data after each section has been prepared, although data could also be collected continually during material removal depending on the particular sectioning method that is employed. After collection of the series of 2D data files, computer software programs are used to construct a 3D array of the characterization data that can be subsequently rendered as an image or analyzed for morphological or topological parameters. As an example, the 3D reconstruction of the austenite phase in a commercial austenitic stainless steel alloy AL-

6XN [24] is shown in Figure 11. The data set was produced via manual serial sectioning that incorporated collection of both optical images and electron backscatter diffraction (EBSD) maps. The volume contains 138 grains, and the arrow represents the normal of the serial sectioning plane. Although not readily visible because of the gray-scale coloring of this printing, the color of each grain corresponds to the crystallographic orientation relative to the arrow, which was determined by EBSD.

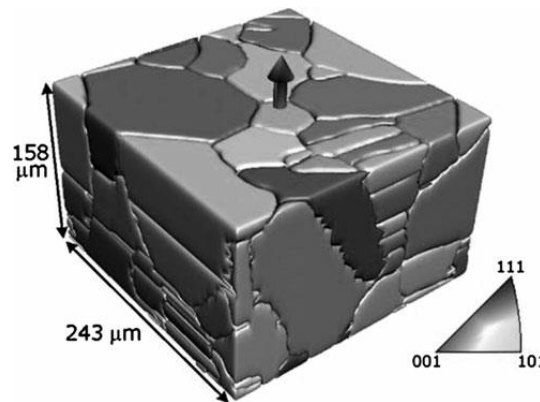


Figure 11 3D reconstruction of the austenite phase in a commercial austenitic stainless steel alloy AL-6XN [24].

One of the most significant limitations of these methods is that they are merely the 3D visualization of materials for the purpose of reverse engineering. Therefore, the models from these methods are difficult to modify for the purpose of materials design as tools for engineers. However, an explicit mathematical model with ease of modification is desired for a design-oriented modeling process. The modeling approach proposed in this dissertation is to provide an engineering tool for design of new materials as its major contribution.

Images are typically obtained through the reconstruction from many forms of physical projections, such as spectral regions across the entire electromagnetic spectrum, transmission electron microscopy (TEM), scanning electron microscopy (SEM) and even

sound or pressure waves [25]. Among all forms, the positron emission tomography (PET) and single photon emission tomography (SPECT) used in  $\gamma$ -ray medical imaging, such as to identify infections or tumors in human bodies, are most widely applied. From the projections, measurements are obtained through line integrals along the projection paths.

Image reconstruction is then performed from integrals to pixels in a computer with reconstruction algorithms. There are two types of algorithms for reconstructing images: analytical and iterative algorithms.

### **2.2.3 Analytical algorithms for image reconstruction**

Shepp et al. [26] proposed the filtered back projection algorithm based on the closed form of inverse Radon transform in Section 2.1. In this method, an operation called ramp filter is introduced. The original images can be obtained by the back projection of the filtered projection profile derived from the ramp filter. Byrne et al. [27,28] developed methods of estimating Fourier transform of a function sampled at limited number of discrete data points by incorporating the prior knowledge of the transformed function. However, the prior knowledge utilized in these methods is limited to shape and support of object power spectrum.

Analytical algorithms have closed-form mathematical expressions. They are efficient and elegant. However, they are unable to handle complicated factors such as scatter. Numerical algorithms were developed, as summarized next.

### **2.2.4 Regularization of linear inverse problems**

Image reconstruction is one type of inverse problems. The field of inverse problems was first introduced by Soviet-Armenian physicist, Viktor Ambartsumian [29]. In this dissertation, the proposed methods are related to the linear inverse problems.

A linear system is described as

$$\mathbf{AX} = \mathbf{B}$$

where  $\mathbf{A}$  is called the observation matrix,  $\mathbf{X}$  is the unknown vector, and  $\mathbf{B}$  is a known vector.

In the case that the observation matrix is not invertible, optimization methods are used to solve the inverse problem. In order to do so, an objective function is defined for the inverse problem. The objective function is to measure how close the predicted data from the recovered model fits the observed data.

Regularization is the process of finding the solution to the optimization problem by trading off between different solutions or introducing additional information or constraints. For example, least-squares method for solving over-constrained linear equation set is a simple regularization method. When the problem is under-constrained, the constraint is usually added to the objective function in the form of a weighted penalty. More details about regularization techniques can be found at [30, 31, 32, 33, 34, 35, 36]. The inverse surfacelet transform developed in this dissertation as the first task uses the concept of regularization to reconstruct images from surfacelets.

### **2.2.5 Iterative algorithms for image reconstruction**

The basic process of iterative reconstruction is that the image is discretized into pixels, and each pixel value is treated as an unknown. Then a system of linear equations is set up according to the imaging projections. Finally, the system of equations is solved by an iterative algorithm. The solution of pixels is unique and easy to obtain if there are enough data of projections. However most of the iterative algorithms deal with incomplete data. Iterative reconstruction is popular for two reasons: (1) it is easy to



model and handle projection noise, especially when the counts are low; and (2) it is easy to model the imaging physics, such as geometry, non-uniform attenuation, scatter, and others [37].

The earliest iterative methods are the algebraic reconstruction techniques (ART). These are a class of numerical approaches designed for solving large sparse systems of equations. The method cycles through the measurements repeatedly and consider only one measurement at a time. Only the pixels involved in the measurement are updated. Herman et al. [38] improved the computational efficiency of the ART method by adjusting the order of accessing the collected data and the so-called relaxation parameters during the reconstruction procedure. Mueller et al. [39,40] adjusted the ART method for image reconstruction in 3D cone-beam computed tomography. Shieh et al. [41] extended the analytical methods of [27,28] to an iterative one.

Another important class of iterative algorithms is the maximum likelihood expectation maximization (ML-EM) or statistical image reconstruction algorithms [42,43,44,45,46,47], which is also the most commonly used algorithm in emission tomography. This algorithm is a general approach to estimate the best image from infinite candidates through the introduction of a set of ‘complete data’ and iterates between computing the mean of the complete data and maximizing the probability of the complete data over the image space.

An alternative scheme to ART and ML-EM estimation is to use standard gradient-based optimization procedures such as steepest ascent or the conjugate-gradient method. This usage started from Goitein [48] and Budinger et al. [49]. As the name indicates, the searching direction is in the gradient of the objective function at the current iteration.

Therefore, the simplest method is the steepest ascent. However, the steepest ascent method has a low convergence rate. This is then resolved by conjugate gradient algorithms, which utilize symmetric and positive-definite coefficient matrices and therefore provide higher convergence rates. The new approach proposed in this research is based on the conjugate gradient algorithm.

According to [50], one major challenge of using gradient-based methods in emission tomography is the inclusion of constraint guaranteeing the non-negativity of all pixel values, which is essentially nonlinear. The most common approach is to restrict the step size so that each update is non-negative. In order to deal with the non-negativity constraint in an easier way, the coordinate ascent (CA) methods were developed [51,52,53,54]. The basic idea of these methods is to sequentially update each voxel to maximize the objective function with respect to that voxel. However, the limitation of the CA algorithms is that the convergence rates are very sensitively dependent on the initial guess of images.

Instead of approaching the emission tomography problem with well-known traditional numerical methods, some methods are developed to meet specific aspects of the problem. Functional substitution methods were developed to better address the sparse nature of the coefficient matrix. They replace the original cost function at each step with a substitutive function so that the value of the original function can be increased when maximized. The best known example of a functional substitution method in emission tomography is the EM algorithm of Dempster et al. [55].

On contrary to analytical algorithms, iterative reconstruction algorithms are less efficient and may not converge to the real solution. However, because of its higher

versatility and easier to implement on computer, the iterative reconstruction algorithms are increasingly used in applications.

### **2.2.6 Conjugate-gradient-based iterative algorithms**

The conjugate gradient method is a well-known numerical method for solving linear least squares problems by iteratively minimizing the squared norm of the difference between the measured and the estimated data. However, such methods are not widely applied in tomographic image reconstruction. Very limited development has been made in this class of methods [56,57,58,59]. One possible reason for the limitation is that conjugate-gradient-based iterative methods usually have slow convergence in solving tomographic image reconstruction problems. Another possible reason is that the conjugate-gradient-based iterative methods can only solve over-constrained problems (that is, the projections should be more than the pixels), but usually the available data of projections are incomplete.

Because of the incomplete data of projections, additional constraints are needed for rational solution of the linear equation system. The existing methods usually obtain the constraints from prior information based on the non-negativity of the object intensity (or density) for the physical reason and/or the geometry of the featured objects. A typical example for the non-negativity of the object intensity is the reconstruction of impulsive object images [60,61]. For the geometric information, Tam et al. [56] and Kawata et al. [58] used the so-called object-boundary constraint. However, these two methods have three major disadvantages. First, the pixels are simply classified to be those inside and outside the object, and there are no independent constraints applied on the boundary pixels. These methods are therefore not suitable for image reconstruction in materials

science, where boundaries among multiple materials are often found in modern materials and therefore clear geometric information of which is required. Second, the pixels outside the object in these methods were simply constrained to be zero, leading to the result that the image information of outer portion is completely ignored and not reconstructed. Third, the pixel positions are manually assigned in both methods, which is obviously not applicable for complex and random object distributions, such as composites.

Shariff [62] developed a constrained conjugate gradient method, which treats the constraints separately from equation system instead of directly adding them to the system. This method is able to emphasize the object boundaries. In this research, a novel image reconstruction method similar to this approach is developed, but with distinctions.

### ***2.3 Image-Based Feature Recognition Methods***

Edges define the boundaries between regions in an image, which help with feature recognition. The edge detection methods [63,64] can be categorized into two groups: search-based and zero-crossing based. The search-based methods capture the feature edges by first computing edge strength and then searching for the local maxima in a direction to match the edge profile. The edge strength and searching direction can be measured and defined in many different forms, such as the magnitude and the direction of the gradient of the image intensity. The gradient is usually represented by the first order derivative. On the other hand, the zero-crossing based methods search for zero crossings based on the second-order derivatives to detect feature edges.

Other methods of identifying geometric features from images have also been developed. For instance, the Radon transform [15] has been applied to identify lines in

2D images [65,66,67]. Similarly, the Hough transform was applied to recognize spherical features in 3D images [68].

## ***2.4 Computer-Aided Heterogeneous Materials Modeling and Design Methods***

### **2.4.1 Computer-aided heterogeneous materials modeling methods**

Two general approaches to heterogeneous modeling have been proposed [69]: discretized and non-discretized approaches. In the first category, materials and geometry are modeled separately, such as mesh-based and voxel-based methods, where geometry is approximated by volume meshes or voxels [70], and material distributions are determined by topology optimization or numerical interpolation from control features [71]. Other researchers applied voxel-based representations that utilized spatial occupancy enumeration of part geometry. Again, material composition information was applied to either individual voxels or interpolated over sets of voxels using a part's bounding surface [72]. General cellular decompositions have also received considerable attention [73]. A general cellular decomposition-based approach integrated physical property distributions into the geometry+material model [74,75] that others have investigated. Some researchers have generalized the cellular modeling approach to include manufacturing process-related Local Composition Control (LCC) elements [76].

In non-discretized approaches, some researchers have separated the representation of material compositions and properties from the underlying part geometry [77,78]. Others have utilized implicit modeling approaches, which have advantages in that a common mathematical model is used for both geometry and material composition [79]. Shapiro and coworkers have applied the theory of R-functions to show how material

composition [80] can be performed using implicit modeling approaches. The advantage of their approach is the unifying nature of implicit modeling to model geometry, material composition, and distributions of any physically meaningful quantity throughout a part. A different group proposed a method based on hypertextures [81] that provides more intuitive user controls, according to the developers. Similar to the implicit modeling approaches, material compositions were specified on part surfaces and similar types of distance measures were used to compute compositions internal to parts.

#### **2.4.2 Computer-aided heterogeneous materials design methods based on structure–property relations**

The core research issue of materials design is to establish process–structure–property–performance relations [82]. As stated in Section 1.1.2, the purpose of the proposed multi-scale materials design method in this dissertation is for the ease of structure–property relation construction, by using a feature-based interactive microstructural modeling approach. It can be used for both top-down and bottom-up design processes.

In constructing structure–property relations, the existing design methods are all based on the statistical distributions of materials. For bottom-up design, Kalidindi et al. [83,84] used a so-called microstructure function to measure the spatial correlations of material microstructures to capture the material microstructural information.

For top-down design, a so-called microstructure sensitive design (MSD) was developed based on spectral representations to capture polycrystalline or anisotropic materials information [85,86,87,88,89]. In this method, a proper orthogonal tensor was used to capture the local orientation of the crystal lattice or phases in composites with

respect to a fixed sample (or global) reference frame bin in the microstructure. The statistical description is then used in predicting mechanical properties of materials [90,91,92,93,94,95]. A so-called “microstructure knowledge systems” (MSK) was recently developed [96,97,98,99,100], which includes higher-order descriptors of microstructures for higher accuracy compared to MSD. MKS is able to describe the spatial distribution of the response field of interest (e.g. stress or strain fields) at small scales for loading conditions at large scales. Chen et al. [101,102] also used the statistical correlation method for material characterization and reconstruction for materials design.

In addition to the above methods to capture the statistical information of microstructures based on material images, little research is done to generate material images systematically. Wu et al. [103] proposed a method of generating 3D image models of stochastic porous media. Kou et al. [104] proposed a microstructural modeling method based on stochastic Voronoi diagram and B-Spline representation. These two methods only model geometries of porous media at a particular scale.

## ***2.5 Limitations of Existing Literatures in the Applications on Multi-scale Heterogeneous Materials Modeling***

First of all, for image recognition, current methods are not suitable for heterogeneous materials modeling. The reason is that, for the purpose of materials design, not only the pixels on the feature edges need to be recognized, it is also important to represent geometric information, such as shapes, dimensions, locations and orientations, of the features at a higher-level abstraction than pixels.

It is well known that the method of convolution is able to find the largest integrals and therefore identify geometric features. However, in this dissertation, it is not used for

the following three reasons. Firstly, the method of convolution only returns the largest integrals for feature identification, and other smaller integrals are ignored for restoration. However, these smaller integrals are also important in the full reconstruction of the material images by inverse surfacelet transform. Secondly, in computer-aided material modeling, the material images are only the media for us to understand the material compositions and structures. We only care about the feature geometries, instead of the detailed pixel values on them. However, the method of convolution only returns the pixels and their values of the matching features, instead of the extracted geometric information. Lastly, the searching step size of the method of convolution is always one pixel's space. However, in the method of largest surface integrals, the step size is flexible. This can effectively enhance the searching efficiency.

Second, for heterogeneous material modeling methods, the limitation of all work described in Section 2.4 is that the models are not multi-scale; at best some can be called multi-resolution. Even then, the resolutions are limited to the overall part geometry and the particular decomposition into cells, voxels, or mesh elements.



## CHAPTER 3

### INVERSE SURFACELET TRANSFORM

The surfacelet transform was proposed so that the image pixels can be converted into surface integrals and then wavelet coefficients. From the surface integrals, material features can be identified. In this chapter, the method of inverse surfacelet transform for retrieving the image pixels from the surface integrals based on the feature identification results is proposed. By the complete method of forward and inverse surfacelet transform, the compression of material image data is realized.

The overview of the complete process of surfacelet transform and inverse surfacelet transform is shown in Figure 12. In the surfacelet transform, surface integrals are obtained from image pixels. 1D wavelet transform is then applied to obtain wavelet coefficients. In the inverse surfacelet transform, the inverse 1D wavelet transform easily retrieves surface integrals from wavelet coefficients. The scope of this chapter is denoted by the dashed box in Figure 12. The inverse problem of retrieving image pixel values from surface integrals is solved based on three constrained conjugate-gradient-based methods with combinations of boundary constraints and inner constraints on internal distributions. The features that determine the boundary constraints are identified from the surfacelet transform process. The locations of internal pixels in the inner constraints can then be calculated from the features. Furthermore, different levels of rigidity associated with the constraints proposed in this chapter provide more flexibility in controlling the constraints than a single-level approach.

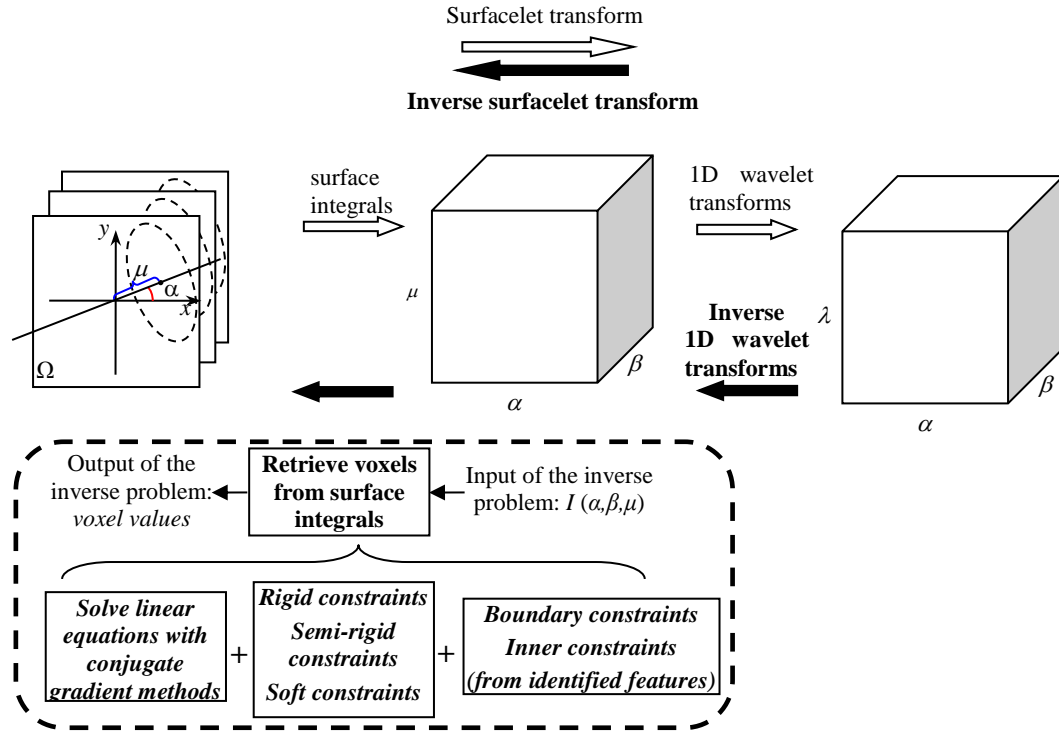


Figure 12 The process of coupled surfacelet transform and inverse surfacelet transform

### 3.1 The Significance of Material Image Data Compression and Dimensionality Reduction

Nowadays, the data storage media, such as computer hard drives, are becoming cheaper, and large data storage is not a big problem anymore. However, people are still seeking for the compression of data of many types because of the expensive reading, writing and transferring times. For example, audio files are still transformed into the MP3 format to store and share, and images are still transformed into the JPEG format. For material images, the requirement of storage space particularly high. For example, a small 3D material image with the size of  $1000 \times 1000 \times 1000$  resolution has 1 billion pixels. Therefore, this image may have a size of hundreds of Mega Bytes even with the compressed JPEG format. Therefore, data compression for material images is important.

In addition, material data represented by pixels do not provide information of microstructural features of materials, such as boundaries and singularities. A more abstract level of description is useful to capture and preserve material knowledge, and help both human users and computers to perform design tasks without losing the essential information. Therefore, data-compression and dimension reduction are important in materials information processing.

### ***3.2 The General Idea of Inverse Surfacelet Transform***

In the surfacelet transform, the surface integrals can be obtained by the summation of all the pixel values on the surfacelets. For instance, for each integral  $t_q(\alpha, \beta, \mu)$  corresponding to a cylindrical surfacelet with the orientation parameters  $\alpha$  and  $\beta$ , and the position parameter  $\mu$ , there exists a simple linear relationship of summation to approximate the integral. Here,  $\mu$  is the translation along x-axis.  $\alpha \in [0, 2\pi)$  and  $\beta \in [-\pi/2, \pi/2]$  are the angular parameters corresponding to rotations around z- and y-axes in the Euclidean space respectively. When this summation is applied to all of the surface integrals with  $P$  pixels and  $Q$  surfacelets, it can be obtained that

$$\mathbf{AV} = \mathbf{T} \quad (3.1)$$

where  $\mathbf{A}$  is a  $Q \times P$  matrix with coefficient components  $a_{qp}$  as either 1 or 0,  $\mathbf{V} = (v_p)$  is a  $P$ -dimensional vector for pixel values  $v_p$ 's ( $p=1, \dots, P$ ), and  $\mathbf{T} = (t_q)$  is a  $Q$ -dimensional vector for surface integrals  $t_q$ 's ( $q=1, \dots, Q$ ).  $a_{qp} = 1$  if the corresponding pixel is on the surfacelet; and  $a_{qp} = 0$  otherwise. Suppose that the numbers of discretized  $\mu$ ,  $\alpha$ , and  $\beta$  are  $u$ ,  $f$ , and  $g$  respectively. The number of surface integrals is  $Q = u \times f \times g$ .

At the same time, if the dimension of each image is  $L \times M$  and there are  $N$  parallel images, then the total number of pixels is  $P = L \times M \times N$ . It should be noted that the number of pixels on a surfacelet varies from surfacelet to surfacelet, which means that the numbers of ones and zeros on each row of matrix  $\mathbf{A}$  vary. Furthermore, a zero integral will be obtained if the surfacelet is positioned or oriented such that it is out of the image domain. In this case, it does not provide useful information and should be avoided if possible. When a surfacelet only covers the pixels that are also covered by other surfacelets, dependency between rows in the coefficient matrix  $\mathbf{A}$  occurs, which is very likely to occur. As a result, the  $Q$  linear equations with non-zero integrals are not necessarily linearly independent.

The solution of Eqn. (3.1) depends on the relationship between  $P$  and  $Q$ . It is obvious that when  $P = Q$  and the  $Q$  linear equations with non-zero integrals are independent, there is only one exact real solution. When  $P < Q$ , the unknown  $v_p$ 's are over-constrained and there is no exact solution. When  $P > Q$ , the unknown  $v_p$ 's are under-constrained and there are an infinite number of solutions. Even in the ideal case of  $P = Q$ , it is possible that a zero integral occurs or the equations are dependent. Then the coefficient matrix  $\mathbf{A}$  is singular, and the equation will have an infinite number of solutions.

The approaches proposed in this chapter solve both cases of  $P < Q$  and  $P > Q$ . The case of  $P < Q$  applies when lossless restoration of image data is desired. In contrast,  $P > Q$  is the case when the surfacelet transform is used in lossy compression, which is more common in applications. In the inverse surfacelet transform, classic numerical methods are utilized to solve the case of  $P < Q$ . A new prior-knowledge-based image

reconstruction method is proposed here for the case of  $P > Q$ , where the boundaries of the key geometric features known a priori are automatically identified and located by the primitives of surfacelets. Then the boundary and/or inner pixels are constrained based on the prior knowledge in order to add more conditions to those from surfacelets. A constrained conjugate gradient algorithm is used to treat these conditions as independent constraints. In addition, a new semi-rigid constrained conjugate gradient algorithm is also proposed to provide a more flexible way to constrain pixels.

### 3.3 *The Inverse Surfacelet Transform without Constraints*

Solving the linear equation  $\mathbf{B}\mathbf{X} = \mathbf{b}$  is equivalent to solving

$$\min F(\mathbf{X}) = \frac{1}{2} \mathbf{X}^T \mathbf{B} \mathbf{X} - \mathbf{X}^T \mathbf{b}$$

which can be done by convex quadratic programming.

In the case of  $P < Q$ , approximation methods are available to numerically solve the over-constrained problems. The two most used ones are the general least-square and conjugate gradient methods. Both are based on the minimization of least-square errors. Eqn. (3.1) is then formulated as

$$\min \left( \sum_{q=1}^Q (\mathbf{A}_{q\bullet} \mathbf{V} - t_q)^2 \right)$$

where  $\mathbf{A}_{q\bullet}$  is the  $q^{\text{th}}$  row of matrix  $\mathbf{A}$ . The solution of the general least-square method is obtained by  $\mathbf{V} = (\mathbf{A}^T \mathbf{A})^{-1} \mathbf{A}^T \mathbf{T}$  where  $\mathbf{A}$  is not necessarily a square matrix.

The conjugate gradient method is an iterative approach to search for the numerical solution of linear equation systems with a symmetric and positive-definite coefficient matrix. The idea is that  $\mathbf{V}$  is iteratively searched for as the solution of

$$\min_{\mathbf{v}} \frac{1}{2} \mathbf{V}^T \mathbf{B} \mathbf{V} - \mathbf{V}^T \mathbf{b} \quad (3.2)$$

corresponding to  $\mathbf{B} \mathbf{V} = \mathbf{b}$ , where  $\mathbf{B}$  is a symmetric and positive-definite matrix. Since matrix  $\mathbf{A}$  in Eqn. (3.1) is not symmetric and positive-definite, it cannot be directly applied to the method. Rather, the equation is transformed to

$$\mathbf{A}^T \mathbf{A} \mathbf{V} = \mathbf{A}^T \mathbf{T} \quad (3.3)$$

and let  $\mathbf{A}^T \mathbf{A} = \mathbf{B}$  and  $\mathbf{A}^T \mathbf{T} = \mathbf{b}$ , since  $\mathbf{A}^T \mathbf{A}$  is symmetric. Additionally, because  $t_i \geq 0$ ,  $\mathbf{T}^T \mathbf{T} = (\mathbf{A} \mathbf{V})^T \mathbf{A} \mathbf{V} = \mathbf{V}^T \mathbf{A}^T \mathbf{A} \mathbf{V} > 0$ . Therefore,  $\mathbf{A}^T \mathbf{A}$  is also positive-definite. Thus, by applying the conjugate gradient method to Eqn. (3.3), the linear equations can be solved.

Although a numerical solution can be obtained for the case of  $P < Q$ , it contradicts to the initial intention of surfacelets, which is designed for image compression. As a result, the case of  $P > Q$  also needs to cope with, where there are many solutions of the minimization problem in Eq. (3.2). Extra knowledge with respect to the materials applications acting as constraints can help us to narrow the scope of solutions, as discussed in the next subsection.

### ***3.4 The Inverse Surfacelet Transform with Constraints***

#### **3.4.1 General procedure of inverse surfacelet transform with constraints**

The main goal of inverse surfacelet transform with constraints is to add more equations as constraints in an under-constrained system so as to reduce the number of possible solutions and convert it to an over-constrained system. In order to make  $P < Q$  possible, even when limited surfacelets are available, additional constraints based on the prior knowledge of materials can be added. One possible type of constraint is based on geometry, or the shape of the object of interest that is already known in the images. Take

fibrous porous media as an example. Suppose the geometry of the fibers is already known, and obtaining the information of orientations and positions of the fibers is generally of more interest than the detailed microstructures of the fibers and matrix from reconstruction. As a result, the pixels on the fibers are more important than others. By properly restricting the pixel values of the interested object based on prior knowledge, the additional constraints provide more information of the object. Since the object is identified as a geometric feature in the inverse surfacelet transform, hereafter, the object is called *feature*.

In the forward surfacelet transform, the type and parameters of surfacelets are determined by the geometric similarity between the material compositions and some surfacelet primitives, such as 3D ridgelet, cylindrical surfacelet (or cylinderlet), and ellipsoidal surfacelet (or ellipsoidlet). For instance, images for fibers in composites can be reconstructed by the cylindrical surfacelet, whereas those for nano ellipsoidal fillers in nano-reinforced composites can be reconstructed by the ellipsoidal surfacelet. In grey scale images, white pixels have the value of 255, black ones have 0, and grey ones have intermediate values according to the corresponding grey scales. Usually, the geometry in the images of materials of interest is brighter than other regions. The surfacelets that cover the feature boundary thus have the largest integral values. The shape and dimension of the surfacelet should be chosen to simulate the reconstructed geometry boundary with the largest integral value achieved when the surfacelet is overlapped with the feature boundary.

Boundary features are identified as follows. If there is more than one target feature to be reconstructed, such as many fibers in composite materials, it is likely that

the largest integrals for each target are very close to each other and it is difficult to differentiate. In this case, the integrals can be grouped into different clusters according to their positions and orientations, and the largest integral in each cluster determines a feature boundary.

Once the corresponding pixels are identified by the rule of the largest surface integral described above, their values are set to be equal based on the fact that the grey scale of the geometry is relatively uniform. The equal values are transformed into additional linear equations by each two adjacent pixels forming an equation, such as  $v_p = v_{p+1}$ . The set of newly formed equations is represented in a matrix form as  $\mathbf{CV} = \mathbf{0}$ , where  $\mathbf{C}$  is the  $S \times P$  constraint coefficient matrix for  $S$  constraints with components  $c_{sp}$  as  $-1$ ,  $0$ , or  $1$ .  $c_{sp} = 1$  when the corresponding voxel is on the left of the equation;  $c_{sp} = -1$  when the corresponding voxel is on the right of the equation;  $c_{sp} = 0$  when the corresponding voxel is not in the equation. The  $S$  linear equations are from the  $S+1$  pixels with equal values on the boundary. Since the number  $S+1$  is usually very large, when these equations are combined with  $Q$  equations from surface integrals, the number of known conditions can be dramatically increased. When the total number of equations is larger than the number of unknowns, the number of solutions is no longer infinite. As a result, fewer surfacelets are required so that the surface integral data needed for image reconstruction can be reduced and compression can be achieved.

Furthermore, if the inner structure or geometry of the feature is not of interest, or it has identical grey scale with the boundary such as the inside portion of fibers, the constraint can be further extended such that both the boundary pixel values and the inner



ones are set to be equal. Thus, the number of constraint equations can be further increased and the data needed for image reconstruction can be further compressed.

### 3.4.2 Inverse surfacelet transform with soft constraints

If the constraint equations are directly added to the ones from surface integrals to form a new set of equations, all equations are treated equally. The equation set is formulated as

$$\begin{bmatrix} \mathbf{A} \\ \mathbf{C} \end{bmatrix} \mathbf{V} = \begin{bmatrix} \mathbf{T} \\ \mathbf{0} \end{bmatrix}$$

The requirement is that after the addition of constraints, the total number of equations is larger than the number of pixels. In other words, all equations have the same weight. In this case, the constraints are called soft, because these constraints will not necessarily be all satisfied in solving the over-constrained system by the least-square methods.

### 3.4.3 Inverse surfacelet transform with rigid constraints

If the constraint equations are treated separately from the ones from surface integrals and more rigidly restricted, the constraints weigh more. In other words, the constraints are stronger than otherwise being directly added to the equations from surface integrals. In this case, the constraints are called rigid. It is solved by the constrained conjugate gradient method with constraints separate from the equation system, similar to [105]. This is an extension of the conjugate gradient method described in the Section 2.2.6. The problem can be described as

$$\begin{aligned} \min_{\mathbf{V}} \quad & \frac{1}{2} \mathbf{V}^T \mathbf{A}^T \mathbf{A} \mathbf{V} - \mathbf{V}^T \mathbf{A}^T \mathbf{T} \\ \text{s.t.} \quad & \mathbf{C} \mathbf{V} = \mathbf{0} \end{aligned} \tag{3.4}$$

The conjugate gradient algorithm under rigid constraints to solve Eqn. (3.4) is listed in Table 1. The main procedure is an Arnoldi style iteration. The enforcement of rigid constraints is by a projection of the residual  $\mathbf{r}$  to  $\mathbf{z}$  through an orthogonal projection matrix  $\mathbf{H} = \mathbf{Z}(\mathbf{Z}^T\mathbf{Z})^{-1}\mathbf{Z}^T$ , where  $\mathbf{Z}$  forms a basis for the null space of  $\mathbf{C}$ , that is  $\mathbf{CZ} = \mathbf{0}$ . It should be noted that in this method, it is not required that  $P < Q$  for matrix  $\mathbf{A}$ .

Table 1 Rigid constrained conjugate gradient algorithm

INPUT: matrix $\mathbf{A}$ , constraint matrix $\mathbf{C}$ , initial guess $\mathbf{V}_0$	
OUTPUT: $\mathbf{V}_{k+1}$	
1.	$\mathbf{T} := \mathbf{T}_0$
2.	$\mathbf{H} = \mathbf{Z}(\mathbf{Z}^T\mathbf{Z})^{-1}\mathbf{Z}^T$ where $\mathbf{CZ} = \mathbf{0}$
3.	$\mathbf{r}_0 := \mathbf{A}^T\mathbf{A}\mathbf{V}_0 - \mathbf{A}^T\mathbf{T}$
4.	$\mathbf{z}_0 := \mathbf{H}\mathbf{r}_0$
5.	$\mathbf{d}_0 := \mathbf{z}_0$
6.	$k := 0$
7.	Repeat
8.	$\nu_k := \frac{-\mathbf{r}_k^T \mathbf{d}_k}{\mathbf{d}_k^T \mathbf{A}^T \mathbf{A} \mathbf{d}_k}$
9.	$\mathbf{V}_{k+1} := \mathbf{V}_k + \nu_k \mathbf{d}_k$
10.	$\mathbf{r}_{k+1} := \mathbf{r}_k + \nu_k \mathbf{A}^T \mathbf{A} \mathbf{d}_k$
11.	$\omega_k := \frac{\mathbf{r}_{k+1}^T \mathbf{z}_{k+1}}{\mathbf{r}_k^T \mathbf{z}_k}$
12.	$\mathbf{d}_{k+1} := -\mathbf{z}_{k+1} + \omega_k \mathbf{d}_k$
13.	If $\mathbf{d}_{k+1}^T \mathbf{d}_{k+1}$ is sufficiently small
14.	exit loop
15.	End If
16.	$k := k + 1$
17.	End Repeat
18.	Return $\mathbf{V}_{k+1}$

### 3.4.4 Inverse surfacelet transform with semi-rigid constraints

The method with soft constraints in Section 3.4.2 does not enforce the constraints, whereas the one with rigid constraints in Section 3.4.3 requires all constraints to be satisfied. Here a third option with more flexibility about the constraints is also provided, which is called semi-rigid. The semi-rigid constraints are realized through an exterior penalty function, which includes constraints in the objective function. The rigidity of the constraints can be controlled by their weights in the objective function. With the exterior penalty function, Eqn. (3.4) can be transformed into an optimization problem with the objective function only as

$$\frac{1}{2} \mathbf{V}^T \mathbf{A}^T \mathbf{A} \mathbf{V} - \mathbf{V}^T \mathbf{A}^T \mathbf{T} + \sum_{i=1}^S w_i (\mathbf{C}_{i\bullet} \mathbf{V})^2$$

where  $\mathbf{C}_{i\bullet}$  is the  $i^{\text{th}}$  row vector of the constraint coefficient matrix  $\mathbf{C}$ . When all weights are set to be equal, the objective function can be further simplified as

$$\frac{1}{2} \mathbf{V}^T \mathbf{A}^T \mathbf{A} \mathbf{V} - \mathbf{V}^T \mathbf{A}^T \mathbf{T} + w \mathbf{V}^T \sum_{i=1}^S \mathbf{C}_{i\bullet}^T \mathbf{C}_{i\bullet} \mathbf{V} \quad (3.5)$$

In order to use the conjugate gradient method to solve the new objective function in Eqn. (3.5), it needs to be further transformed into

$$\mathbf{V}^T \mathbf{G} \mathbf{V} - \mathbf{V}^T \mathbf{A}^T \mathbf{T}$$

where  $\mathbf{G} = \frac{1}{2} \mathbf{A}^T \mathbf{A} + w \sum_{i=1}^S \mathbf{C}_{i\bullet}^T \mathbf{C}_{i\bullet}$ .

In the proposed method of semi-rigid constrained conjugate gradients, some constraints can be treated in a different way other than strictly soft or rigid. For instance, in a fiber, the constraints on the internal pixels can be softer than the ones for the boundary pixels. Then the weights associated with the constraints for the internal pixels

are smaller than the ones for the boundaries. Once the rigidity is controlled by assigning different weight values, softer constraints can be introduced based on the inner pixels in addition to the boundaries. With more constraints, the number of required surfacelets can be potentially further reduced without losing the information of pixels outside the object boundary.

### 3.5 Examples And Results

In this section, examples and results for the methods described in Section 3.3 and Section 3.4 are demonstrated and compared. The experiment is conducted in MATLAB. For all examples, nine images of a small portion of a nano-fiber composite are used. The images are in the format of JPEG, one of them is shown in Figure 13(a). The full size of the picture is  $80 \times 80$  pixels. Thus, the total number of pixels is  $P = 80 \times 80 \times 9 = 57600$ , and the dimension of the coefficient matrix  $\mathbf{A}$  is large. The original images are down sized to  $20 \times 20$ , as shown in Figure 13(b)-(c), and used in the demonstration. Although the blurring image in Figure 13(b) and the non-blurring image in Figure 13(c) are visually different, they are exactly the same in terms of pixel values. The images are then converted into grey scale in MATLAB. The total number of pixels used in the following examples is  $P = 20 \times 20 \times 9 = 3600$ . The nine resized images are shown in Figure 14. They are slightly different from each other, and form a 3D image.

To quantitatively compare the results of different methods, the error measurement

$$e = \sqrt{\frac{1}{P} \sum_{i=1}^P (v_i - v_i^0)^2}$$

is introduced, where  $v_i^0$  is the  $i^{\text{th}}$  pixel value in the original images and  $v_i$  is the one from the reconstructed images.

The cylindrical surfacelet is used for the forward and inverse surfacelet transforms in all examples of this chapter. The equation of a cylindrical surfacelet is shown in Eqn. (2.2). The shape parameters of the implicit surface of the cylindrical surfacelet are  $r_1 = 1$  and  $r_2 = 2$ . The ranges of the orientation parameters are set to be  $\mu \in (-D/2, D/2) = (-14.84, 14.84)$ ,  $\alpha \in [0, 2\pi)$  and  $\beta \in [-\pi/2, \pi/2]$  to ensure that the surfacelets cover all of the pixels, where  $D = \sqrt{20^2 + 20^2 + 9^2}$  is the diagonal length of the 3D image.

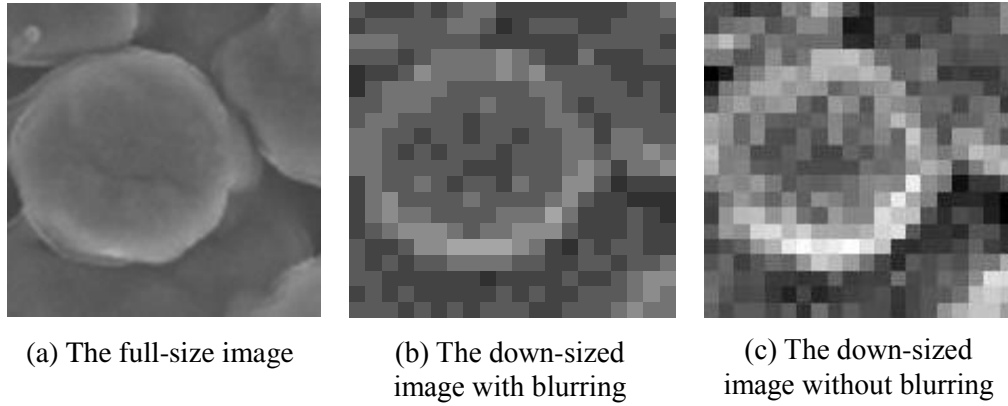


Figure 13 The full and down-sized images of nano-fiber composites

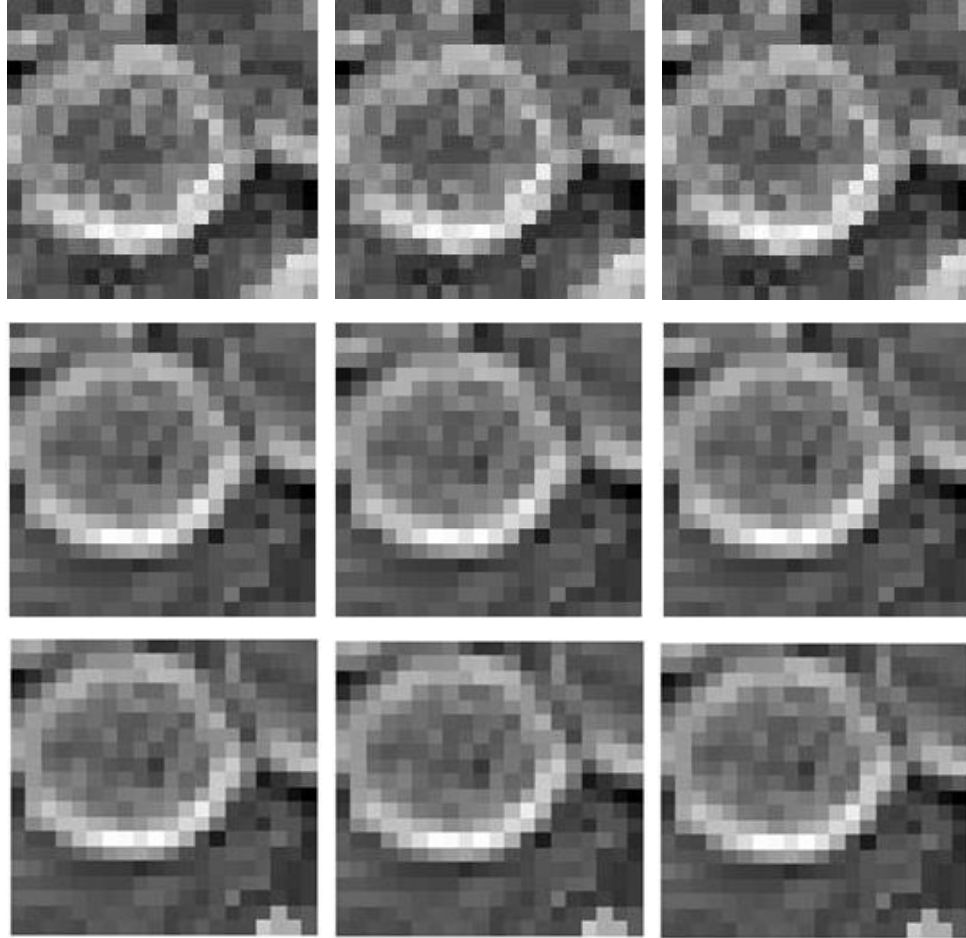


Figure 14 The original nine slices of the 3D image of nano-fiber composites for reconstruction

### 3.5.1 Without Constraints

Reconstruction with both the least-square and conjugate gradient methods without constraints was conducted. The result shows that the full reconstruction of the original images occurs when  $u = 80$ ,  $f = 80$ , and  $g = 5$ . The total number of surfacelets are  $Q = u \times f \times g = 32000$  and  $Q > P$ . These threshold values of  $u$ ,  $f$ , and  $g$  allow all of the pixels in the images to be covered by the surfacelet boundaries without missing any. The reconstruction results of the least-square and conjugate gradient methods are shown in Figure 15 and Figure 16 respectively. With a careful comparison between pixel values,

it is concluded that the least-square and conjugate gradient methods provide the same reconstruction result with these 32,000 surfacelets. The original images are retrieved losslessly.

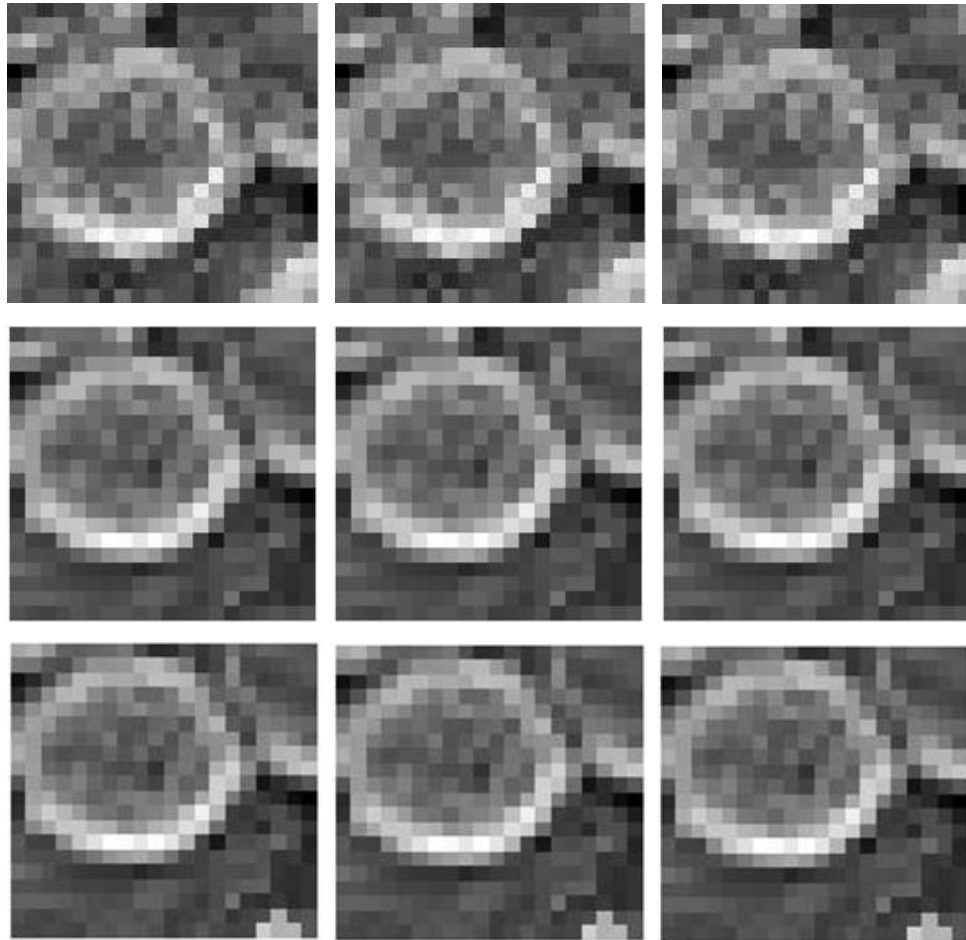


Figure 15 The full reconstruction result with the least-square method. The error is  $e=0$ .

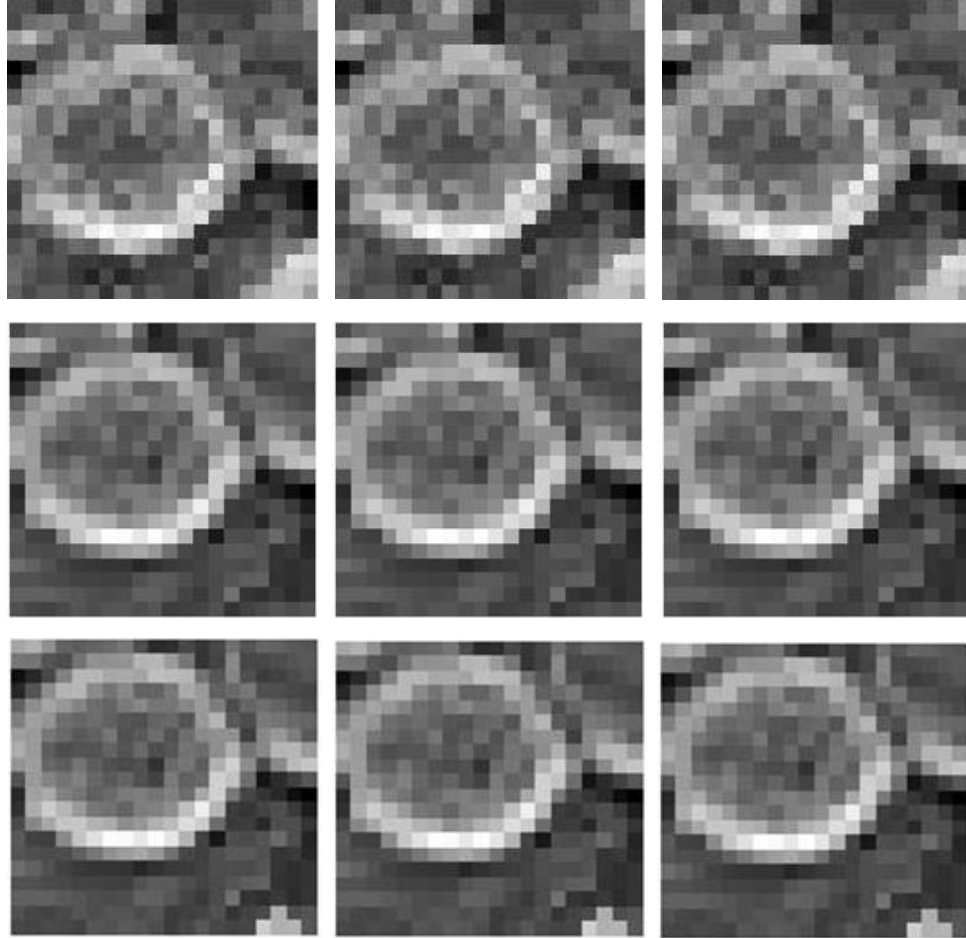


Figure 16 The full reconstruction result with the conjugate gradient method. The error is  $e=0$ .

### 3.5.2 With Constraints

#### 3.5.2.1 Method of automatic fiber boundary identification

For the example of the nano-fiber composites, the positions and orientations of the fibers are of interest. Geometric information of the fibers, such as the shape and size as prior knowledge to us, can be utilized as additional constraints. The constraints are imposed by examining the surfacelet integrals. As shown in Figure 17, the cylindrical surfacelet denoted by the solid circle is overlapped with a fiber surface and has a larger integral value than others such as the two denoted by the circles of dashline. Therefore



surface integrals help determine the positions and orientations of the nano-fibers. If there is only one nano-fiber, its position and orientation can be directly estimated by the cylindrical surfacelet with the largest integral. This can be realized by sorting the surface integrals from the results of forward surfacelet transform. If there is more than one fiber, the largest integral for one fiber can be very close to the one for another fiber, because some surfacelets are overlapped with multiple fibers. In this case, the integrals are grouped into different clusters according to their positions and orientations, and the largest integral in each cluster determines a fiber. As the constraints, the pixel values on the surfacelets can be set to be equal to each other.

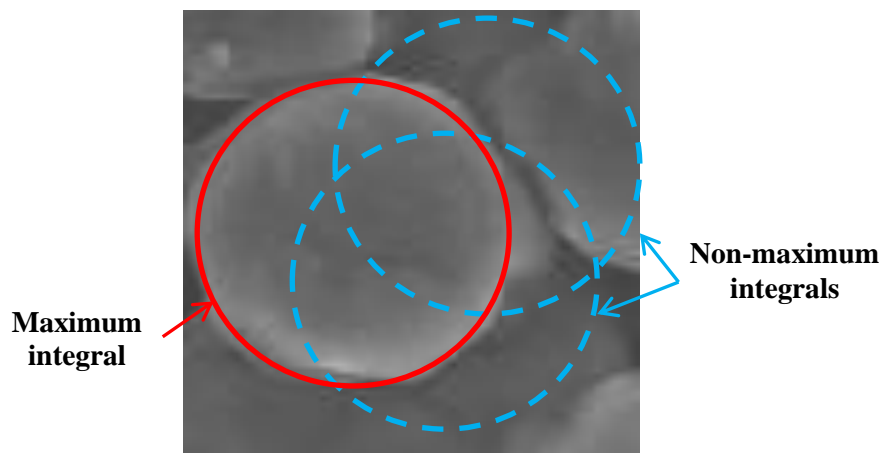


Figure 17 The cylindrical surfacelet overlapped with a fiber surface has the maximum integral

As can be seen from Figure 13, there are four fibers in the images. However, there is only one complete fiber. As a result, the boundary integrals for other fibers are much smaller than that of the complete one. The nano-fibers are close to each other, so the small surfacelet clusters of the partial fibers could be mixed with the complete one. Therefore, it is hard to identify those partial fibers. This problem will be addressed in the

future work. In this dissertation, only complete fibers are identified, and there is only one in this example.

### 3.5.2.2 Soft constraints

In the case of soft constraints, the constraints of equal pixel values at the fiber boundaries are directly added to the original set of equations. The number of pixels on the identified fiber boundary is 340. Therefore, 339 constraint equations are added. In other words, the dimension of the constraint matrix  $\mathbf{C}$  is  $339 \times 3600$ . As stated in Section 3.4.2, the requirement is that the total number of equations is larger than the number of pixels. The results with the least-square method are shown in Figure 18, where the number of surfacelets used from the forward surfacelet transform is  $Q = 58 \times 58 \times 4 = 13456$ ,  $Q = 60 \times 60 \times 4 = 14400$ , and  $Q = 70 \times 70 \times 5 = 24500$  respectively. Since the nine resulted images are similar, only one image is shown in Figure 18 for comparison. It can be seen that when  $Q = 70 \times 70 \times 5 = 24500$ , the error  $e=4.8$  is the smallest among the three. The images in this case are very close to the original ones. Similar results are obtained with the conjugate gradient method, as shown in Figure 19. Thus, with the soft boundary constraints, the number of surfacelets required to retrieve the original images is smaller than the one in the methods without constraints in Section 3.5.1. However, the number of surfacelets is still larger than that of pixels.

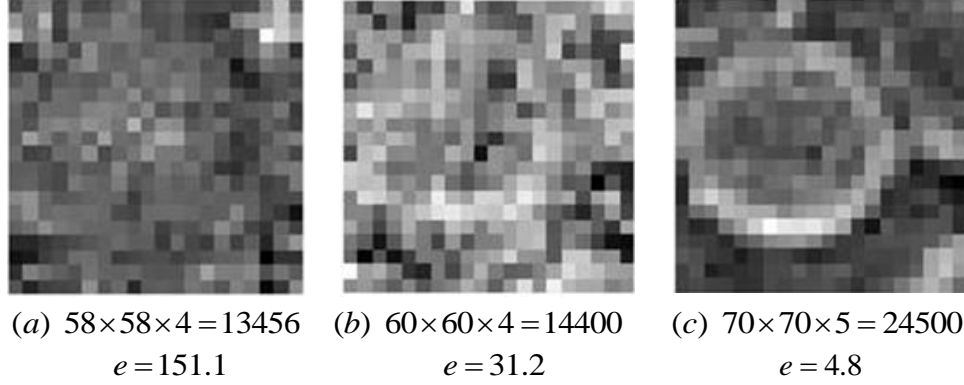


Figure 18 The reconstruction results of soft boundary constraints with the least-square method (first slices only)

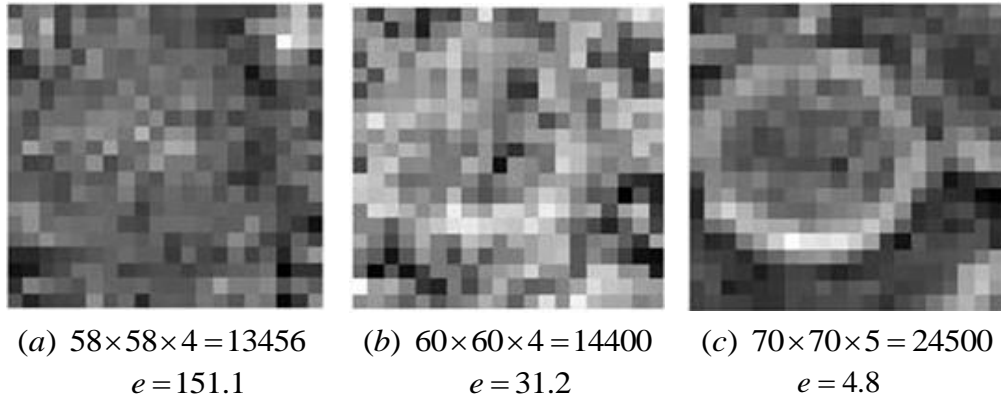


Figure 19 The reconstruction results of soft boundary constraints with the conjugate gradient method (first slices only)

In order to further increase the number of constraints, the inner pixels of the surfacelets are also set to be equal but different from the boundary ones. Therefore, the problem can be formulated as

$$\begin{bmatrix} \mathbf{A} \\ \mathbf{C}_1 \\ \mathbf{C}_2 \end{bmatrix} \mathbf{V} = \begin{bmatrix} \mathbf{T} \\ \mathbf{0} \\ \mathbf{0} \end{bmatrix}$$

where  $\mathbf{C}_1$  is the constraint coefficient matrix for fiber boundary pixels, and  $\mathbf{C}_2$  is the constraint coefficient matrix for fiber inner pixels. Since the number of inner pixels is large, the increase of the number of constraint equations is significant. The number of

pixels inside the identified fiber boundary is 995. Therefore, the dimension of the constraint matrix  $\mathbf{C}_2$  is  $994 \times 3600$ . The results of the method are shown in Figure 20. When the number of surfacelets is too small as in the case of Figure 20(a), the effective (linear independent) equations can be fewer than the unknown. Therefore, the solution is actually not unique.

From the results, it can be seen that the number of surfacelets can be further reduced from the ones with only boundary constraints as in Figure 18 and Figure 19 to achieve similar results. After the addition of constraining equations, the equation system becomes over-constrained. The numerical solutions by minimizing the errors provide the approximations of the true values.

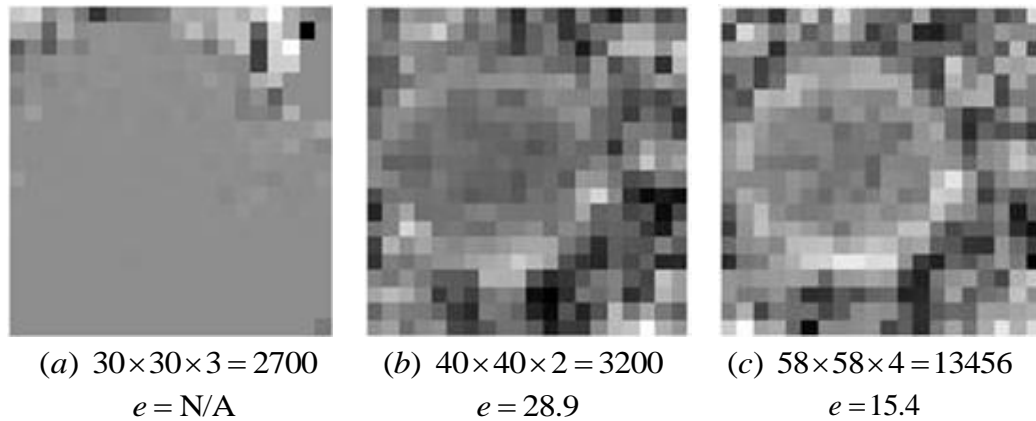


Figure 20 The reconstruction results of soft fiber boundary and inner constraints (first slices only)

### 3.5.2.3 Rigid constraints

When rigid constraints of boundaries are applied, the results are shown in Figure 21. Compared to the method with soft fiber boundary and inner constraints, the method with rigid boundary constraints is able to reconstruct the image by much fewer surfacelets with similar errors. More importantly, this method realizes image

compression, which is one of the important intentions of the surfacelet transform. It can be seen in Figure 21(c) that as few as 1875 surfacelets can be used to reconstruct 3600 pixels with a small error. The compression rate is approximately 50% in this example. All of the resulting nine images are shown in Figure 21.

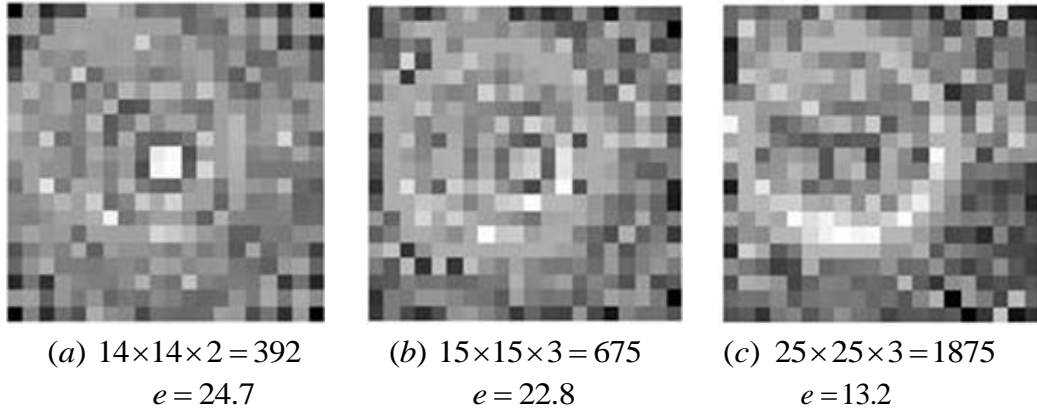


Figure 21 The reconstruction results of rigid fiber boundary constraints (first slices only)

Further compression may be realized if the inner pixels are also constrained. In other words, equality constraints are separately applied on both fiber boundary and fiber inner pixels. The problem can be formulated as the objective function of Eqn. (3.4) with constraints  $\mathbf{C}_1 \mathbf{V} = \mathbf{0}$  and  $\mathbf{C}_2 \mathbf{V} = \mathbf{0}$ . The results are shown in Figure 23. It can be seen that the number of surfacelets is significantly reduced.

The drawback of this method is that although the key features of the complete fiber remain, the detailed information about the partial fibers is lost. The reason is that the constraints have a significant influence on the solution. Therefore, weaker constraints may provide better results.

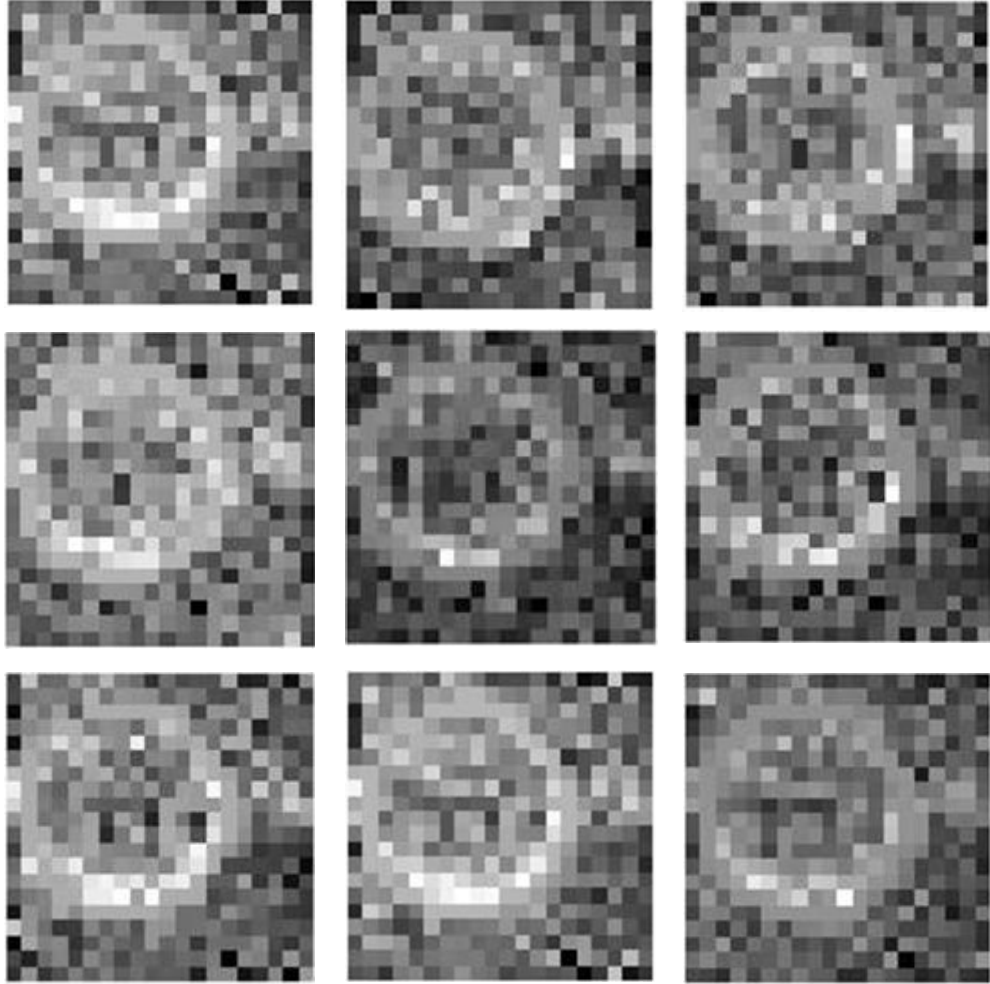


Figure 22 The full reconstruction result of rigid fiber boundary constraints in the case of  $Q=25\times 25\times 3=1875$ . The error is  $e=13.2$ .

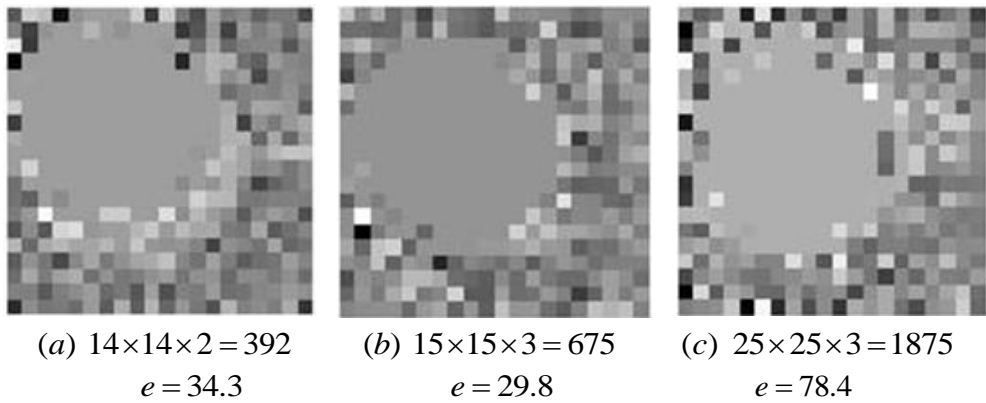


Figure 23 The reconstruction results of rigid fiber boundary and inner constraints (first slices only)

### 3.5.3 Semi-rigid constraints

From the results of Section 3.5.2, it can be seen that some tradeoffs are needed in selecting the reconstruction methods. When the rigid constraints are applied on the boundary only, the number of surfacelets is more than the one when the rigid constraints of boundary and inner pixels are both applied, where the number of constraints increases. However, the errors with the rigid boundary constraints are smaller. Here, it is shown that the method of semi-rigid constraints provides a third option with more flexibility.

The results for semi-rigid fiber boundary and inner constraints with different combinations of weights are shown in Figure 24, Figure 25, and Figure 26 respectively. It can be seen that when penalty weights for boundary pixels are equal to  $1 \times 10^{10}$ , the results have the smallest error. Compared to the method with rigid fiber boundary and inner constraints, the results of the semi-rigid method have clearer fiber boundaries. Besides, compared to the method with only rigid fiber boundary constraints, although the error is relatively the same, the pixels inside the fiber have smoother transition, which increases the contrast between the pixels on and off the fiber. Although the contrast is also increased if rigid constraints are added on both boundaries and inner pixels as in Figure 23, the boundary is not as clear as in Figure 25.

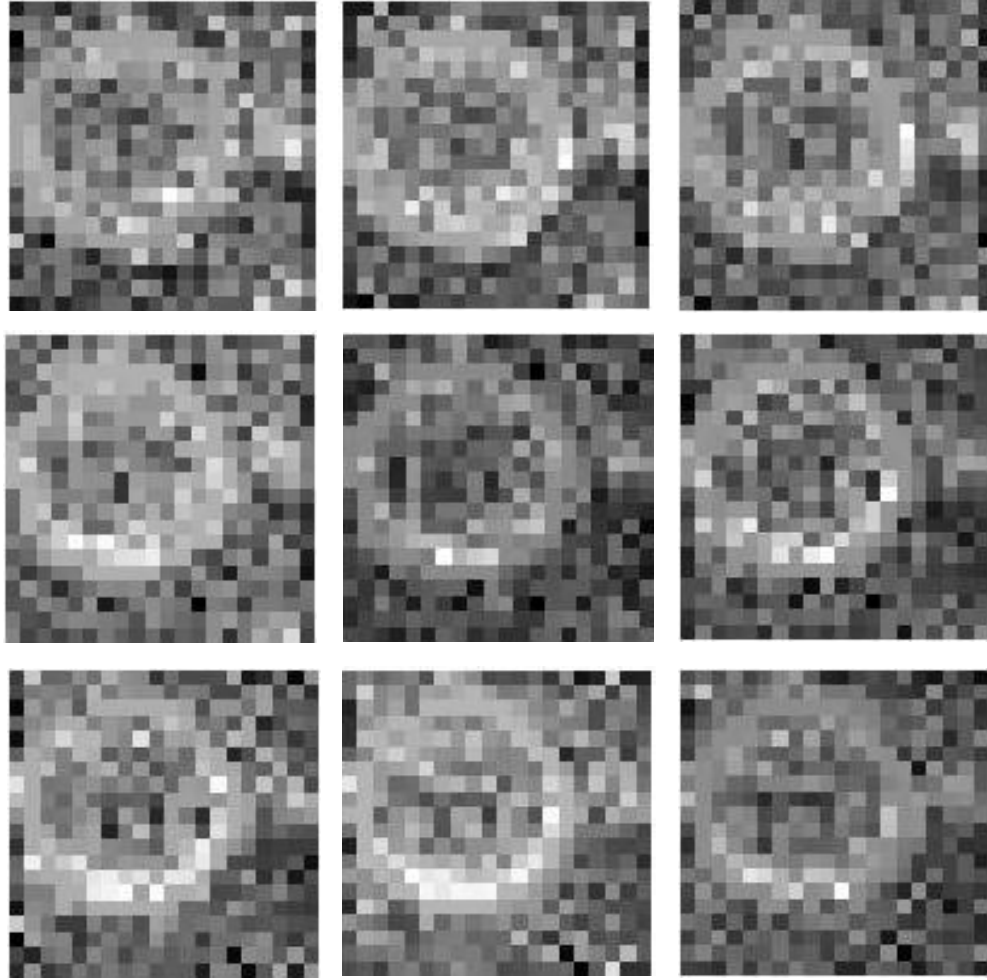


Figure 24 The full reconstruction result of semi-rigid constraints with penalty weights for boundary pixels equal to  $1 \times 10^{10}$  and for inner pixels equal to 10. The error is  $e=13.2$ .



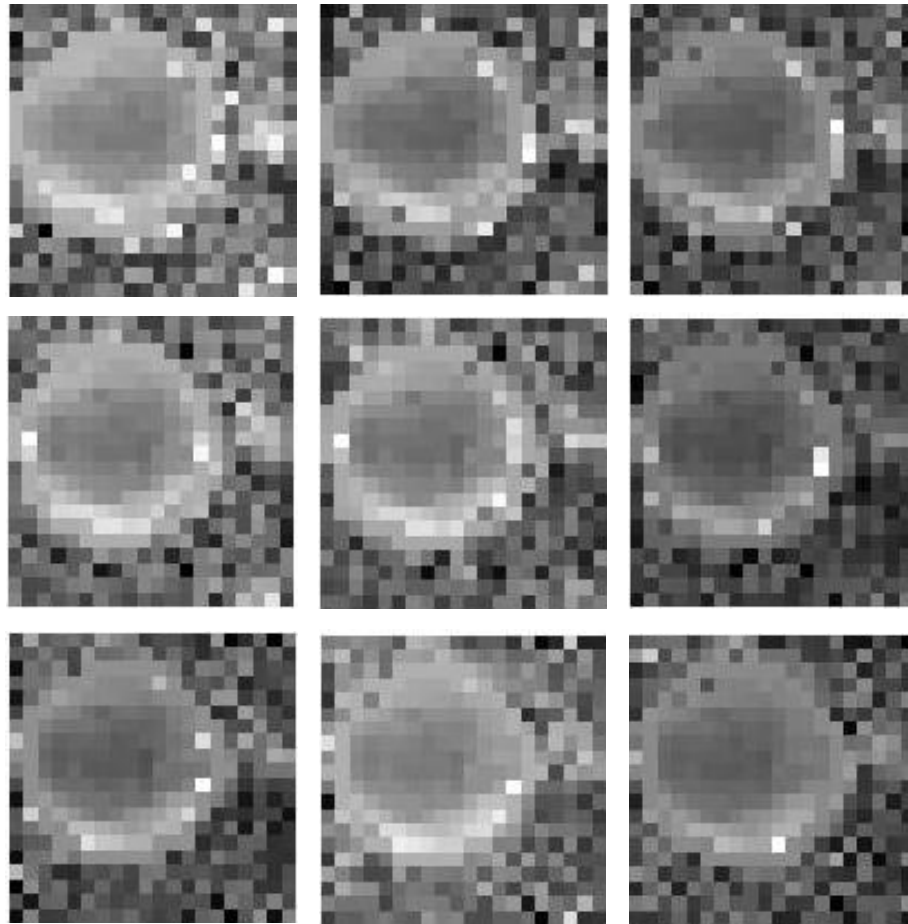


Figure 25 The full reconstruction result of semi-rigid constraints with penalty weights for boundary pixels equal to  $1 \times 10^{10}$  and for inner pixels equal to  $1 \times 10^3$ . The error is  $e=12.9$ .

The new constrained conjugate gradient methods developed in this chapter can be generalized to the image reconstruction of any composite material with emphasis on the locations and orientations of the boundaries of the fillers.

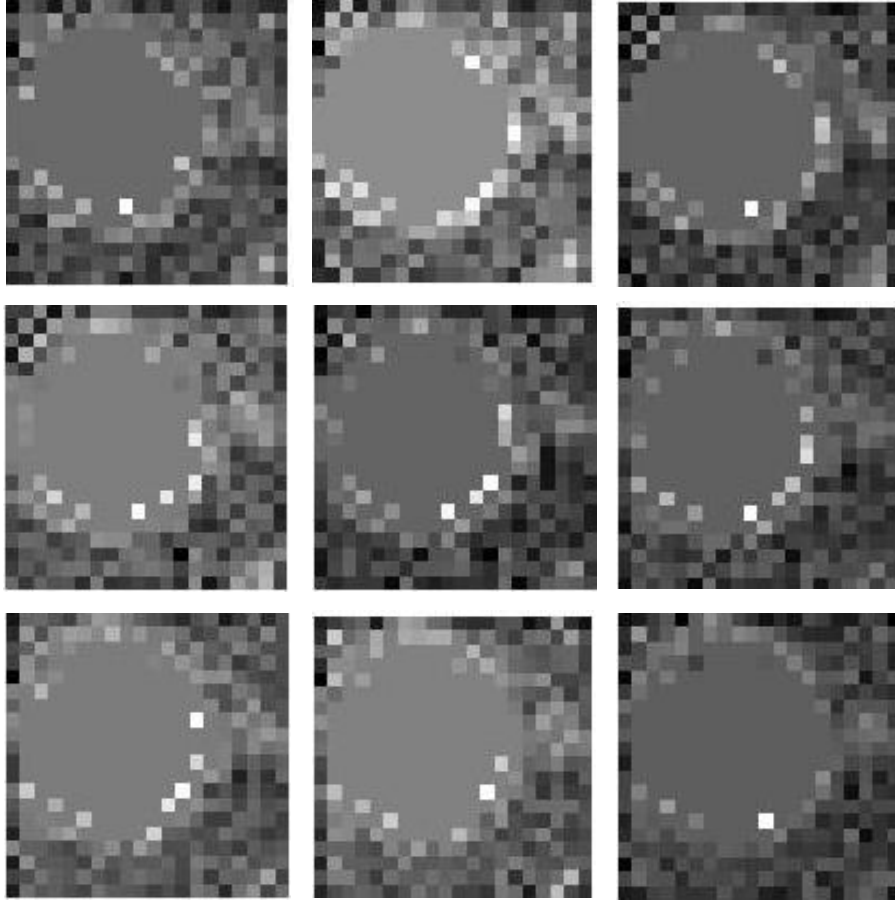


Figure 26 The full reconstruction result of semi-rigid constraints with penalty weights for both boundary and inner pixels equal to  $1 \times 10^{10}$ . The error is  $e=16.5$ .

### ***3.6 Evaluation and Comparison***

The quasi-Newton method with line search is used as a comparison with the proposed constrained conjugate gradient methods. When the constraints are only applied on the boundary, the results for different number of equations are as shown in Figure 27.

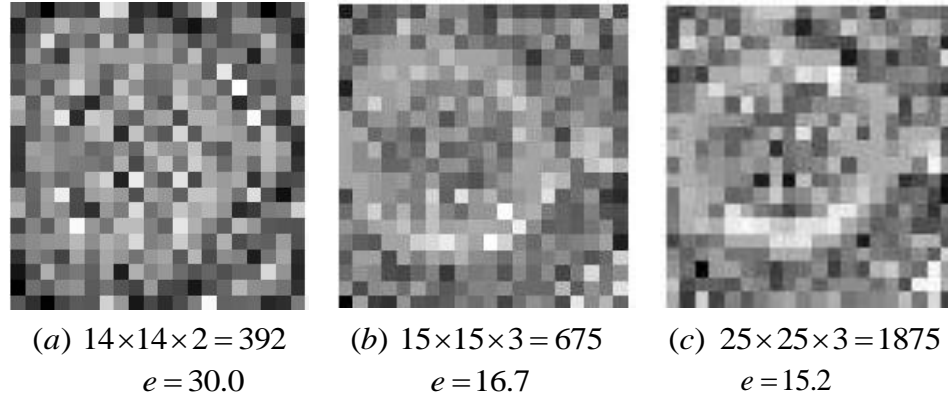


Figure 27 The reconstruction results of Quasi-Newton method with line search with fiber boundary constraints (first slices only)

The comparison of the results from the different methods is shown in Table 2. The experiments are conducted on a PC with 2.00GHz CPU and 4.00GB RAM. The number of equations used in the comparison is  $25 \times 25 \times 3 = 1875$ , and the constraints are for the boundary pixels only.

Table 2 The comparison among different methods

Optimization Method	Average error	CPU time	Iterations (generations)
Direct linear equations solution	31 (but with 7 times more equations required)	186s	N/A
Rigid constrained conjugate gradient algorithm	13.2	219s	522
Quasi-Newton method with line search	8	4230s	139
Semi-rigid constrained conjugate gradient algorithm	12.9	2025s	2512

The robustness of the methods is evaluated by using three different initial guesses (0, 1, and 100) for all pixel values to start the optimization algorithms. If the optimization results of an algorithm are the same for those three guesses, the algorithm is regarded as being robust. Results show that all these methods are robust. As can be seen from the results in Table 2, the conjugate gradient algorithm with rigid constraints and the quasi-Newton method with line search show the best results in terms of error and time efficiency. Between the quasi-Newton method and the constrained conjugate gradient algorithm, the latter shows slightly better results with less error but much better computational efficiency. The constrained conjugate gradient method is 20 times more efficient than the quasi-Newton method. The constrained conjugate gradient method realizes image compression, which is important for the surfacelet transform. It can be seen that 1875 surfacelets can reconstruct 3600 pixels reasonably well with small errors. The rigid and semi-rigid constrained conjugate gradient methods show different advantages. The rigid method produces more precise results, whereas the semi-rigid method produces more distinguishable boundaries of objects.

The proposed methods for inverse surfacelet transform are based on solving a quadratic optimization problem from linear equations. The computational time is related to the number of pixels in the images. The CPU time of 219 seconds for the rigid constrained conjugate gradient algorithm is not short for the small example images. Yet, if implemented in other languages such as C++, the computational time can be reduced.

### ***3.7 Conclusion and Future Work***

In this paper, we proposed a constrained conjugate-gradient based strategy for the inverse surfacelet transform to complete the surfacelet transform formalism. By

identifying and applying constraints on important pixels of interest, features can be preserved and retrieved during reconstruction. The proposed methods of inverse surfacelet transform with constraints are able to reconstruct images with fewer surfacelets than image pixels for the purpose of compression, by utilizing the prior knowledge of geometric features. Compared to the generic image compression methods, our method allows us to preserve boundary information of features more efficiently in material images, in addition to the integrated capability of feature identification.

In future, the proposed algorithm will be further optimized for the improvement of computational efficiency, which will enable larger images of more complex material microstructures to be processed. Parallel computing and a machine-oriented language can be utilized. Furthermore, the prior knowledge of microstructure characteristics other than feature geometry, such as mechanics of materials, can also be considered.

## CHAPTER 4

### COMPOSITE SURFACELETS

It has been demonstrated in Chapter 3 that existing primitive surfacelets are able to identify inner boundaries of material microstructures with simple geometries. In this chapter, in order to increase the flexibility and efficiency of feature identification, the existing primitive surfacelets are extended by composite surfacelets. Particularly, cubic and v-joint surfacelets are developed, as two examples.

It should be noted that the convolution method, Radon transform, and Hough transform can also identify geometric features. However, composite surfacelets are essentially different from them in the following senses.

As stated in Section 2.5 that the method of convolution is able to find the largest integrals and therefore identify geometric features. However, it is not suitable for heterogeneous material modeling for the following three reasons. Firstly, the method of convolution only returns the largest integrals for feature identification, and other smaller integrals are ignored for restoration. However, these smaller integrals are also important in the full reconstruction of the material images by inverse surfacelet transform. Secondly, in computer-aided material modeling, the material images are only the media for us to understand the material compositions and structures. We care the most about the feature geometries, instead of the detailed pixel values on them. However, the method of convolution only returns the pixels and their values of the matching features, instead of the extracted geometric information. Lastly, the searching step size of the method of convolution is always one pixel's space. However, in the method of largest surface integrals, the step size is flexible. This can effectively enhance the searching efficiency.

In addition, Hough transform is able to identify linear or spherical features, but it is not designed for image compression and reconstruction.

Last but not least, composite surfacelets can provide thickness information of features. In contrast, the traditional Radon or Hough transform only considers edge feature without thickness information.

## 4.1 Cubic Surfacelet

### 4.1.1 The construction of a cubic surfacelet

The cubic surfacelet is constructed by three sets of parallel 3D ridgelets or planar surfacelets that are perpendicular to  $x$ -,  $y$ -, and  $z$ -axis respectively, as shown in Figure 28. The equation of a 3D ridgelet is shown in Eqn. (2.1). Its implicit surface portion is used for the construction of a cubic implicit surface. The cubic surfacelet can then be constructed by the combination of the cubic implicit surface and a wavelet function.

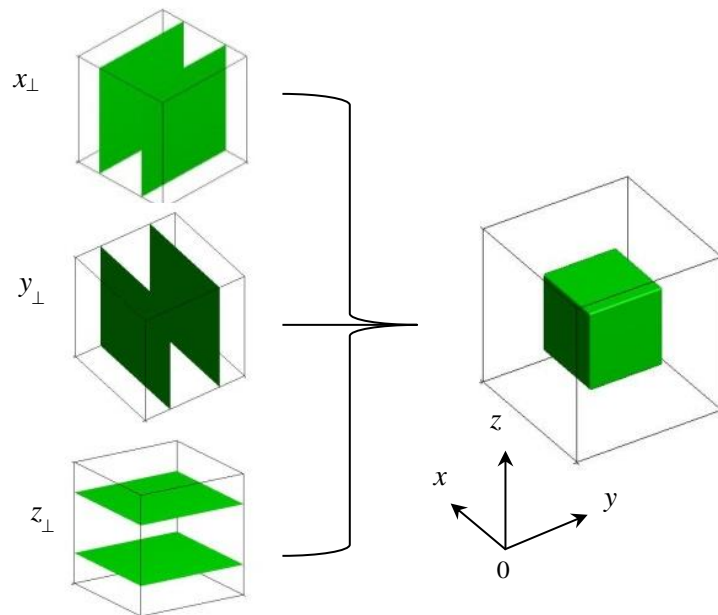


Figure 28 The scheme for the construction of the cubic surfacelet from three sets of two parallel ridgelets perpendicular to  $x$ -,  $y$ -, and  $z$ -axis

#### 4.1.1.1 The construction of a rectangular column in the cubic surfacelet

To show the construction of a cubic implicit surface, the construction of a rectangular column is shown first. A rectangular column can be constructed by two sets of parallel planes. For example, if the two sets of parallel planes are defined as  $y=a$  and  $y=b$ ,  $x=c$  and  $x=d$  respectively, as illustrated in Figure 29, the first set of two planes perpendicular to the  $x$ -axis, denoted by  $x_{\perp}$ , can be represented implicitly as  $\rho_1(x, y, z) = (x-c)(x-d) = 0$ . Similarly, the  $y_{\perp}$  set can be represented as  $\rho_2(x, y, z) = (y-a)(y-b) = 0$ . Here,  $a, b, c, d$  are translation parameters of the individual plane. For both  $x_{\perp}$  and  $y_{\perp}$ , the isovalues of the spatial points which are not on the surfaces are negative between the two planes and positive outside. Therefore, the rectangular column intercepted by the two sets of planes can be constructed by the intersection operation of the two implicit functions.

According to the R-function representations [106, 107], the union of two implicit functions  $\rho_1$  and  $\rho_2$  is  $\min(\rho_1, \rho_2)$ , and can also be represented as

$$\rho_{1\cup 2} = \frac{1}{2}(\rho_1 + \rho_2 - \sqrt{\rho_1^2 + \rho_2^2 - 2\rho_1\rho_2}) = 0 \quad (4.1)$$

The intersection of the two implicit functions is  $\max(\rho_1, \rho_2)$ , and can also be represented as

$$\rho_{1\cap 2} = \frac{1}{2}(\rho_1 + \rho_2 + \sqrt{\rho_1^2 + \rho_2^2 - 2\rho_1\rho_2}) = 0$$



$$\rho_1(x, y, z) = (x - c)(x - d) = 0$$

$$\rho_2(x, y, z) = (y - a)(y - b) = 0$$

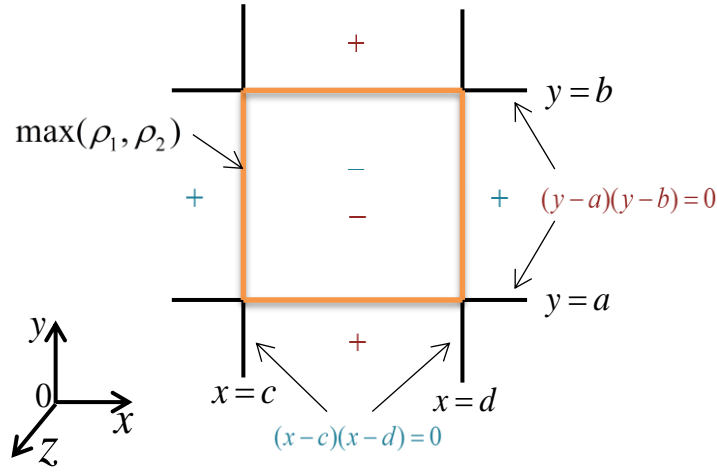


Figure 29 The construction of a column along z-axis with rectangular cross-section from two sets of two parallel planes in x- and y- axis

#### 4.1.1.2 The construction of a cubic implicit surface

Similar to the construction of the  $x_{\perp}$  and  $y_{\perp}$  sets in Section 4.1.1.1, the third set of planes, which is the  $z_{\perp}$  set, can be constructed by the planes of  $z=e$  and  $z=g$ . It can be represented as  $\rho_3(x, y, z) = (z - e)(z - g) = 0$ , where  $e$  and  $g$  are translation parameters of the two planes along the z-axis. When the intersection operation is conducted to the  $z_{\perp}$  set  $\rho_3$  and the rectangular column  $\rho_{1 \cap 2}$  intercepted by  $x_{\perp}$  and  $y_{\perp}$ , a cubic implicit surface can be constructed.

Therefore the cubic implicit surface formed by  $\rho_1$ ,  $\rho_2$ , and  $\rho_3$  is

$$\rho_c = \frac{1}{2}(\rho_{1 \cap 2} + \rho_3 + \sqrt{\rho_{1 \cap 2}^2 + \rho_3^2 - 2\rho_{1 \cap 2}\rho_3}) = 0.$$

The final form of  $\rho_c$  in the cubic surfacelet is shown in Section 4.1.2.

#### 4.1.2 The derivation of the cubic implicit surface function with three dimensional translation and rotation

Six parameters are used to decide the location and orientation of a cubic surfacelet in 3D space, three for the translation along x-, y-, and z-axis and three for the rotation about these axes. Suppose that the sizes of the cube are  $l_1$ ,  $l_2$  and  $l_3$ . They are constant once the shape of the cubic surfacelet is determined. The translation parameters  $a$ ,  $b$ ,  $c$ ,  $d$ ,  $e$  and  $g$  are related by  $b=a+l_1$ ,  $d=c+l_2$ , and  $g=e+l_3$ . Therefore, the three translation parameters along the x-, y-, and z- axis can be assigned as the translation of the center point of the cube. With the translation and rotation involved, the implicit function representation of the three sets of planes  $\rho_1$ ,  $\rho_2$ , and  $\rho_3$  can be derived. The details are discussed as follows, and the scheme is illustrated in Figure 30.

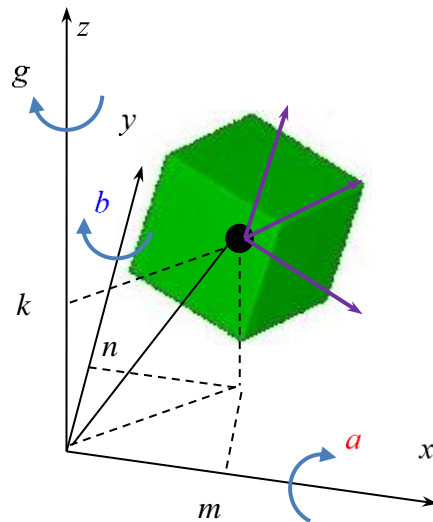


Figure 30 The three dimensional translation and rotation of a cubic implicit surface

Suppose  $\alpha$ ,  $\beta$  and  $\gamma$  are the rotation angles around the x-, y-, and z-axis respectively. Then the rotation matrices are

$$A_x = \begin{bmatrix} 1 & 0 & 0 \\ 0 & \cos \alpha & -\sin \alpha \\ 0 & \sin \alpha & \cos \alpha \end{bmatrix}, A_y = \begin{bmatrix} \cos \beta & 0 & \sin \beta \\ 0 & 1 & 0 \\ -\sin \beta & 0 & \cos \beta \end{bmatrix}, A_z = \begin{bmatrix} \cos \gamma & -\sin \gamma & 0 \\ \sin \gamma & \cos \gamma & 0 \\ 0 & 0 & 1 \end{bmatrix}$$

The overall rotation matrix that include three rotations is

$$A = A_z \cdot A_y \cdot A_x = \begin{bmatrix} \cos \beta \cos \gamma & \sin \alpha \sin \beta \cos \gamma - \cos \alpha \sin \gamma & \cos \alpha \sin \beta \cos \gamma + \sin \alpha \sin \gamma \\ \cos \beta \sin \gamma & \sin \alpha \sin \beta \sin \gamma + \cos \alpha \cos \gamma & \cos \alpha \sin \beta \sin \gamma - \sin \alpha \cos \gamma \\ -\sin \beta & \sin \alpha \cos \beta & \cos \alpha \cos \beta \end{bmatrix}.$$

After the rotations, the new coordinates  $(x', y', z')$  for the point  $(x, y, z)$

become

$$\begin{bmatrix} x' \\ y' \\ z' \end{bmatrix} = A \begin{bmatrix} x \\ y \\ z \end{bmatrix} = \begin{bmatrix} \cos \beta \cos \gamma x + (\sin \alpha \sin \beta \cos \gamma - \cos \alpha \sin \gamma) y + (\cos \alpha \sin \beta \cos \gamma + \sin \alpha \sin \gamma) z \\ \cos \beta \sin \gamma x + (\sin \alpha \sin \beta \sin \gamma + \cos \alpha \cos \gamma) y + (\cos \alpha \sin \beta \sin \gamma - \sin \alpha \cos \gamma) z \\ -\sin \beta x + \sin \alpha \cos \beta y + \cos \alpha \cos \beta z \end{bmatrix}$$

Suppose that  $m$ ,  $n$ , and  $k$  are the  $x$ -,  $y$ -, and  $z$ -coordinates of the center of the cube respectively. The implicit functions of the planes with orientation and translations are

$$\begin{aligned} & \rho_1(l_1; m, \alpha, \beta, \gamma; x, y, z) \\ & = (x' - a)(x' - a - l_1) \\ & = ((\cos \beta \cos \gamma x + (\sin \alpha \sin \beta \cos \gamma - \cos \alpha \sin \gamma) y \\ & \quad + (\cos \alpha \sin \beta \cos \gamma + \sin \alpha \sin \gamma) z - m - l_1 / 2) \\ & \quad \times (\cos \beta \cos \gamma x + (\sin \alpha \sin \beta \cos \gamma - \cos \alpha \sin \gamma) y \\ & \quad + (\cos \alpha \sin \beta \cos \gamma + \sin \alpha \sin \gamma) z - m + l_1 / 2)) \\ & = 0 \end{aligned}$$

$$\begin{aligned}
& \rho_2(l_2; n, \alpha, \beta, \gamma; x, y, z) \\
&= (y' - c)(y' - c - l_2) \\
&= ((\cos \beta \sin \gamma x + (\sin \alpha \sin \beta \sin \gamma + \cos \alpha \cos \gamma) y \\
&\quad + (\cos \alpha \sin \beta \sin \gamma - \sin \alpha \cos \gamma) z - n - l_2 / 2) \\
&\quad \times (\cos \beta \sin \gamma x + (\sin \alpha \sin \beta \sin \gamma + \cos \alpha \cos \gamma) y \\
&\quad + (\cos \alpha \sin \beta \sin \gamma - \sin \alpha \cos \gamma) z - n + l_2 / 2)) \\
&= 0
\end{aligned}$$

$$\begin{aligned}
& \rho_3(l_3; k, \alpha, \beta, \gamma; x, y, z) \\
&= (z' - e)(z' - e - l_3) \\
&= ((-\sin \beta x + \sin \alpha \cos \beta y + \cos \alpha \cos \beta z - k - l_3 / 2) \\
&\quad \times (-\sin \beta x + \sin \alpha \cos \beta y + \cos \alpha \cos \beta z - k + l_3 / 2)) \\
&= 0
\end{aligned}$$

When these functions are substituted into the R-function, the explicit function of the implicit surface in the cubic surfacelet can be obtained. The final implicit function is

$$\begin{aligned}
& \rho_c(l_1, l_2, l_3; m, n, k, \alpha, \beta, \gamma; x, y, z) \\
&= \frac{1}{2} [\rho_{1\cap 2} + (-\sin \beta x + \sin \alpha \cos \beta y + \cos \alpha \cos \beta z - e) \\
&\quad \times (-\sin \beta x + \sin \alpha \cos \beta y + \cos \alpha \cos \beta z - e - l_3) \\
&\quad + \sqrt{\rho_{1\cap 2}^2 + ((-\sin \beta x + \sin \alpha \cos \beta y + \cos \alpha \cos \beta z - e) \\
&\quad \quad (-\sin \beta x + \sin \alpha \cos \beta y + \cos \alpha \cos \beta z - e - l_3))^2} \\
&\quad - 2\rho_{1\cap 2}((-\sin \beta x + \sin \alpha \cos \beta y + \cos \alpha \cos \beta z - e) \\
&\quad \quad (-\sin \beta x + \sin \alpha \cos \beta y + \cos \alpha \cos \beta z - e - l_3))] \\
&= 0
\end{aligned}$$

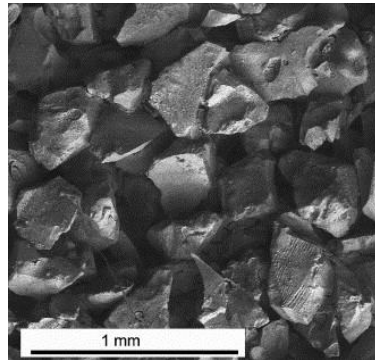
where

$$\begin{aligned}
\rho_{1\cap 2} = & \frac{1}{2} \left( (\cos \beta \cos \gamma x + (\sin \alpha \sin \beta \cos \gamma - \cos \alpha \sin \gamma) y \right. \\
& + (\cos \alpha \sin \beta \cos \gamma + \sin \alpha \sin \gamma) z - m - l_1 / 2) \\
& (\cos \beta \cos \gamma x + (\sin \alpha \sin \beta \cos \gamma - \cos \alpha \sin \gamma) y \\
& + (\cos \alpha \sin \beta \cos \gamma + \sin \alpha \sin \gamma) z - m + l_1 / 2) \\
& + ((\cos \beta \sin \gamma x + (\sin \alpha \sin \beta \sin \gamma + \cos \alpha \cos \gamma) y \\
& + (\cos \alpha \sin \beta \sin \gamma - \sin \alpha \cos \gamma) z - n - l_2 / 2) \\
& (\cos \beta \sin \gamma x + (\sin \alpha \sin \beta \sin \gamma + \cos \alpha \cos \gamma) y \\
& + (\cos \alpha \sin \beta \sin \gamma - \sin \alpha \cos \gamma) z - n + l_2 / 2) \\
& \left. + \sqrt{ \left( (\cos \beta \cos \gamma x + (\sin \alpha \sin \beta \cos \gamma - \cos \alpha \sin \gamma) y \right. \right. \\
& + (\cos \alpha \sin \beta \cos \gamma + \sin \alpha \sin \gamma) z - m - l_1 / 2) \\
& (\cos \beta \cos \gamma x + (\sin \alpha \sin \beta \cos \gamma - \cos \alpha \sin \gamma) y \\
& + (\cos \alpha \sin \beta \cos \gamma + \sin \alpha \sin \gamma) z - m + l_1 / 2) \Big)^2 \\
& + ((\cos \beta \sin \gamma x + (\sin \alpha \sin \beta \sin \gamma + \cos \alpha \cos \gamma) y \\
& + (\cos \alpha \sin \beta \sin \gamma - \sin \alpha \cos \gamma) z - n - l_2 / 2) \\
& (\cos \beta \sin \gamma x + (\sin \alpha \sin \beta \sin \gamma + \cos \alpha \cos \gamma) y \\
& + (\cos \alpha \sin \beta \sin \gamma - \sin \alpha \cos \gamma) z - n + l_2 / 2) \Big)^2 } \\
& + \left. \left( -2 \left( (\cos \beta \cos \gamma x + (\sin \alpha \sin \beta \cos \gamma - \cos \alpha \sin \gamma) y \right. \right. \right. \\
& + (\cos \alpha \sin \beta \cos \gamma + \sin \alpha \sin \gamma) z - m - l_1 / 2) \\
& (\cos \beta \cos \gamma x + (\sin \alpha \sin \beta \cos \gamma - \cos \alpha \sin \gamma) y \\
& + (\cos \alpha \sin \beta \cos \gamma + \sin \alpha \sin \gamma) z - m + l_1 / 2) \\
& \left. \left( (\cos \beta \sin \gamma x + (\sin \alpha \sin \beta \sin \gamma + \cos \alpha \cos \gamma) y \right. \right. \\
& + (\cos \alpha \sin \beta \sin \gamma - \sin \alpha \cos \gamma) z - n + l_2 / 2) \\
& (\cos \beta \sin \gamma x + (\sin \alpha \sin \beta \sin \gamma + \cos \alpha \cos \gamma) y \\
& + (\cos \alpha \sin \beta \sin \gamma - \sin \alpha \cos \gamma) z - n + l_2 / 2) \Big) \right)
\end{aligned}$$

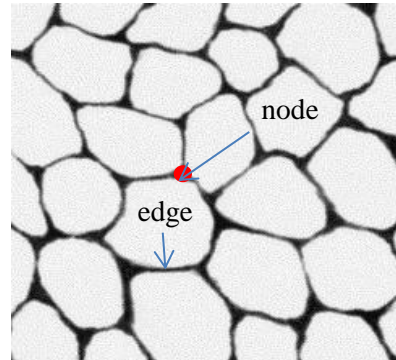
## 4.2 V-joint Surfacelet

General polyhedral shapes other than the rectangular ones are also seen in microstructures. The rectangular feature is only a special case of the polyhedral ones. The grain shapes of many traditional materials are very close to polyhedrons, such as the forms of polygonal crystals in many alloys. One example is  $\text{Al}_2\text{O}_3$  particle shown in Figure 31(a). The two-phase structure of  $\text{Al}_2\text{O}_3$ -Fe obtained through infiltration of the

porous ceramic matrix formed by the  $\text{Al}_2\text{O}_3$  powder in Figure 31(a) is shown in Figure 31(b) [108].



(a) SEM image of  $\text{Al}_2\text{O}_3$  ceramic



(b) Image of ceramic–metal composites (dark region is Fe, and light region is  $\text{Al}_2\text{O}_3$ )

Figure 31 Microstructure of  $\text{Al}_2\text{O}_3$  and  $\text{Al}_2\text{O}_3$ –Fe composites [108]

Another significant characteristic about the powder composite materials and many alloys is that the grains are compactly packed and the binding phase is in a network form with nodes and connecting edges, as shown in Figure 31(b). Together with the fact that the polyhedral grain features have more irregular shapes than the rectangular feature, the scheme in Chapter 3 is not effective to represent or identify the grains. Instead, representing and identifying the binding phase including nodes and edges, such as the Fe phase in Figure 31, is a better choice. Based on the geometric similarity, the cubic surfacelet can be parameterized as very narrow rectangles to identify the edges. However, the information of the node locations cannot be directly captured.

The v-joint surfacelet is a new composite surfacelet that unites two narrow rectangular cubic surfacelets to form a V shape. The V shape can identify both the node locations and edge orientations simultaneously. The construction of the v-joint composite surfacelet is described as follows and illustrated in Figure 32. The shape parameters of

the v-joint surfacelet are the width  $W$ , the edge length  $L$ , and the depth  $D$ . Two narrow cubic surfacelets with the same sizes are combined at the ends along the edge length direction to form a *pivot* with a *v-joint angle*  $\theta$ , by the union operation for implicit surfaces. During the surfacelet transform, the shape parameters are fixed. They are adjusted to match those of the connection phase of the material at the beginning of the surfacelet transform. The location parameters, including the overall translation distances, rotation angles, and v-joint angle  $\theta$ , vary. Note that  $\theta$  is not defined as a shape parameter. This allows for more flexibility in pattern matching.

The union between the two rectangular implicit surfaces in the v-joint surfacelet is done by the R-function similar to Eqn.(4.1). There are also seven location parameters to locate a v-joint surfacelet, three ( $m$ ,  $n$ , and  $k$ ) for the translation, three ( $\alpha$ ,  $\beta$ , and  $\gamma$ ) for the orientation, and the v-joint angle  $\theta$ . The three translation parameters along the x-, y-, and z-axis can be assigned as the translation of the pivot. The rotation angle around the x-, y-, and z-axis are  $\alpha$ ,  $\beta$  and  $\gamma$  respectively. The rotation and translation methods for the v-joint surfacelet are exactly the same as the cubic surfacelet in Section 4.1. The final form of the implicit surface in the v-joint surfacelet is shown as following.

$$\begin{aligned}
& \rho_v(W, L, D; m, n, k, \alpha, \beta, \gamma, \theta; x, y, z) \\
&= \frac{1}{2} [\rho_{c1}(W, L, D; m, n, k + \frac{L}{2}, \alpha, \beta, \gamma; x, y, z) \\
&\quad + \rho_{c2}(W, L, D; m, n, k + \frac{L}{2}, \alpha, \beta, \gamma + \theta; x, y, z) \\
&\quad - \sqrt{\rho_{c1}^2(W, L, D; m, n, k + \frac{L}{2}, \alpha, \beta, \gamma; x, y, z) \\
&\quad + \rho_{c2}^2(W, L, D; m, n, k + \frac{L}{2}, \alpha, \beta, \gamma + \theta; x, y, z)} \\
&\quad - 2\rho_{c1}(W, L, D; m, n, k + \frac{L}{2}, \alpha, \beta, \gamma; x, y, z) \\
&\quad \cdot \rho_{c2}(W, L, D; m, n, k + \frac{L}{2}, \alpha, \beta, \gamma + \theta; x, y, z) \\
&= 0
\end{aligned}$$

where  $\rho_{c1}$  and  $\rho_{c2}$  are the two respective rectangular implicit surfaces in the v-joint.

An example for identifying the connection features with v-joint composite surfacelets will be given in Chapter 5.

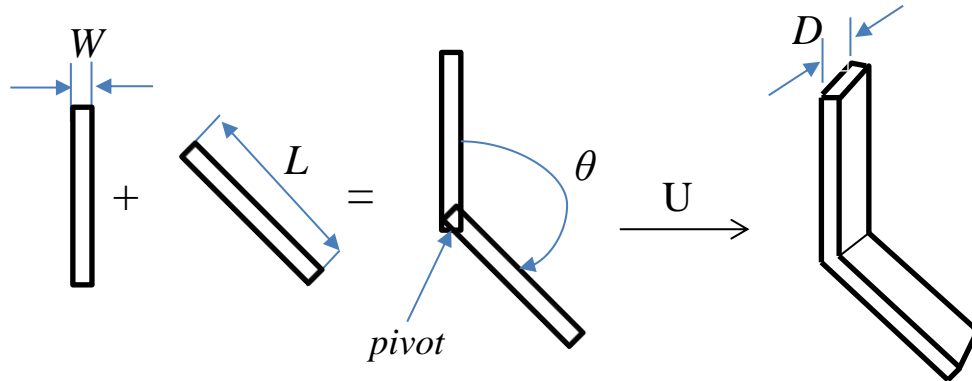


Figure 32 The construction of v-joint composite surfacelet based on two cubic surfacelets composites

### 4.3 Feature Identification with the Cubic and V-joint Surfacelets

The feature identification with composite surfacelets is based on the largest surface integrals, similar to the one based on the primitive surfacelets [4]. Typically, the



locations and orientations of the features are of interest to identify. Geometric information of the target features, such as the shape and size, are prior knowledge to us. The features are captured by examining the surface integrals. In addition, some image processing methods can be used to increase the contrast and highlight the features by increasing the greyscale values of the feature pixels.

When a surfacelet is overlapped with the feature (e.g., a cylindrical surfacelet is overlapped with a fiber surface), its corresponding surface integral value is larger than those of other surfacelets. Therefore surface integrals help determine the positions and orientations of the target feature geometries. If there is only one feature geometry to identify, its position and orientation can be directly estimated by the corresponding surfacelet with the largest integral. This can be realized by sorting the surface integrals from the results of surfacelet transform. If there are more than one feature geometry, the largest integral for one feature geometry can be very close to the one for another feature geometry, because some surfacelets can be overlapped with multiple feature geometries. In this case, the integrals are grouped into different clusters according to their positions and orientations. The largest integral or the best estimate based on some criteria in each cluster determines the feature geometry. This clustering process is regarded as an averaging or homogenization scheme in the multi-resolution surfacelet representation.

#### **4.3.1 Feature identification with the cubic surfacelet**

In existing materials, it is common that the cubic or rectangular particles of interest have various sizes. In order to identify all feature geometries, the shape parameters of the cubic surfacelet are chosen to be identical to the smallest particle. For those particles that are larger than the surfacelet, multiple surfacelets with the largest

integrals are needed to identify the location and orientation of one particle. The union of these surfacelets, which is the overall profile of the surfacelets, is able to show the location and orientation of a particle. For those particles almost in the same size as the surfacelet, only the largest integral is needed to identify the location and orientation of one particle.

#### **4.3.2 Feature identification with the v-joint surfacelet**

It can be seen in Figure 31(b) that the greyscale pixel values and the widths of the nodes and edges for the metal binding phase are not uniform. The image can be processed so that the binding phase has larger pixel values. After the surfacelet transform is conducted, most of the largest integrals will be from the brighter and wider nodes and edges. Therefore, in order to identify those darker or narrower feature geometries, much more surfacelets are needed.

Most of the surfacelets for those brighter and wider nodes and edges do not exactly overlap with the feature geometries. Therefore, in order to clearly capture the feature geometries, those surfacelets with correct locations and orientations should be extracted. In this dissertation, the scheme of averaging locations and orientations of v-joint surfacelets is used for each feature geometry. The process of feature identification is graphically illustrated in Figure 33 and summarized as the flow chart in Figure 34. The seven steps are described as follows.

In the first step, the shape parameters of the v-joint surfacelet are designed to match the edge lengths and angles in-between. Then the surfacelet transform is conducted to obtain the surface integrals, as illustrated in Figure 33(a).

In the second step, the number of surfacelets with the largest integrals is chosen such that all important feature geometries can be covered, as illustrated in Figure 33(b).

In the third step, these surfacelets are grouped into clusters based on relative locations and orientations so that all surfacelets in the same cluster are for the same feature geometry, as illustrated in Figure 33(c).

In the fourth step, the average pivot location and orientation of each cluster are calculated. A new surfacelet with the average location and orientation is created, and all old surfacelets are discarded, as illustrated in Figure 33(d). After this step that reduces the resolution in the surfacelet domain, the number of surfacelets for feature identification is significantly reduced. It should be noted that if there are multiple surfacelets for one feature geometry, the pivots of these surfacelets are distributed around the node. Because the nodes in the images actually have non-zero areas, the average location is able to approximately reflect the geometric center of the node.

For feature identification, the center of the node is desired. Since the three edges at one node need at least two v-joint surfacelets to cover, these two surfacelets should be properly coordinated to form a neat one-node and three-branch geometry. Therefore, in the fifth step, those surfacelets with close pivot locations are translated to their average pivot location so that two surfacelets for one node are connected and the locations of the nodes are identified, as illustrated in Figure 33(e). The reason that the surfacelets for different aspects of the three edges at a node are not mixed in the clusters is as follows. If one of the three edges has a very large width, then most surfacelets in the cluster may locate on that edge. Then the average pivot is pulled towards that edge instead of reflecting the geometric center, because the surfacelets on that edge account for a larger

weight. With the above separate averaging steps for individual clusters for the multi-branch cases, there are no more than two surfacelets on one node so that one edge cannot overweight others. After averaging pivot locations, the v-joint surfacelets with close orientations at the same pivot location should be rotated to the average orientation.

To improve the accuracy of identification, a v-joint surfacelet can be broken into two separate cubic surfacelets and rotate each cubic surfacelet separately so that the v-angles can be further fine-tuned. Therefore, in the sixth step, the average orientations of the cubic surfacelets that share the same pivot location and have the similar orientations are calculated. The old cubic surfacelets can also be removed for better clarity and accuracy, as illustrated in Figure 33(f). In order to make the surfacelets better match the edges, the averaged cubic surfacelets are further rotated around the pivots based on the principle of largest integrals, as illustrated in Figure 33(g).

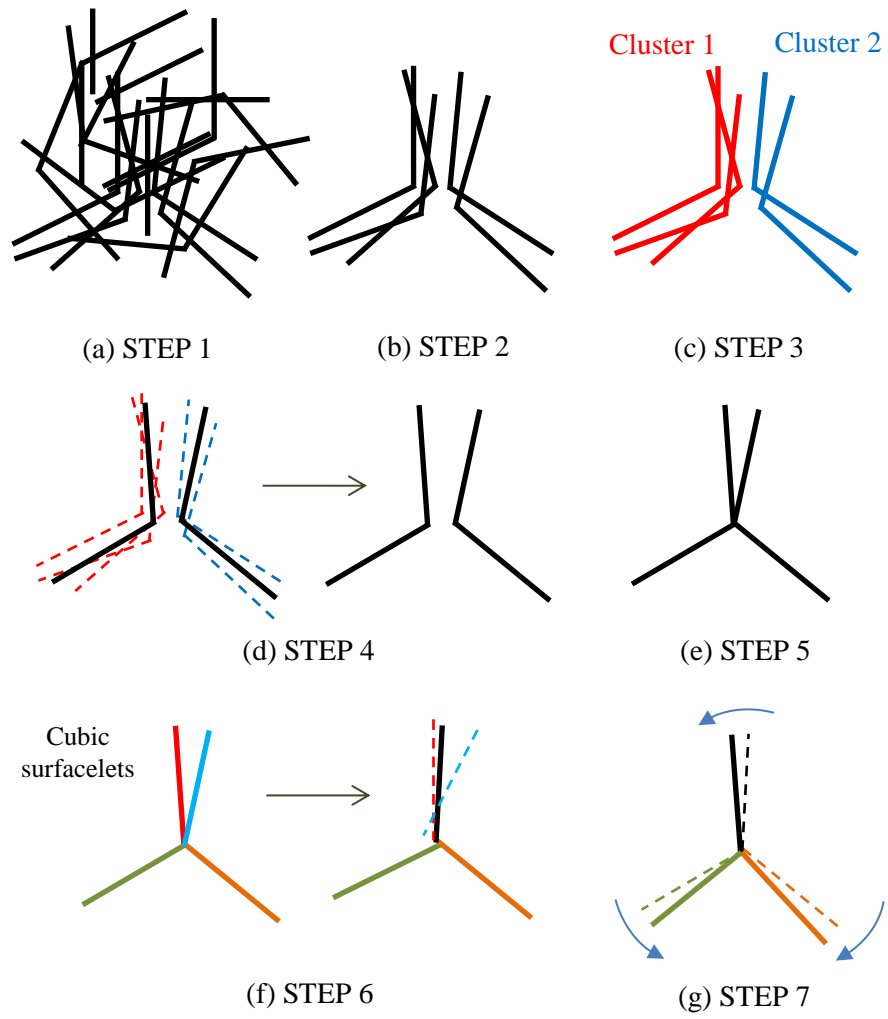


Figure 33 Graphic illustration of the feature identification process with the v-joint surfacelet

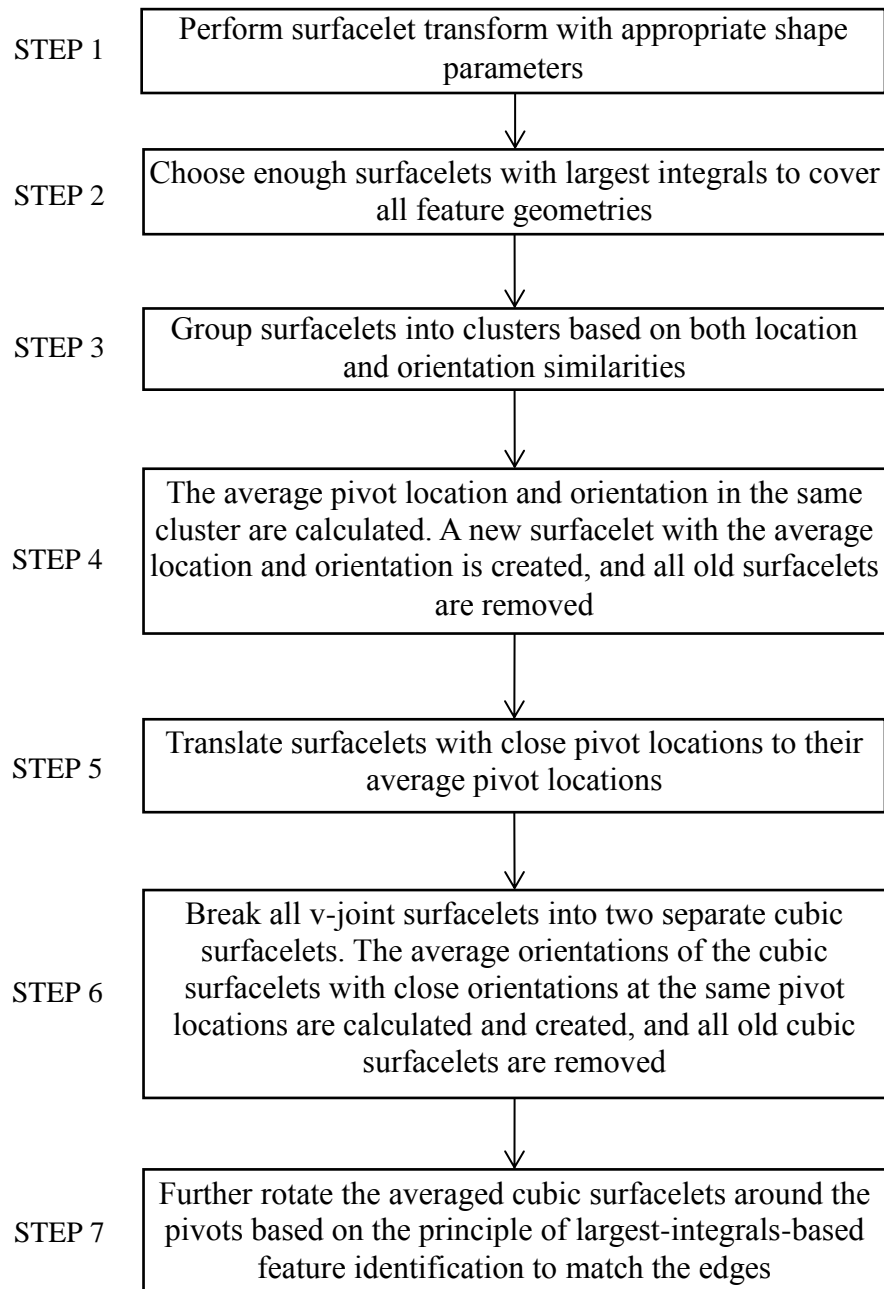


Figure 34 The process of the feature identification with the v-joint surfacelet

#### 4.4 Demonstrations and Results

In this section, the proposed cubic and v-joint surfacelets for feature identification are tested on the microstructures of nano-C60 [109] for biomolecular sensing, shown in Figure 35(a), and the Al<sub>2</sub>O<sub>3</sub>-Fe composites in Figure 31 respectively. The composite

surfacelets are implemented in MATLAB on a PC. For both examples, three slices of images are used. To better demonstrate the details, only a portion of the images is used here. The spatial domain in the images is normalized to be  $[-1,1]$  for all ranges of  $x$ ,  $y$ , and  $z$  directions. The ranges of the translation parameters are  $m$ ,  $n$ , and  $k \in [-1,1]$ , and the ranges of the rotation angles are  $\alpha$ ,  $\beta$ , and  $\gamma \in [0, 2\pi]$  to ensure that the surfacelets cover all target features.

#### **4.4.1 Cubic surfacelet to identify nano-C60 particles**

Because of the limited CPU capability of the PC, in this example, a small representative portion of the image with one particle is used, as shown in Figure 35(b). The same image is stacked three times to form the 3D slices in this example. The images are treated as 3D cross-section slices of the particle. The top and bottom boundaries of the particle are not included in the three images, as shown in Figure 35(c). Therefore, the size of the particle along  $z$ -axis direction is assumed to be large, and the corresponding shape parameter  $l_3$  is set to be a large value. The size of each image is  $76 \times 76$ , thus the total number of pixels for three images is  $P=76 \times 76 \times 3=17328$ .

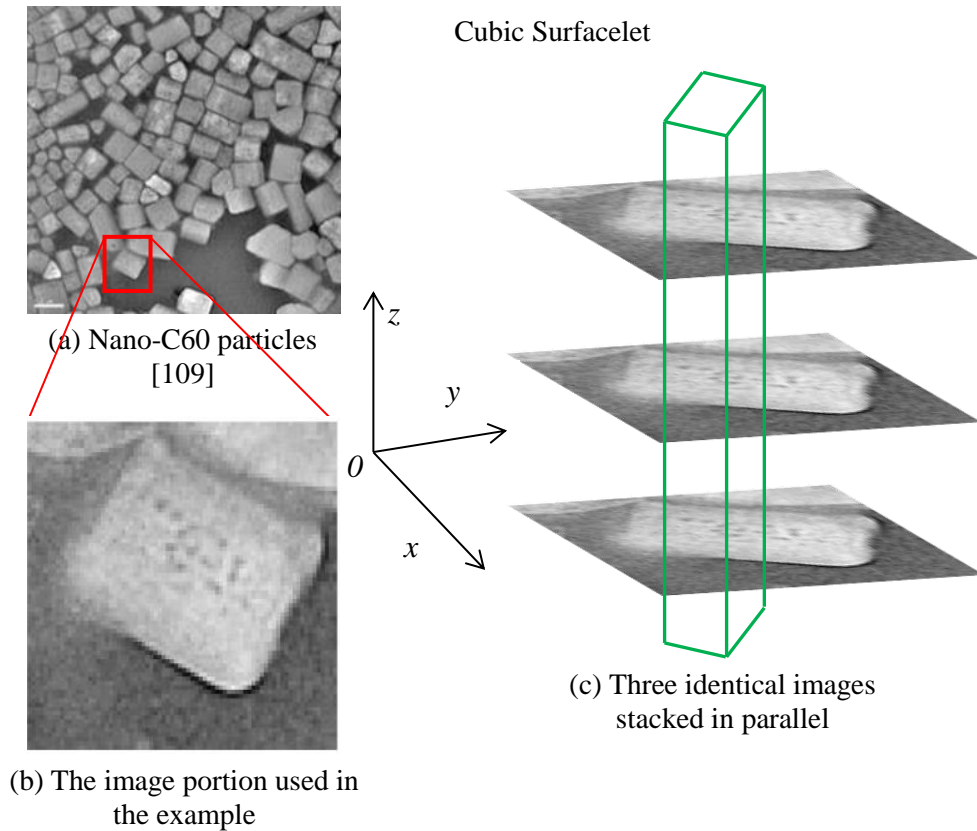


Figure 35 The 3D images of nano-C60 particle

The shape parameters of the cubic surfacelet are  $l_1=1.34$ ,  $l_2=1$ , and  $l_3=3$ , which are designed to match the size of the particle. The translation along the z-axis is set as zero. The number of cubic surfacelets used is  $m \times n \times \alpha \times \beta \times \gamma = 10 \times 10 \times 1 \times 1 \times 6 = 600$ . The surfacelet with the largest integral is used for identification. The feature identification result is shown in Figure 36.



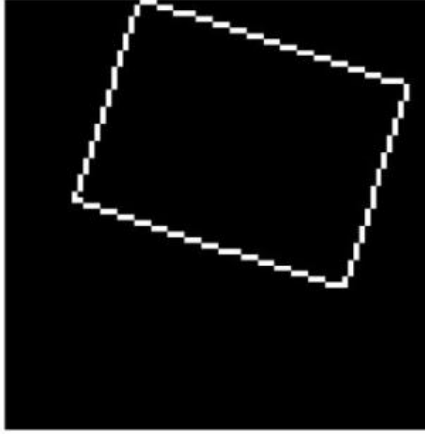


Figure 36 Identifying a rectangular feature with a cubic surfacelet with matching shape parameters

As stated in Section 4.3.1, particles in images may have varied sizes. In order to identify all feature geometries, the dimensions of the cubic surfacelet are chosen to be identical to the smallest particle. Therefore, to demonstrate the generality of feature identification based on the cubic surfacelet, a cubic surfacelet that is smaller than the rectangular particle is intentionally chosen. The number of surfacelets used is  $m \times n \times \alpha \times \beta \times \gamma = 20 \times 20 \times 1 \times 1 \times 30 = 12000$ . The shape parameters of the cubic surfacelet are  $l_1 = l_2 = 0.5$ , and  $l_3 = 3$ , and the translation along the z-axis is set as zero. Because  $l_1 = l_2$  thus the chosen cubic surfacelet is self-symmetric, the range of rotation angles  $\alpha, \beta, \gamma$  can be reduced to  $[0, \pi/2]$ . The feature identification result is shown in Figure 37. It can be seen that the size, location, and orientation of the particle can be better recognized if more integrals with the largest values are utilized.

The identified feature can be applied for the reconstruction of the original images by inverse surfacelet transform. The reconstruction is conducted with a constrained conjugate-gradient method. Only the boundary pixels are added as constraints. In this example, there is no need to translate the cubic surfacelet in the z-direction, i.e.  $k=0$ . To

decrease the computational cost, the size of each image is reduced to  $20 \times 20$ , thus the total number of pixels for three images is  $P=20 \times 20 \times 3=1200$ . The number of surfacelets used in reconstruction is  $m \times n \times \alpha \times \beta \times \gamma = 8 \times 8 \times 1 \times 1 \times 10 = 640$ . The results of reconstructed images are shown in Figure 38, where one to twenty integrals with the largest values are chosen to be constraints respectively. The data compression rate is 47%.

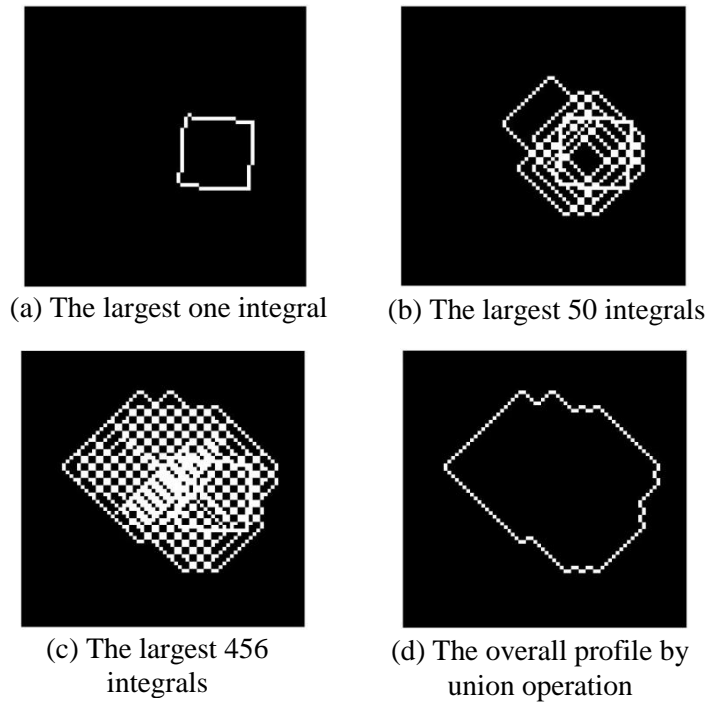


Figure 37 Identifying rectangular features with cubic surfacelets in smaller size

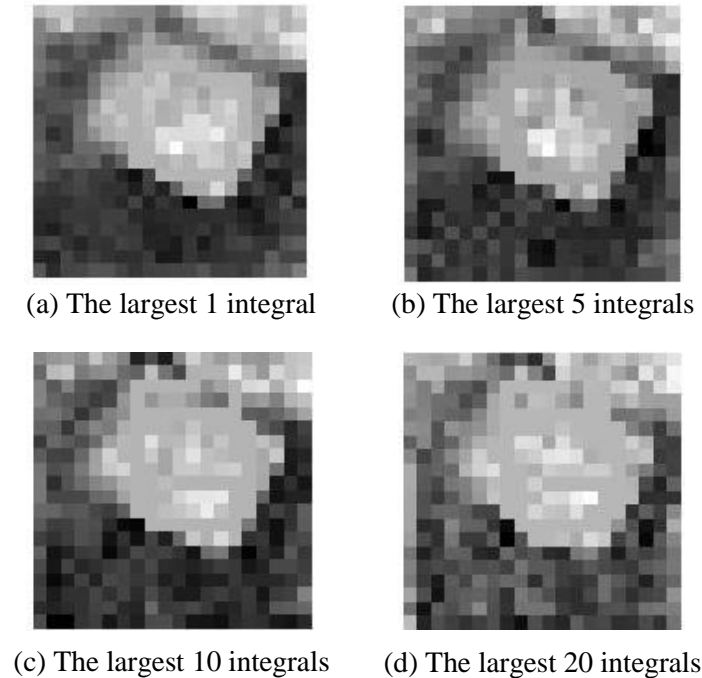


Figure 38 Image reconstruction results with different constraints of cubic surfacelets

#### 4.4.2 V-joint surfacelet to identify $\text{Al}_2\text{O}_3$ -Fe composite

$\text{Al}_2\text{O}_3$ -Fe composite in Figure 31(b) is used as the example to illustrate feature identification based on the v-joint surfacelet. Two portions are selected from the original image to test the scalability. The first one contains one grain as shown in Figure 39(a), and the second one has multiple grains as shown in Figure 39(b). Because the largest-integrals-based feature identification method requires that the feature to be identified has a larger greyscale value than the rest of the image, the images are inverted first.

Similar to the previous example in Figure 35, the same image is stacked to form three slices of 3D images. In this example, based on the estimated average size of the metal phase in the image, the shape parameters of the v-joint surfacelet are chosen as  $W=0.02$ ,  $L=0.4$ , and  $D=4$ . Similar to the example of the cubic surfacelet in Section 4.4.1, the size of the v-joint  $D$  along the z-axis direction is chosen to be larger than the image

domain  $z \in [-1, 1]$ . The v-joint angle  $\theta = 100^\circ$  is fixed. This can significantly reduce the computational time of surfacelet transform, because the dimension of the reciprocal surfacelet space is reduced without varying the v-joint angle. The number of surfacelets used here is  $m \times n \times \alpha \times \beta \times \gamma = 30 \times 30 \times 1 \times 1 \times 30 = 27000$ . There is no need to translate the v-joint surfacelet in the z-axis direction, i.e.  $k=0$ .

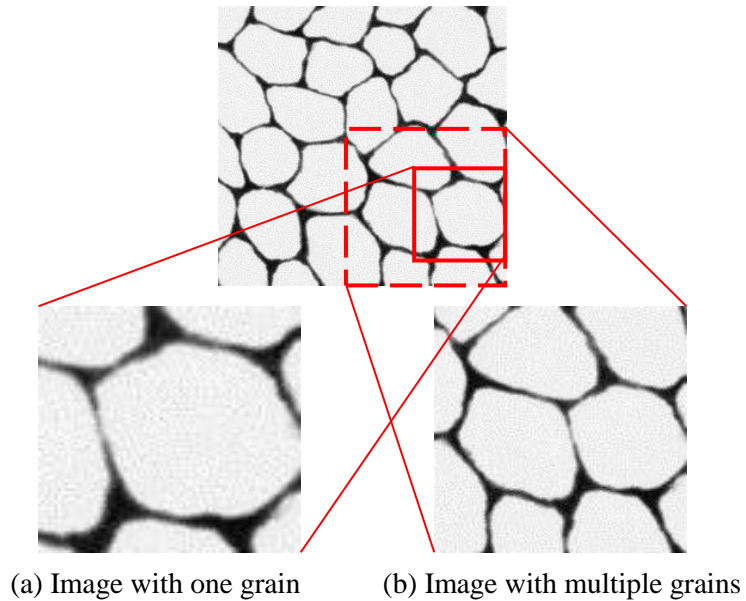


Figure 39 The two example images of  $\text{Al}_2\text{O}_3\text{-Fe}$  composites for testing the v-joint surfacelet

With the largest-integrals-based feature identification method, the identification results for different numbers of largest integrals are compared in Figure 40. It can be seen that since the values of pixels within the metal phase are not equal to each other, neither the widths of the nodes and edges, much more surfacelets are needed to identify those features with either brighter pixels or narrower geometries. As shown in Figure 40, when more than 100 largest integrals are used, most feature geometries in the image are covered after STEP 1. Then the surfacelets with similar locations and orientations are

clustered and averaged. The result after STEP 4 is shown in Figure 41(a). The number of surfacelets is reduced from 150 to 12. The result after STEP 6 is shown in Figure 41(b). The number of surfacelets is further reduced from 12 to 9. The result after STEP 7 is shown in Figure 41(c). Figure 41(d) shows the cubic surfacelets derived from the v-joint surfacelets match the feature in the original image fairly well.

In order to demonstrate the scalability of the proposed method, the image with multiple grains is also tested. The identification result is shown in Figure 42. Notice that in this example the width of the v-joint is small because it needs to match the thinnest feature in the original image. It will be increased if the original feature width is larger. In contrast, the traditional Radon or Hough transform only considers edge feature without thickness information.

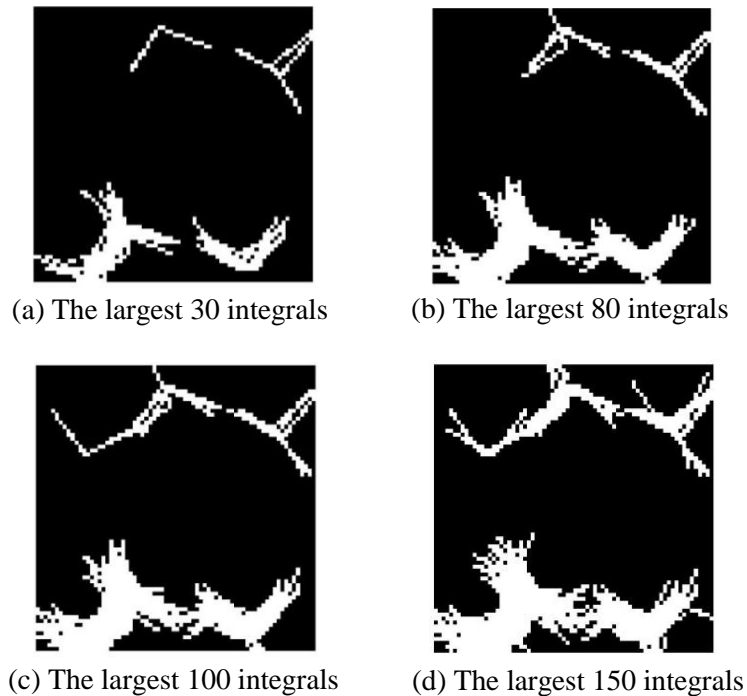
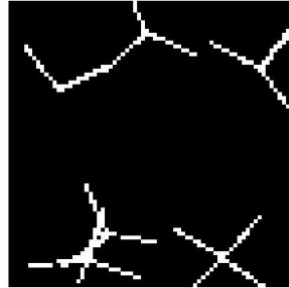


Figure 40 Features identified after STEP 1, with different numbers of largest integrals



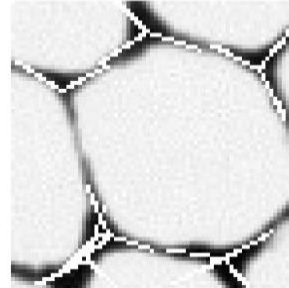
(a) The result of STEP 4  
(12 surfacelets)



(b) The result of STEP 6  
(9 surfacelets)

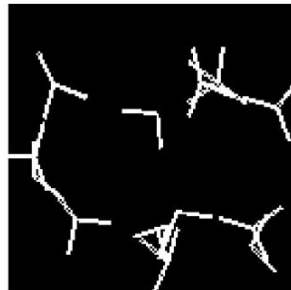


(c) The result of STEP 7

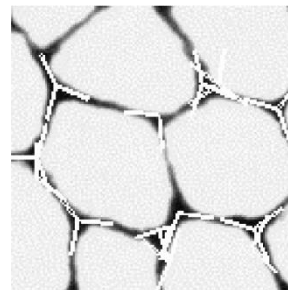


(d) The result matching the  
original image

Figure 41 The intermediate results during the process of the feature identification



(a) The feature  
identification result



(b) Result matching the  
original image

Figure 42 The identification result for the image with multiple grains

So far, the feature identification is only for the positions and orientations of boundaries. However, the thickness information cannot be captured. This can be realized by regarding the thickness as the extra dimension in the surfacelet space. Therefore, a better feature identification process can be proposed by tweaking the seventh step.

Instead of only rotating the averaged cubic surfacelets around the pivots, the thickness is also adjusted based on the principle of largest-integrals-based feature identification to match the boundaries. In the same example, the thickness is adjusted in the range of [0.01, 0.03] with step size of 0.005. The results for one-grain and multiple-grain images are shown in Figure 43 and Figure 44 respectively.

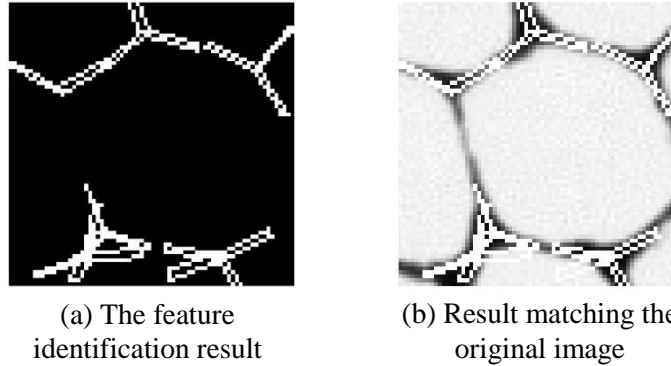


Figure 43 The identification result with thickness recognition for the image with one grain

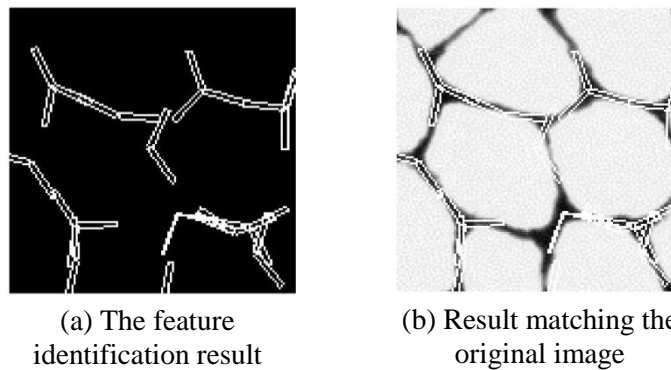


Figure 44 The identification result with thickness recognition for the image with multiple grains

It can be seen from Figure 43 and Figure 44 that not only the positions and orientations of boundaries, but also the variable thickness can be identified.

There are two major benefits of cubic and v-joint surfacelets over straight line or planes for feature identification. First, on one hand, straight lines or planes with finite

lengths are hard to be represented implicitly. On the other hand, although straight lines or planes can be represented implicitly with finite lengths, they are not able to identify straight boundary features with finite lengths efficiently and accurately. On contrary, cubic or v-joint surfacelets have finite lengths to better match straight boundary features. Second, cubic and v-joint surfacelets have non-zero thickness, which is very important in feature identification for the following reasons.

First, by the simple union operation, cubic and v-joint surfacelets can be combined into a single implicit surface so that a complex boundary geometry can be represented by a group of simple implicit surfaces, as shown in the examples in Section 4.4.1 and Section 4.4.2. However, this operation is hard to implement on straight lines or planes. Second, straight boundaries such as the Fe phase in the example of  $\text{Al}_2\text{O}_3$ -Fe composite in Section 4.4.2 usually have non-zero thickness. Therefore, v-joint surfacelets with non-zero thickness can capture the thickness information of such boundaries more efficiently and accurately.

The resulting composite surfacelets, cubic and v-joint for example, can be utilized for feature identification both globally and locally. Globally, composite surfacelets can be combined into a single implicit surface by the union operation so that a complex boundary geometry, such as the boundary network of  $\text{Al}_2\text{O}_3$ -Fe composite in Section 4.4.2, can be implicitly represented. In other words, the discrete pixels on material boundaries in images can be abstracted into a continuous geometric representation. This provides the global high level information of material images. One usage of this geometric representation is: combined with wavelets approximation, composite surfacelets are able to model material distributions. The detailed method will be



introduced in Chapter 5. Locally, the location, orientation and thickness information, such as that of individual edges and joints of the boundaries identified the v-joint surfacelets, can be obtained from corresponding surfacelets. For local features identified by a group of overlapping composites, the information can be easily obtained by clustering algorithms, such as K-means.

#### ***4.5 The Improvement of Surfacelet Location Evaluation based on the Consideration of Pixel Variation***

In Section 4.4, the feature identification method based on the largest surface integrals is introduced so that the boundary of the target features can be captured. However, this method is not successful when some inner portion of the target feature has similar greyscale value to outer environment. For example, Figure 45(a) shows the AFM image of the carbon fiber reinforced polymer composites (CFRPs) [110]. The bright part is the fiber and the rest is resin. For the purpose of better illustration, the contrast of the image is increased by Photoshop, as shown in Figure 45(b). It can be seen that the portion of the fiber in the dashed ellipse has the color very close to the environment. Therefore, the greyscale value will also be similar in the greyscale image. As a result, for example, the two cubic surfacelets shown in Figure 45(b) have the same surface integral. Thus, surfacelet 2 is also regarded as inside the fiber by the feature identification method discussed in the previous subsection. The identification result therefore has a huge error. Therefore, in order to accurately determine if the surfacelet is inside or outside the feature boundary, a new evaluation method should be introduced so that surfacelet 1 has larger evaluation value than surfacelet. Even when the colors are similar, human eyes can still easily identify the boundary because they are able to capture the boundary based on the

sharp gradient change of pixel values across the boundary. Therefore, based on this observation, the variation of the pixel values along the surfacelet should be considered.

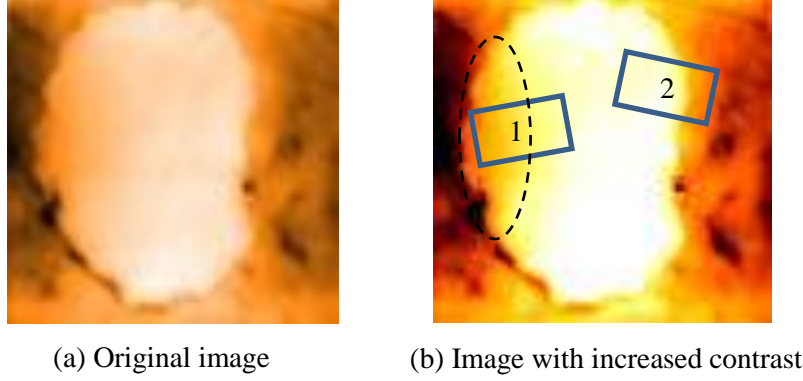


Figure 45 The original AFM image of carbon fiber reinforced polymer composites (CFRPs) and the one with increased contrast

In this dissertation, the variation of the pixel values is evaluated by the standard deviation. It can be estimated that a surfacelet with more evenly distributed pixel values or inside the feature boundary, such as surfacelet 1 in Figure 45(b), has a smaller standard deviation than those with less evenly distributed pixel values or outside the feature boundary, such as surfacelet 2. In order to make the evaluation of surfacelets inside the feature larger than that of those across the boundary, the surface integral and the standard deviation are proposed to be combined in the following ways of

$$t' = t + \frac{w}{\left( \sqrt{\frac{1}{N} \sum_{i=1}^N (v_i - \delta)^2} \right)^d},$$

$$t' = t - w \times \left( \sqrt{\frac{1}{N} \sum_{i=1}^N (v_i - \delta)^2} \right)^d$$

and

$$t' = \frac{t}{\left( \sqrt{\frac{1}{N} \sum_{i=1}^N (v_i - \delta)^2} \right)^d}$$

where  $v_i$  is the  $i^{\text{th}}$  pixel value,  $N$  is the number of pixels on the surfacelet,

$\delta = \frac{1}{N}(v_1 + \dots + v_N)$ ,  $w$  is the weight parameter and  $d$  is an integer power,  $t$  is original

evaluation of the surfacelet integral.  $t'$  is referred to as the improved surface integral.

It should be noted that  $t'$  is only used for the purpose of feature identification.

The inverse surfacelet transform is still based on  $t$ .

In the following subsection, the feature identification results of these three formulas are compared, and the formula with the best result is determined. The example of CFRPs in Figure 45 is used for the comparison of the three formulas.

In order to quantitatively compare the feature identification results of these three formulas, the real boundary feature is needed as the comparison datum. Many existing boundary recognition methods are available to obtain the real boundary feature. The results of Sobel, Prewitt, Roberts, Log and Canny methods are shown in Figure 46 (a), (b), (c), (d) and (e) respectively. It can be seen that the best result is from the Canny method, since most part of the boundary is recognized. However, it is still not the real boundary feature. Therefore, manual modification is conducted based on the Canny method. The result is shown in Figure 46 (f), and the result matching the boundary in the original image is shown in Figure 46 (g).

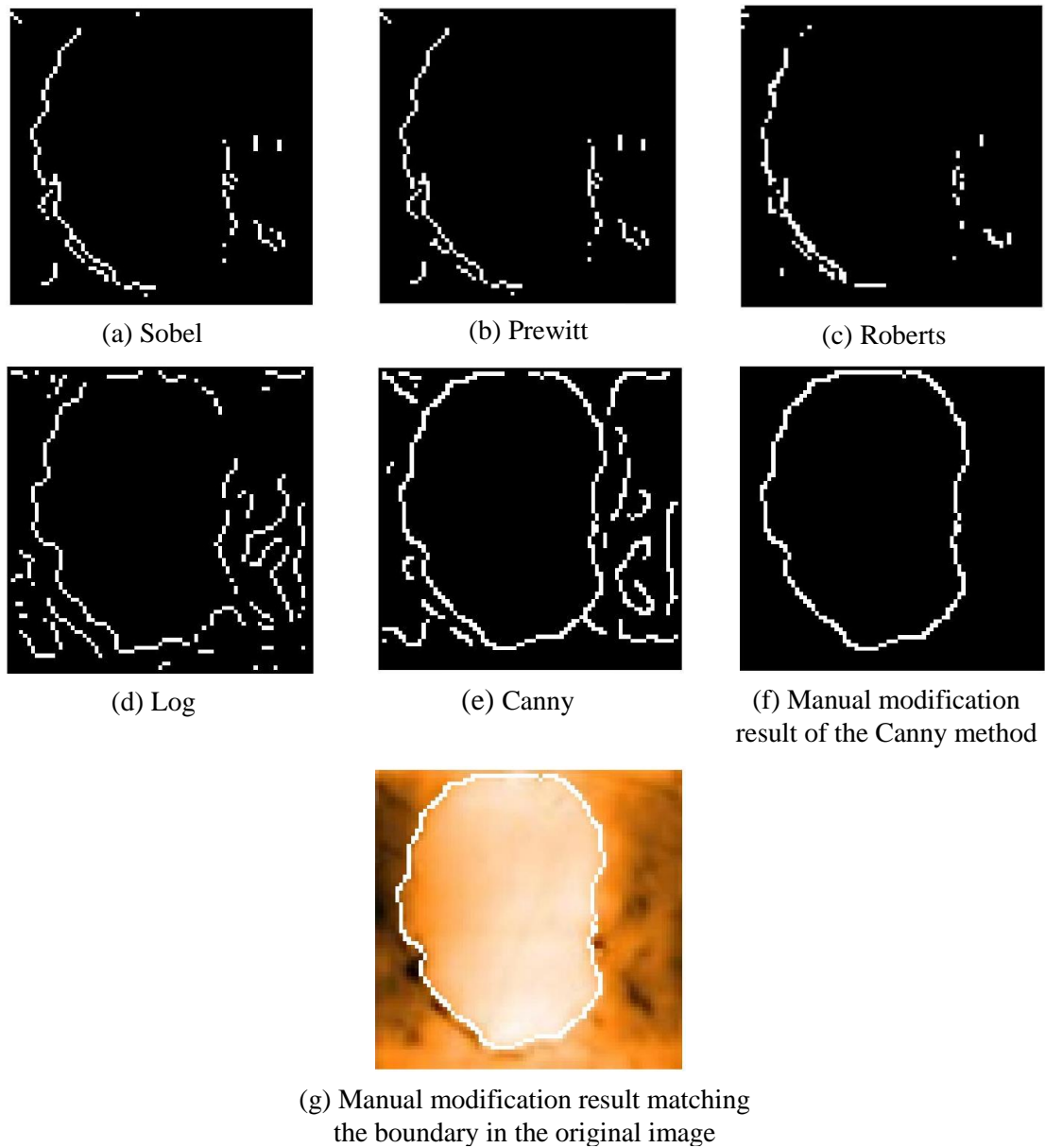


Figure 46 The results of different boundary recognition methods

The following measure properties of image regions are used to compare the feature identification results:

'Number of pixels' — the actual number of pixels in the region;

'Centroid' — the center of mass of the region. The first element of Centroid is the horizontal coordinate (or x-coordinate) of the center of mass, and the second element is the vertical coordinate (or y-coordinate);

'Orientation' — the angle (in degrees ranging from -90 to 90 degrees) between the x-axis and the major axis of the ellipse that has the same second-moments as the region;

'Eccentricity' — the eccentricity of the ellipse that has the same second-moments as the region. The eccentricity is the ratio of the distance between the foci of the ellipse and its major axis length. The value is between 0 and 1.

Because some of the feature identification results are not close loops in the images, and some have two or more regions, it is necessary that the datum boundary for comparison is divided into two portions (left and right), and the comparison is conducted on both portions. As shown in Figure 47(a), the boundary is divided by the vertical line that has average x-coordinate of the four extrema points of the entire boundary. The two centroids and the two ellipses with the same second-moments are shown in Figure 47(b). The corresponding measure properties are listed in Table 3.

Table 3 Measure properties of the datum boundary

	Number of pixels	Centroid	Orientation	Eccentricity
Left portion	117	(16.5, 35.4)	-87.1	0.9463
Right portion	112	(51.1, 36.0)	-89.9	0.9653

In the following subsections, for each formula and parameter configuration, the property measurement is conducted on the visually best results.

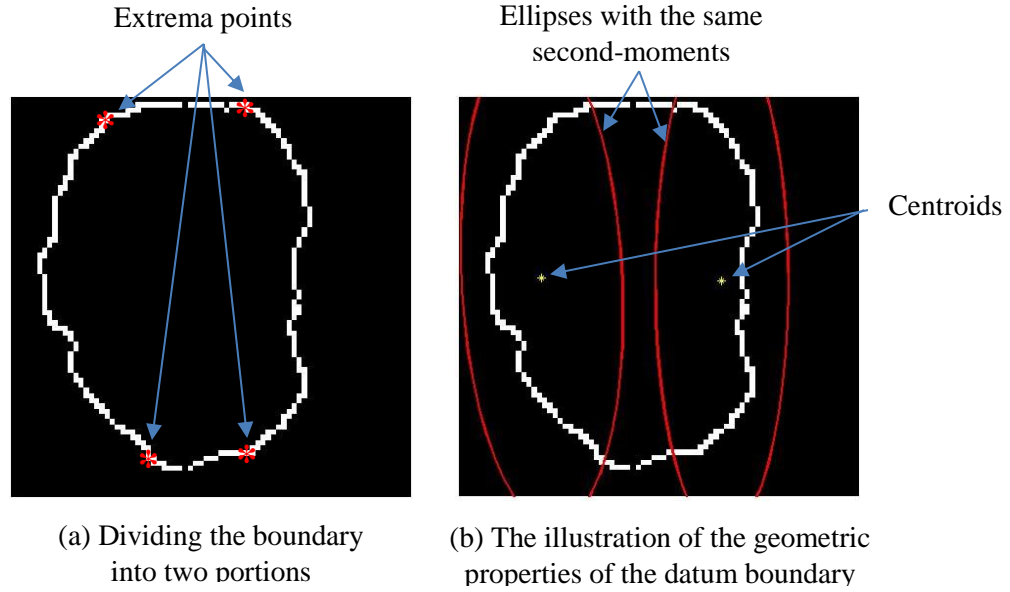


Figure 47 The calculation of the geometric properties of the datum boundary for comparison

#### 4.5.1 The implementation with the original AFM image

The shape parameters of the cubic surfacelet are  $l_1=0.6$ ,  $l_2=0.4$ , and  $l_3=3$ . The translation along the z-axis is set as zero. The number of cubic surfacelets used is  $m \times n \times \alpha \times \beta \times \gamma = 20 \times 20 \times 1 \times 1 \times 30 = 12000$ . The original image with low contrast is used.

When  $d=1$ , the new evaluation of the improved surfacelet integral  $t'$  can be obtained as

$$t' = t + \frac{w}{\sqrt{\frac{1}{N} \sum_{i=1}^N (v_i - \delta)^2}}$$

When  $w=10$ , the feature identification results are shown in Figure 48. The measure properties for Figure 48(f) are listed in Table 4.



(a) The largest 200 integrals (b) The largest 300 integrals (c) The largest 600 integrals



(d) The largest 800 integrals (e) The largest 1000 integrals (f) The largest 1200 integrals

Figure 48 Feature identification results when  $w = 10$

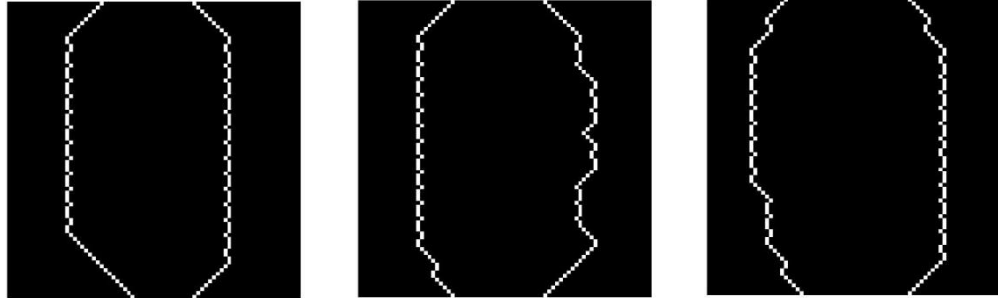
Table 4 Measure properties for Figure 48(f)

	Number of pixels	Centroid	Orientation	Eccentricity
Left portion	77	(15.0, 39)	-86.6	0.9912
Right portion	77	(60.4, 39)	-89.2	0.9938

When  $w = 10^3$ , the feature identification results are shown in Figure 49. The measure properties for Figure 49(f) are listed in Table 5.



(a) The largest 200 integrals (b) The largest 300 integrals (c) The largest 600 integrals



(d) The largest 800 integrals (e) The largest 1000 integrals (f) The largest 1200 integrals

Figure 49 Feature identification results when  $w = 10^3$

Table 5 Measure properties for Figure 49(f)

	Number of pixels	Centroid	Orientation	Eccentricity
Left portion	77	(15.2, 39)	-85.8	0.9907
Right portion	77	(60.46, 39)	-89.2	0.9938

When  $w = 10^5$ , the feature identification results are shown in Figure 50. The measure

properties for Figure 50(f) and (g) are listed in

Table 6 and Table 7 respectively.





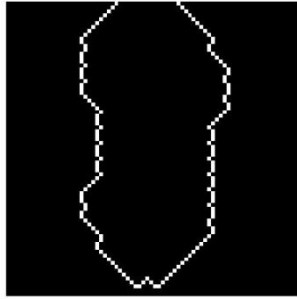
(a) The largest 200 integrals



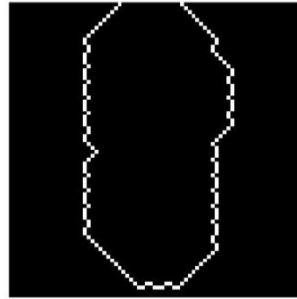
(b) The largest 300 integrals



(c) The largest 400 integrals



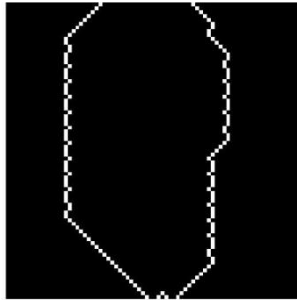
(d) The largest 600 integrals



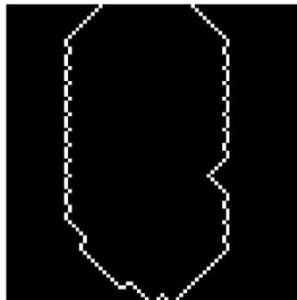
(e) The largest 800 integrals



(f) The largest 1000 integrals



(g) The largest 1200 integrals



(h) The largest 1400 integrals



(f) The largest 1600 integrals



(g) The largest 1800 integrals

Figure 50 Feature identification results when  $w = 10^5$

Table 6 Measure properties for Figure 50(f)

	Number of pixels	Centroid	Orientation	Eccentricity
Left portion	77	(16.9, 39)	-83.4	0.9897
Right portion	77	(56.9, 39)	-88.4	0.9966

Table 7 Measure properties for Figure 50(g)

	Number of pixels	Centroid	Orientation	Eccentricity
Left portion	77	(15.5, 39)	-85.2	0.9903
Right portion	77	(57.7, 39)	-87.4	0.9940

When  $w = 10^{10}$ , the feature identification results are shown in Figure 51.

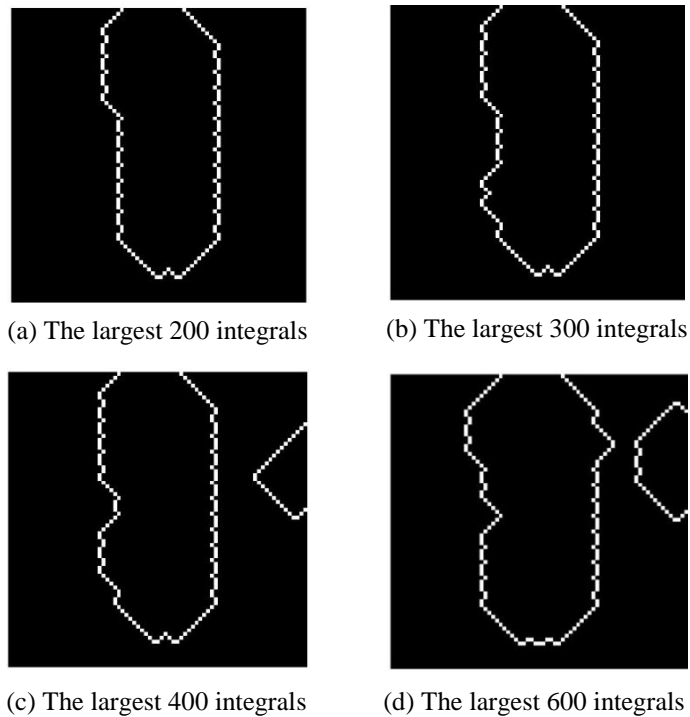


Figure 51 Feature identification results when  $w = 10^{10}$

When  $w = 10^{15}$ , the feature identification results are shown in Figure 52.

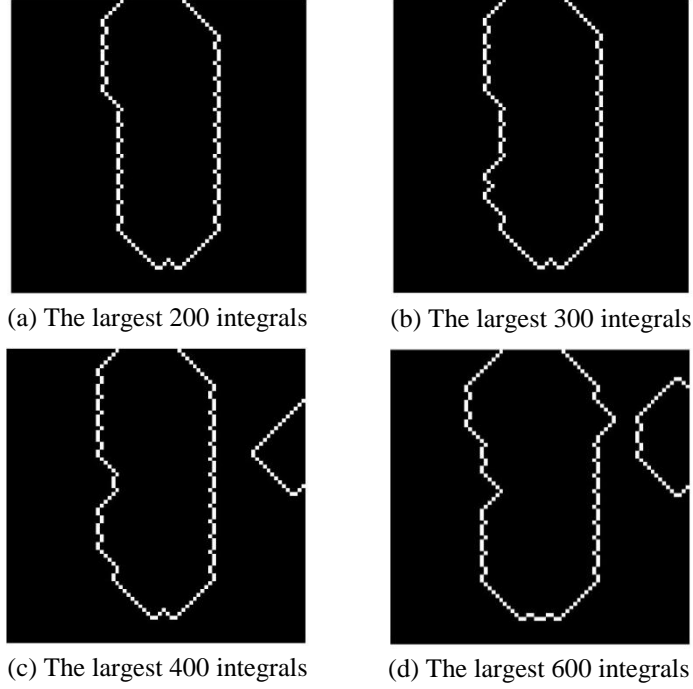


Figure 52 Feature identification results when  $w = 10^{15}$

When  $d=4$ , the new evaluation of the improved surfacelet integral  $t'$  can be obtained as

$$t' = t + \frac{w}{\left(\sqrt{\frac{1}{N} \sum_{i=1}^N (v_i - \delta)^2}\right)^4} = t + \frac{w}{\left(\frac{1}{N} \sum_{i=1}^N (v_i - \delta)^2\right)^2}$$

When  $w=10$ , the feature identification results are shown in Figure 53. The measure properties for Figure 53(e) and (f) are listed in Table 8 and Table 9 respectively.

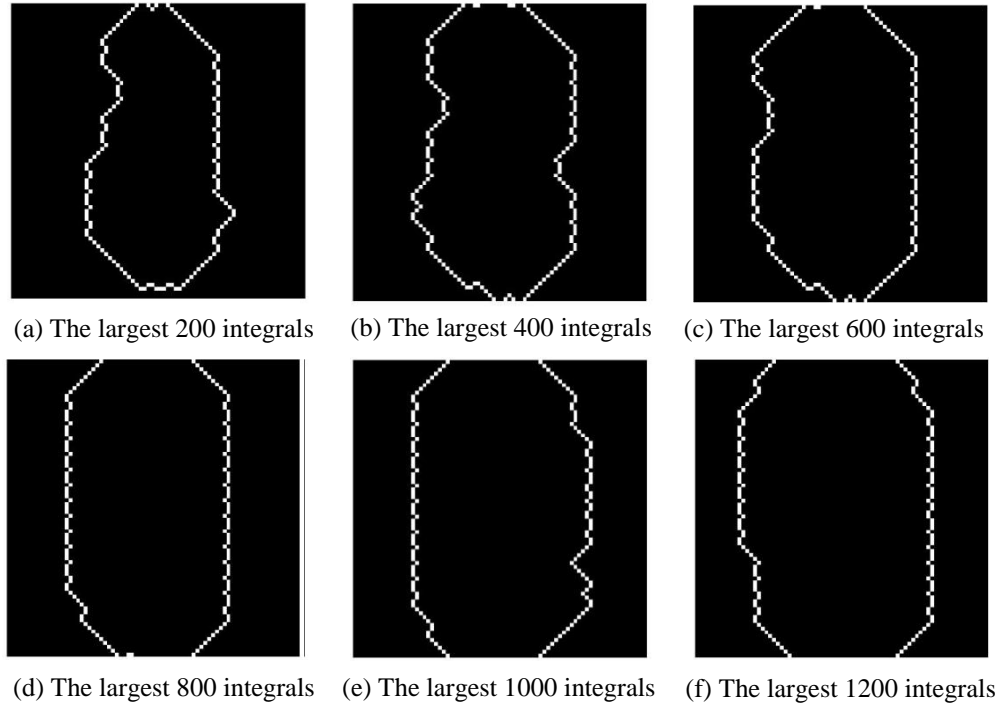


Figure 53 Feature identification results when  $w = 10$

Table 8 Measure properties for Figure 53(e)

	Number of pixels	Centroid	Orientation	Eccentricity
Left portion	77	(17.6, 39)	-89.2	0.9938
Right portion	77	(58.7, 39)	-89.4	0.9862

Table 9 Measure properties for Figure 53(f)

	Number of pixels	Centroid	Orientation	Eccentricity
Left portion	77	(15.0, 39)	-86.6	0.9912
Right portion	77	(60.4, 39)	-89.2	0.9938

When  $w = 10^3$ , the feature identification results are shown in Figure 54. The measure properties for Figure 54(e) and (f) are listed in Table 10 and Table 11 respectively.

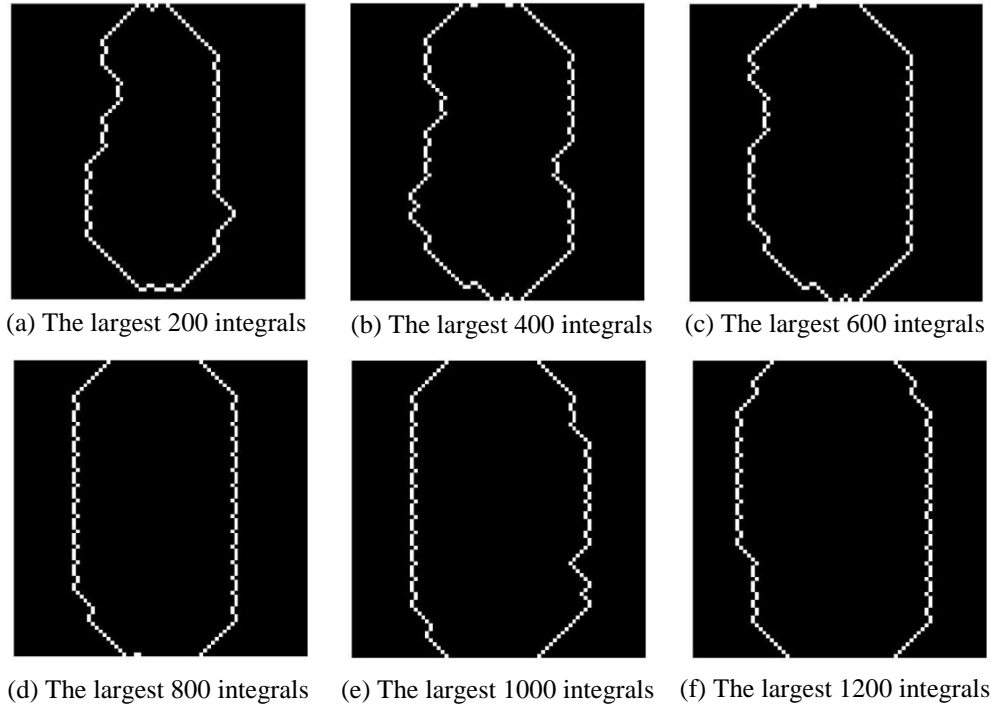


Figure 54 Feature identification results when  $w = 10^3$

Table 10 Measure properties for Figure 54(e)

	Number of pixels	Centroid	Orientation	Eccentricity
Left portion	77	(17.6, 39)	-89.2	0.9938
Right portion	77	(58.7, 39)	-89.4	0.9862

Table 11 Measure properties for Figure 54(f)

	Number of pixels	Centroid	Orientation	Eccentricity
Left portion	77	(15, 39)	-86.6	0.9912
Right portion	77	(60.4, 39)	-89.2	0.9938

When  $w = 10^5$ , the feature identification results are shown in Figure 55.

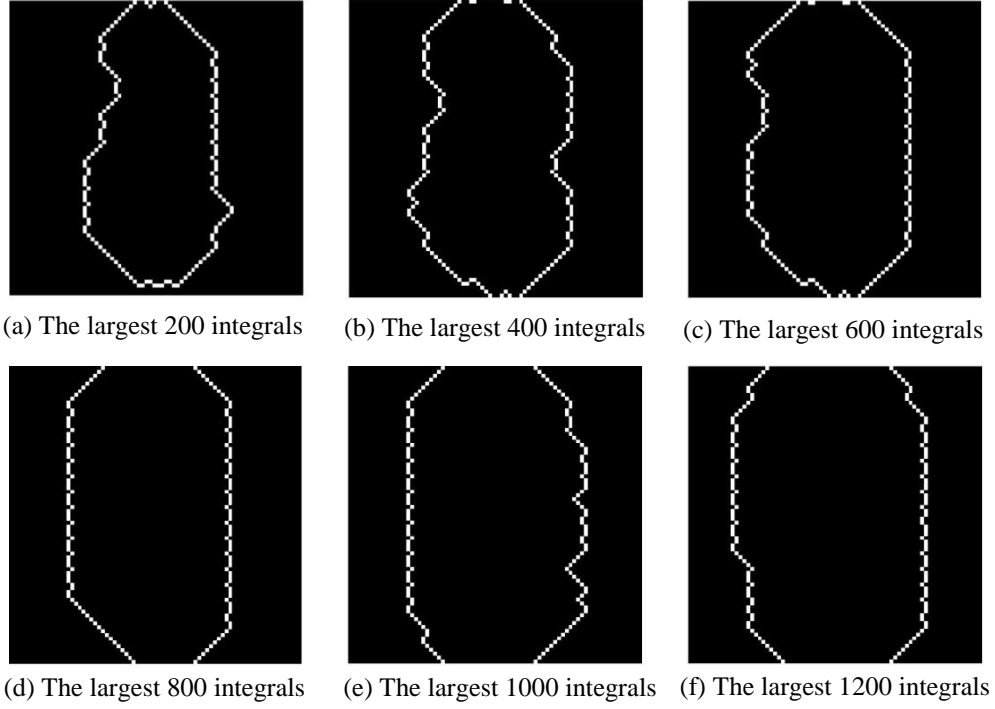


Figure 55 Feature identification results when  $w = 10^5$

For  $t' = t - w \times \left( \sqrt{\frac{1}{N} \sum_{i=1}^N (v_i - \delta)^2} \right)^d$ , when  $d=1$ , the new evaluation of the improved

surfacelet integral  $t'$  can be obtained as

$$t' = t - w \times \sqrt{\frac{1}{N} \sum_{i=1}^N (v_i - \delta)^2}$$

When  $w = 10$ , the feature identification results are shown in Figure 56.

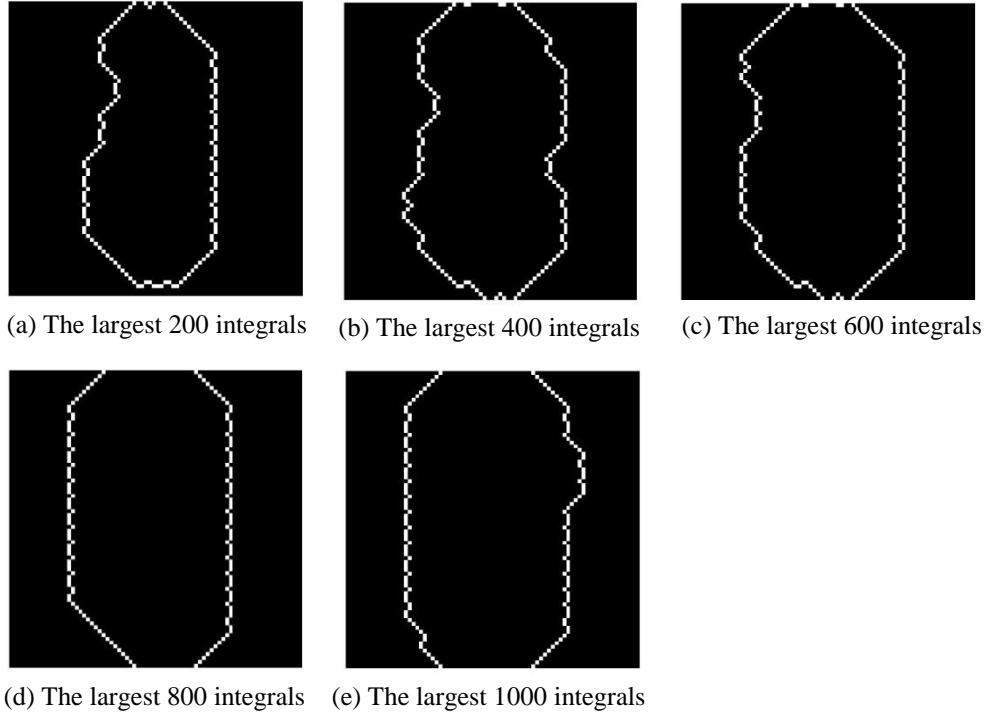


Figure 56 Feature identification results when  $w = 10$

When  $w = 10^3$ , the feature identification results are shown in Figure 57. The measure properties for Figure 57(e) and (f) are listed in Table 12 and

Table 13 respectively.

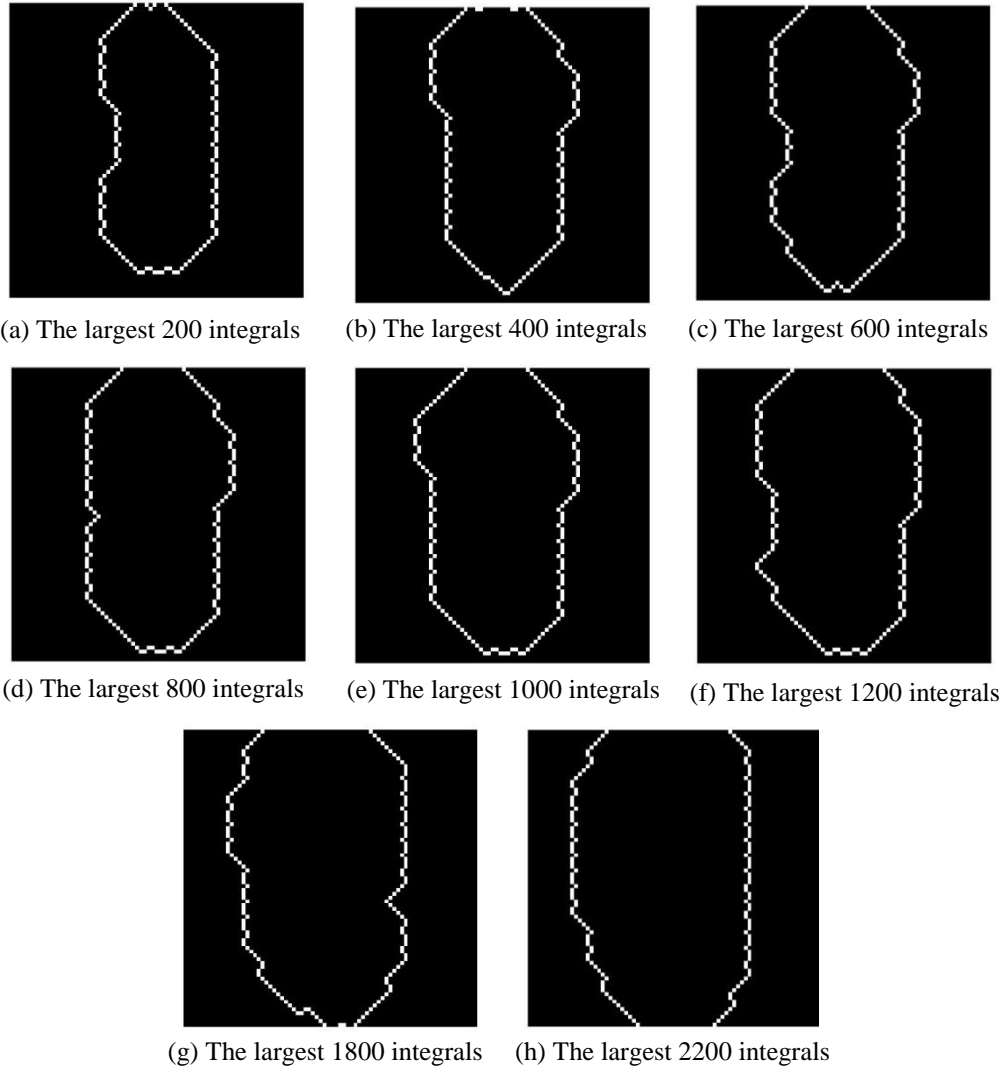


Figure 57 Feature identification results when  $w = 10^3$

Table 12 Measure properties for Figure 57(g)

	Number of pixels	Centroid	Orientation	Eccentricity
Left portion	81	(18.5, 40.7)	-78.8	0.9819
Right portion	77	(55.5, 39)	-86.8	0.9908



Table 13 Measure properties for Figure 57(h)

	Number of pixels	Centroid	Orientation	Eccentricity
Left portion	77	(15.8, 39)	-83.7	0.9867
Right portion	77	(56.7, 39)	-87.7	0.9965

When  $w = 10^5$ , the feature identification results cannot be obtained.

When  $d=4$ , the new evaluation of the improved surfacelet integral  $t'$  can be obtained as

$$t' = t - w \times \left( \sqrt{\frac{1}{N} \sum_{i=1}^N (v_i - \delta)^2} \right)^4 = t - w \times \left( \frac{1}{N} \sum_{i=1}^N (v_i - \delta)^2 \right)^2$$

When  $w = 10$ , the feature identification results are shown in Figure 58.

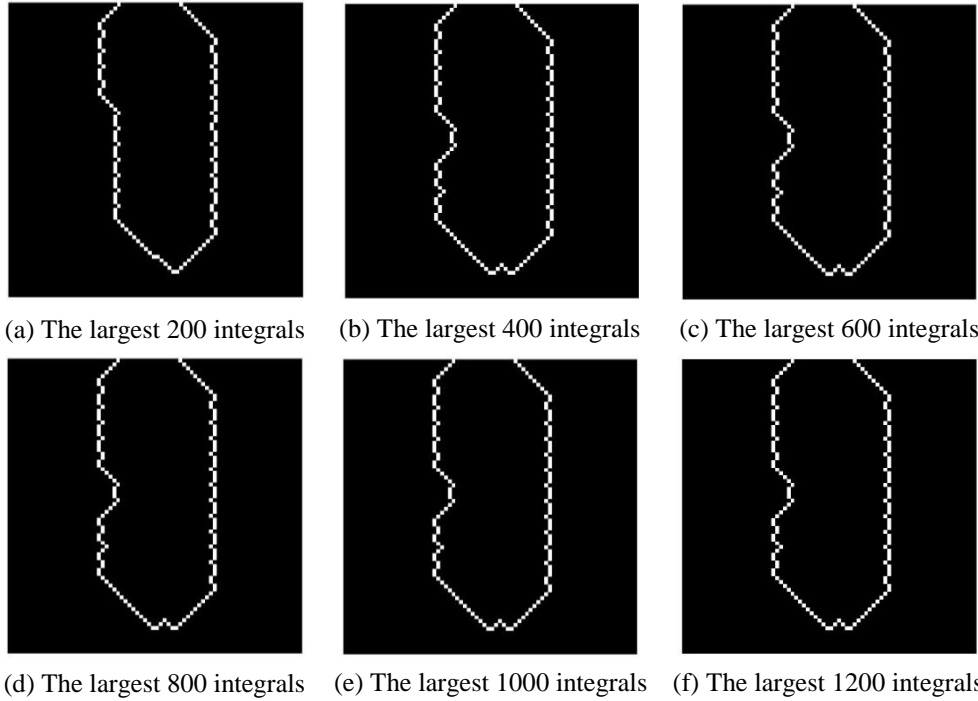


Figure 58 Feature identification results when  $w = 10$

For  $t' = \frac{t}{\left(\sqrt{\frac{1}{N} \sum_{i=1}^N (v_i - \delta)^2}\right)^d}$ , when  $d=1$ , the feature identification results are

shown in Figure 59. The measure properties for Figure 59 (e) are listed in Table 14.

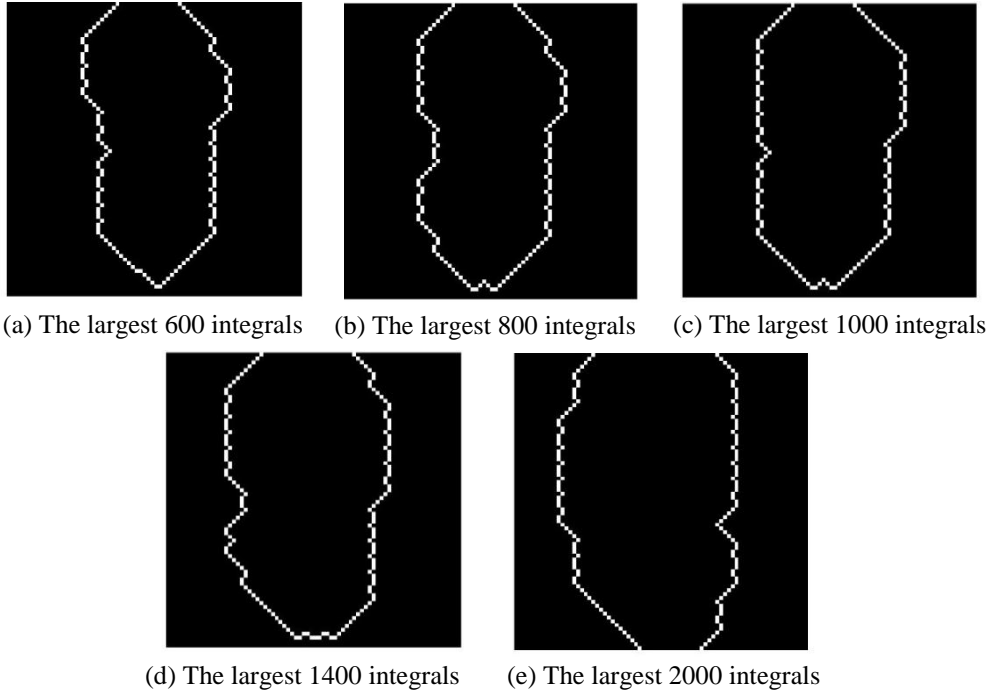
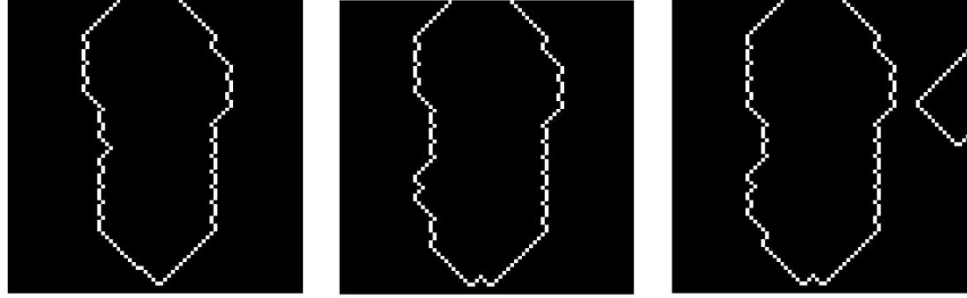


Figure 59 Feature identification results when  $d=1$

Table 14 Measure properties for Figure 59(e)

	Number of pixels	Centroid	Orientation	Eccentricity
Left portion	77	(16.8, 39)	-81.7	0.9814
Right portion	77	(56.3, 39)	-86.9	0.9966

When  $d=4$ , the feature identification results are shown in Figure 60.



(a) The largest 600 integrals (b) The largest 800 integrals (c) The largest 850 integrals

Figure 60 Feature identification results when  $d=4$

When  $d=6$ , the feature identification results are shown in Figure 61.



(a) The largest 600 integrals (b) The largest 800 integrals (c) The largest 850 integrals

Figure 61 Feature identification results when  $d=6$

#### 4.5.2 The implementation with the contrast-increased AFM image

The shape parameters of the cubic surfacelet and the number of cubic surfacelets used remain the same as in Section 4.5.1. The contrast-increased AFM image in Figure (b) is used.

When  $t' = t + \frac{w}{\sqrt{\frac{1}{N} \sum_{i=1}^N (v_i - \delta)^2}}$ , and  $w=10$ , the feature identification results are

shown in Figure 62.

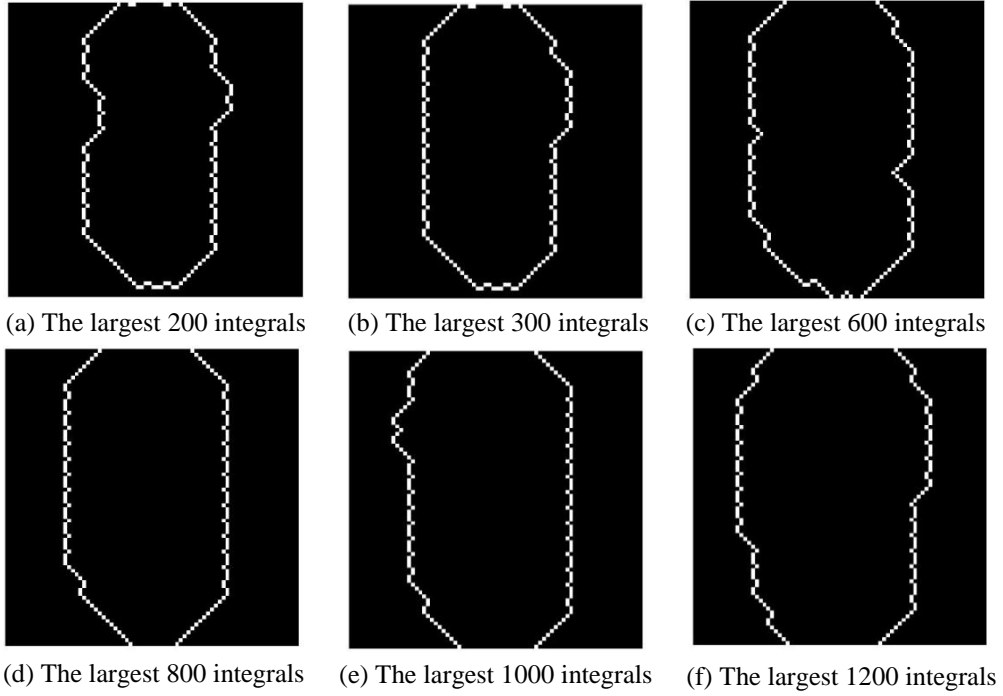


Figure 62 Feature identification results when  $w = 10$

When  $t' = \frac{t}{\sqrt{\frac{1}{N} \sum_{i=1}^N (v_i - \delta)^2}}$ , the feature identification results are shown in Figure

63.

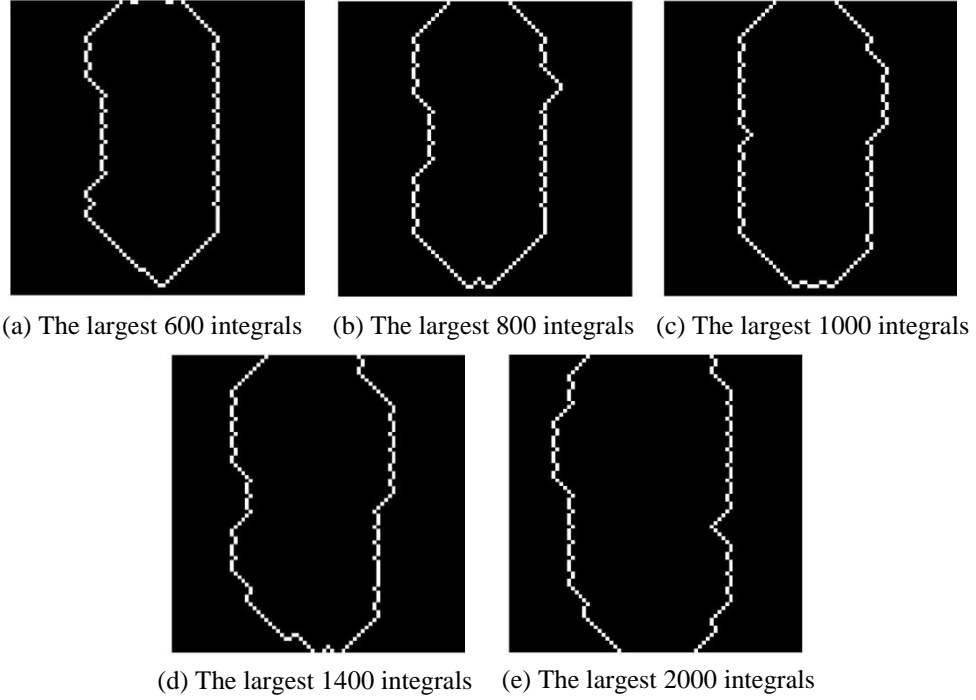


Figure 63 Feature identification results when  $d=1$

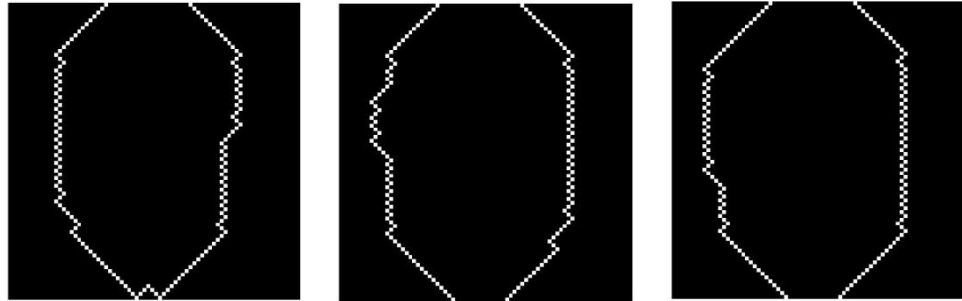
#### 4.5.3 The implementation with the contrast-increased AFM image and different surfacelet shape parameters

The shape parameters of the cubic surfacelet are  $l_1=0.84$ ,  $l_2=0.64$ , and  $l_3=3$ . The translation along the  $z$ -axis and the number of cubic surfacelets remain the same. The contrast-increased AFM image is used.

When  $d=1$ , the new evaluation of the improved surfacelet integral  $t'$  can be obtained as

$$t' = t + \frac{w}{\sqrt{\frac{1}{N} \sum_{i=1}^N (v_i - \delta)^2}}$$

When  $w=10$ , the feature identification results are shown in Figure 64. The measure properties for Figure 64(a) and (c) are listed in Table 15 and Table 16 respectively.



(a) The largest 200 integrals (b) The largest 300 integrals (c) The largest 400 integrals

Figure 64 Feature identification results when  $w = 10$

Table 15 Measure properties for Figure 64(a)

	Number of pixels	Centroid	Orientation	Eccentricity
Left portion	79	(18.2, 39.9)	-81.7	0.9715
Right portion	79	(54.8, 39.9)	81.3	0.9789

Table 16 Measure properties for Figure 64(c)

	Number of pixels	Centroid	Orientation	Eccentricity
Left portion	79	(18.1, 39.9)	-79.5	0.9822
Right portion	79	(54.9, 39.9)	80.7	0.9837

When  $w = 10^3$ , the feature identification results are shown in Figure 65.

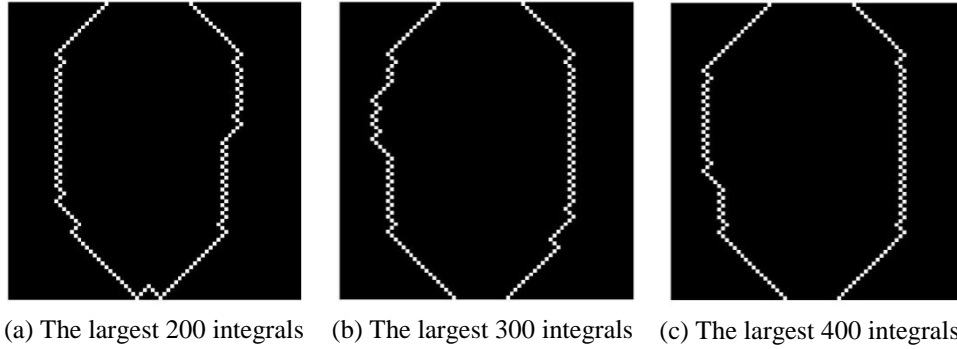


Figure 65 Feature identification results when  $w = 10^3$

When  $w = 10^{10}$ , the feature identification results are shown in Figure 66.

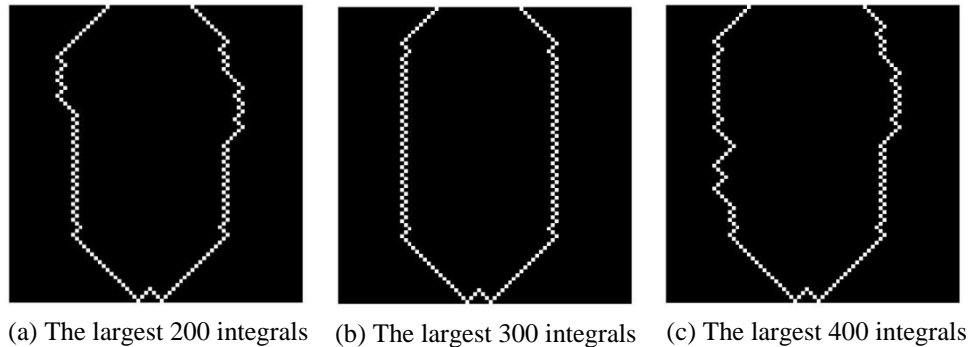


Figure 66 Feature identification results when  $w = 10^{10}$

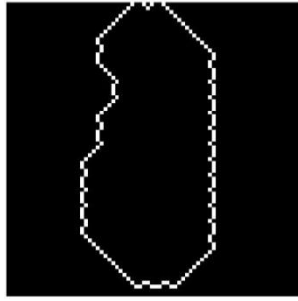
#### 4.5.4 Conclusion of comparison results of the three formulas

Based on the comparison result, it can be concluded that increasing the image contrast does not improve the quality of the feature identification. The possible reason is that increasing the image contrast enlarges the differences between all pixels values. When the boundary of features has sharper change of pixel values, the variance of other regions are also increasing. As a result, the boundary of features can still not stand out from the rest of pixels. Therefore, for feature identification with or without considering the standard deviation, the original and contrast-increased images show no difference.

From the comparison of the three formulas in Sections 4.5.2 and 4.5.3, it can be seen that the result that best matches the boundary is as follows.

$$\text{When } t' = t - w \times \sqrt{\frac{1}{N} \sum_{i=1}^N (v_i - \delta)^2}, \text{ and } w = 10^3, \text{ that is } t' = t - 10^3 \times \sqrt{\frac{1}{N} \sum_{i=1}^N (v_i - \delta)^2},$$

with the largest 1800 surface integrals, the result is shown in Figure 67(b). This is regarded as the best, because the number of pixels and positions of the centroids are the closest to the real values. Meanwhile, the orientation and eccentricity are also very close to the real values. It can be seen that the proposed method with considering the gradient information of pixels can improve the feature identification result.



(a) The feature identification result without gradient information



(a) The best feature identification result with gradient information

Figure 67 The best feature identification result, when  $t' = t - 10^3 \times \sqrt{\frac{1}{N} \sum_{i=1}^N (v_i - \delta)^2}$  with the largest 1800 integrals compared to result without considering the gradient information

Although the  $t' = t - 10^3 \times \sqrt{\frac{1}{N} \sum_{i=1}^N (v_i - \delta)^2}$  produces the best result in this example,

other methods proposed in Section 4.5 could have better results in other examples. More research is needed in order to systematically utilize the proposed methods. However, this research will not be covered in this dissertation, because the aim of this subsection is mainly to propose possible approaches for the improvement of surfacelet location



evaluation. In addition, the best result for a particular example is given, because this result will be used in Chapter 5 for the material distribution modeling

#### ***4.6 Conclusion and Future Work***

In this chapter, a new concept of composite surfacelets is proposed to represent and identify complex microstructures. Composite surfacelets can be constructed from existing primitive or composite surfacelets. As two examples, cubic and v-joint surfacelets are developed to identify line-edged features. They are tested with real microstructure images. The results show that with the surfacelet transform and the largest-integrals-based feature identification method, these two composite surfacelets are able to identify the locations and orientations of features. It should be noted that the concept of composite surfacelets is general. Composite surfacelets are not limited to these two demonstrated in this chapter. More types of composite surfacelets can be designed for different microstructural features.

In order to improve the feature identification results for material images without clear feature boundaries, a method of improving the surfacelet location evaluation based on the consideration of pixel variation is proposed. An example is given, and different new improved evaluations are compared. The results show that with all improved evaluations, the feature boundary can be better identified. However, there exists one method which gives the best result depending on the example.

The identification approach presented in this chapter is mainly for important features. If other details about material microstructures in images are of interest and the reconstruction of the original images is desired, the inverse surfacelet transform can be

applied. More surfacelets are required if more details need to be captured and reconstructed.

Compared to the traditional edge detection methods, the proposed method extracts the important geometric features (shapes, sizes, locations, and orientations), which provide parametric-level information to determine material properties. That is, the proposed method uses only a few parameters to represent important features instead of pixels. For the purpose of reducing computational time, only three stacked identical images are used in the examples. The features identified in the examples are just 2.5-D. In the future work, the proposed approach will be tested on truly 3D examples.

## CHAPTER 5

### APPLICATION OF SURFACELETS IN MATERIALS MODELING

It has been demonstrated in Chapter 3 and Chapter 4 that, with the primitive or composite surfacelets, the microstructural features of material images can be identified. As such, the microstructural information of 3D material images can be extracted and converted into implicit surface models. Based on these representations, material composition or local property distributions can be further modeled with extra information from the material images, since the material microstructure defines the ‘skeleton’ or major material distributions, whereas the material composition is more like the ‘flesh and skin’ in addition to the microstructural information.

The goal of this chapter is to find a method for modeling the continuous distributions of materials, such as material compositions or local properties, based on the identified boundaries of microstructures. The assumption is that the material composition or local property distributions are similar in all directions, i.e. nearly isotropic. Therefore, the 2D distributions can be simplified as 1D ones. For example, as shown in Figure 68, in all directions inside the material domain, as indicated by the straight lines crossing the center of the object, the 1D distributions of material are very similar along the lines. In other words, if the distributions along the lines are normalized to ones with a single radius and the distributions are mapped to a new domain with the boundary represented as a circle, the distributions then have rotational symmetry. As a result, the 2D distributions can be approximated by 1D distributions along the radial lines.

In this chapter, a systematic surfacelet selection and modeling mechanism to support material distribution modeling with surfacelets is developed. From the images of

material properties or compositions, wavelet analysis is applied to identify the number and type of wavelets to describe the 1D distribution along the radial lines. Then surfacelets are constructed based on the identified wavelets and the 2D distributions can be modeled by the surfacelets.

In the rest of the chapter, the general procedure of the surfacelet selection and modeling is described in Section 5.1. The wavelet transform is introduced in Section 5.2. An example is implemented and demonstrated in Section 5.3. The analysis of the results is given in Section 5.4. In Section 5.5, the contribution and limitation of the proposed method and the future work of this chapter are discussed.

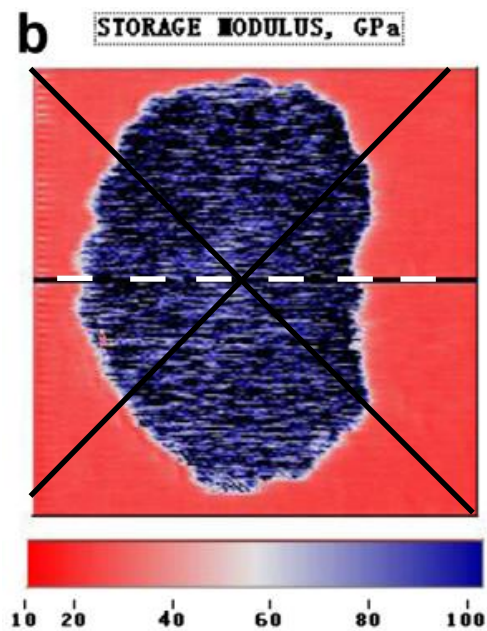


Figure 68 The isotropic distribution of property along the radius directions of the material

## ***5.1 The General Procedure of Approximating Material Composition or Local Property Distributions with Surfacelets***

The general procedure is shown in the flow chart in Figure 69 and described as follows.

In STEP 1, appropriate surfacelet shape parameters are chosen to match the microstructural features of interest.

In STEP 2, surfacelet transform is performed so that all microstructural features of interest are identified. Together with STEP 1, this part is for *feature identification*.

In STEP 3, 1D material composition or local property distribution around the microstructures of interest is obtained by the distribution of image pixel value or experimental data.

In STEP 4, 1D wavelet transform is conducted to approximate the material composition or local property distributions obtained from STEP 3. This 1D wavelet transform is only for 1D material composition or local property distributions in a representative direction. Together with STEP 3, this part is for *wavelet transform*.

In the final STEP 5, the obtained wavelets and the implicit surfaces from feature identification are combined into surfacelets. This is conducted by plugging the implicit surfaces into the obtained wavelets, simply by the definition of a general surfacelet basis function described in [4]. The resulting surfacelets construct the model of the 3D material images.

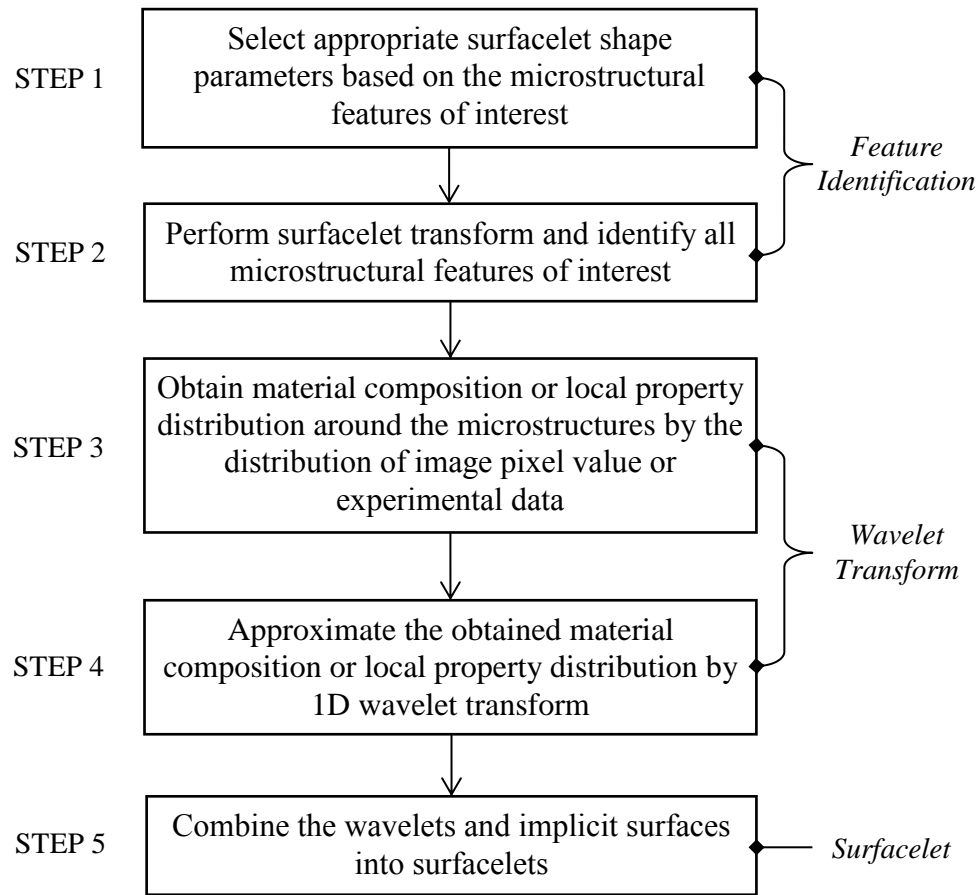


Figure 69 The general procedure of approximating material composition or local property distributions with surfacelets

## 5.2 The Wavelet Transform

In the domain of 2D shape representations, wavelets are among the most popular multi-resolution representations. Similar to Fourier analysis, wavelet analysis is to represent and approximate signals (or functions in general) with orthogonal or non-orthogonal basis functions. Both methods can be used to uncover frequency components of signals. Both can be used to represent multi-resolution subspaces and fast algorithms are available for both. However, instead of sinusoidal functions in Fourier analysis, the functional space for wavelet analysis is decomposed based on a scaling function  $\phi(t)$  and a wavelet function  $\psi(t)$  with one dimensional variable  $t$  for multi-resolution analysis.

In the continuous wavelet transform (CWT) basis functions are called wavelets  $\varphi(t)$ . The CWT compares the signal to the shifted and compressed or stretched (scaled) versions of these allowed wavelets. If the signal is a real value, the CWT is a real-valued function of scale and position. For a scale parameter ( $a>0$ ) and position ( $b$ ) the CWT is:

$$c(a,b) = \int_{-\infty}^{\infty} f(t) \frac{1}{\sqrt{a}} \varphi\left(\frac{t-b}{a}\right) dt$$

There are many different admissible wavelets that can be used in the CWT, which is actually the strength of wavelet analysis, although certain forms such as Haar, Daubechies, Morlet, etc. have been used more extensively.

Using MATLAB wavelet tool box and using the Mexican hat as the wavelet function the wavelet transformation is conducted. The mirrored signal is saved in .mat format and inserted to the toolbox. The value of  $\sigma$  for the Mexican hat function has been selected as 0.5 which is the default value. The number and the range of the scales are optional and are inserted as inputs to the wavelet toolbox.

### ***5.3 An Example and Results***

In this subsection, an example of modeling material local property distribution is demonstrated. The example image is chosen the same as Figure 45(a). All experimental images in this chapter are from the work of Gu et al. [110]

In STEP 1, the surfacelet shape parameters are chosen identical to those used in Section 4.5.1.

In STEP 2, surfacelet transform is performed to identify the microstructural feature. In this Chapter, the best feature identification result shown in Figure 67 is used.

In STEP 3, material local property distribution around the microstructure is obtained by experimental data. In this chapter, the storage modulus is used as an example for material local property. From experimental results, the 2D storage modulus map is shown in Figure 68. The discrete storage modulus data points along the dashed straight line indicated in Figure 68 are shown in Figure 70.

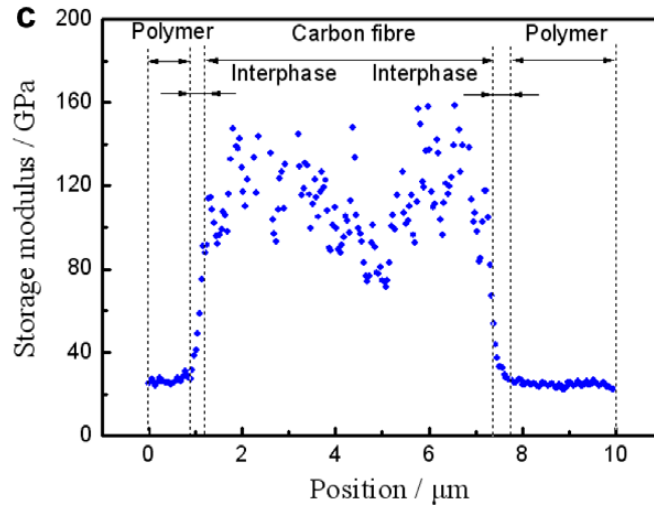


Figure 70 The discrete storage modulus data along the straight line indicated in Figure 68

In STEP 4, 1D wavelet transform is conducted to approximate the material local property distributions obtained from the data points in Figure 70. The approximated and the original results are shown in Figure 71. The blue curve is the cubic spline fitting of the original data (100 data points), and the red one is the wavelet approximation result. This 1D wavelet transform is conducted in MATLAB wavelet toolbox. 50 evenly distributed sample data points are chosen from Figure 70 so that the computational cost can be lowered, but they are enough to represent the entire distribution.



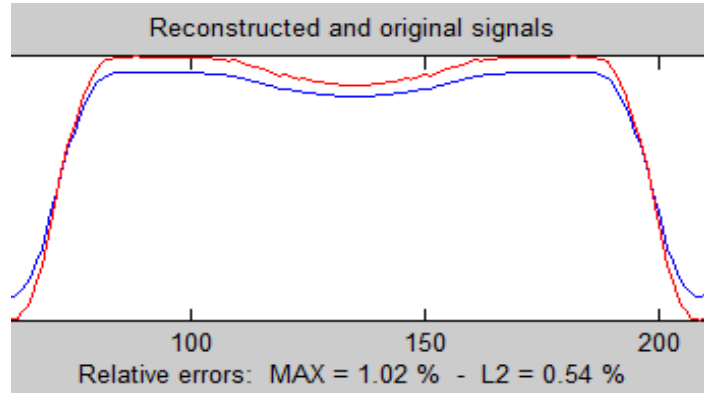


Figure 71 The wavelet transformation results for the discrete storage modulus data shown in Figure 70

In STEP 5, the obtained wavelets and the implicit surfaces from feature identification are combined into surfacelets.

Based on the feature identification and wavelet transformation results, the storage modulus distribution can be approximated. Because the result surfacelet model is in 3D, only the 2D distribution in the middle plane of the model is shown and compared. The results for Mexican hat with 25 data points, Mexican hat with 50 data points, Beta wavelet with 25 data points, and Beta wavelet with 50 data points are shown in Figure 72, Figure 73, Figure 74, and Figure 75 respectively.

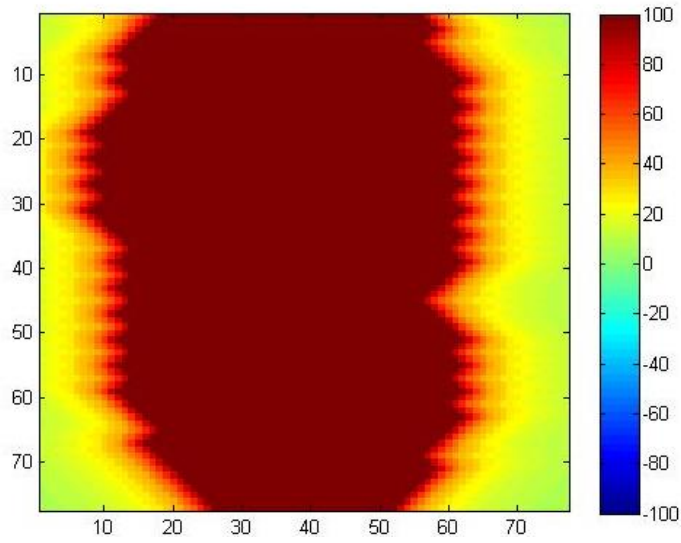


Figure 72 The 2D distribution in the middle plane of the surfacelet model from Mexican hat wavelet with 25 data points

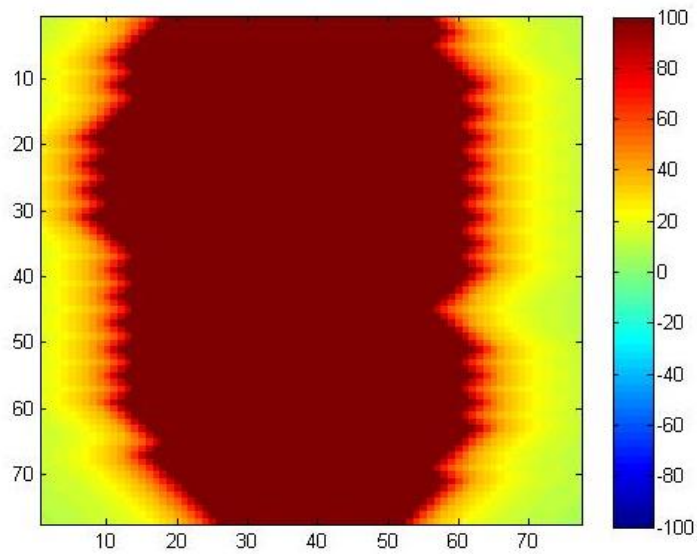


Figure 73 The 2D distribution in the middle plane of the surfacelet model from Mexican hat wavelet with 50 data points

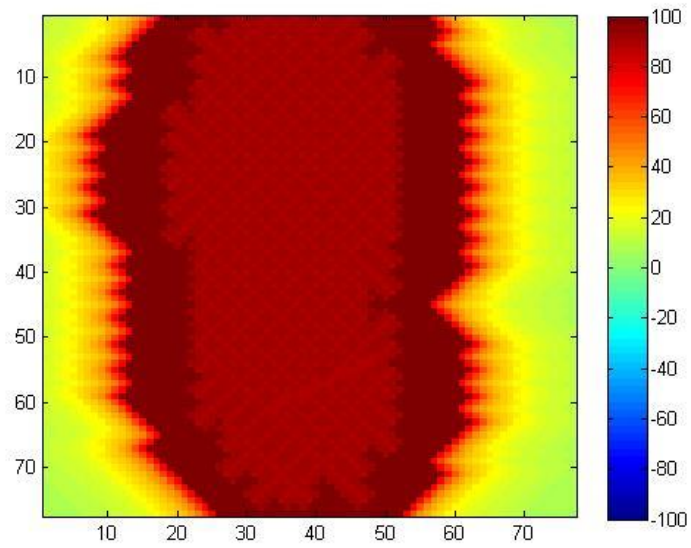


Figure 74 The 2D distribution in the middle plane of the surfacelet model from Beta wavelet with 25 data points

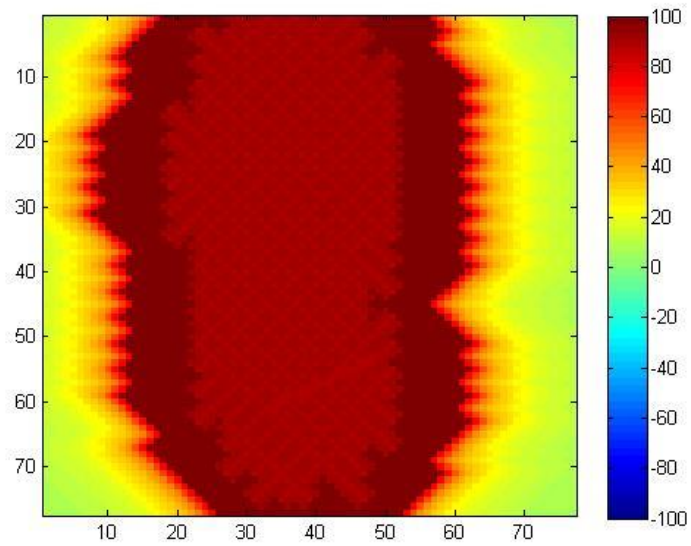


Figure 75 The 2D distribution in the middle plane of the surfacelet model from Beta wavelet with 50 data points

#### 5.4 Analysis of the Result Accuracy

In order to quantitatively determine the accuracy of the proposed method, the results of the surfacelet model are compared to the storage modulus map. Theoretically, the accuracy depends on two aspects: the feature identification accuracy and the wavelet approximation accuracy.

Although the 2D storage modulus map is given, the detailed data is not directly available from the reference. Therefore, the storage modulus values have to be obtained from Figure 68 based on the value matching between the pixels in the map and those in the legend bar. In order to simplify the calculation, sample data points are used for comparison. Therefore, the resolution of storage modulus map is decreased to 30×30, as shown in Figure 76(a). The storage modulus values are compared to the 30×30 data points in the same locations in the surfacelet model.

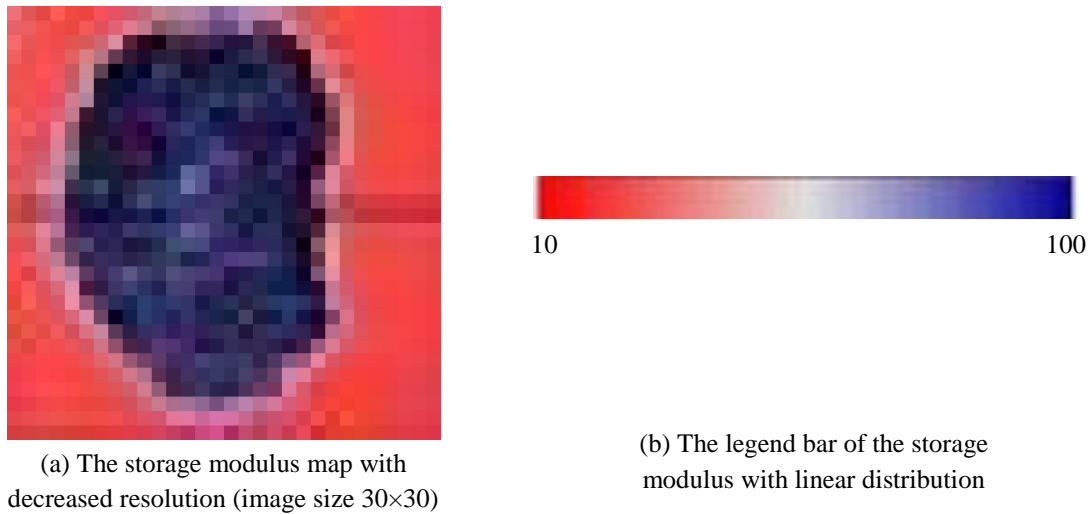


Figure 76 The derivation of the storage modulus values

The error measurement is evaluated by:

$$e = \sqrt{\frac{1}{P} \sum_{i=1}^P (M_i - M_i^0)^2}$$

where  $M_i^0$  is the  $i^{\text{th}}$  storage modulus value in the original storage modulus map in Figure 76 (a), and  $M_i$  is the one from the surfacelet model.

The resulting errors for different wavelet transforms are shown in Table 17. It can be seen from the table that the Mexican hat wavelet has smaller errors than the Beta wavelet. In addition, with the same wavelet but more data points, the error becomes smaller.

Table 17 The resulting errors between the surfacelet model and the original values for different wavelet transforms

	Mexican hat wavelet with 25 data points	Mexican hat wavelet with 50 data points	Beta wavelet with 25 data points	Beta wavelet with 50 data points
$e$	8.3	8.1	10.7	9.9

## 5.5 Discussions and Future Extensions

In this chapter, a general method to approximate material composition and local property distributions is proposed. This method is based on the feature identification result of the 3D material images, and wavelet approximation of the material composition or local property distributions along radial lines. An example is used to demonstrate the method. The proposed method is able to model the material composition and local property distributions with certain levels of accuracy, based on a proposed error metric.

The limitation of the proposed method is that it has the isotropic assumption about the material compositions or properties. The distributions are nearly identical along all radial directions and exhibit the rotational symmetry. For strong anisotropic materials, the error of the approximation is expected to be significant. Therefore, the future extension of

this method should meet the need of anisotropic materials. One possible way to do so is to combine the wavelet approximation for 1D distribution with the surface boundary approximation during the surfacelet selection process. In current procedure, the surface boundaries are united into one single implicit surface, and then plugged into 1D wavelet functions. Therefore, the current boundary domain can be represented as:

$$y(\mathbf{r}) = j_{a_j, b_k}(\min(\min(\min(r_{a_l, b_m, m_n}(\mathbf{r}))))))$$

where  $\mathbf{r} = (x, y, z)$  is the location in the domain  $\Omega$  in the Euclidean space,  $j$  is a wavelet function,  $a_j$  and  $b_k$  are the wavelet parameters,  $\rho$  is a surface function so that  $\rho(x, y, z) = 0$  implicitly defines a surface,  $m_n$  is the translation parameter of the surface, and  $a_l$  and  $b_m$  are the orientation parameters. In this method, the parameters of wavelets (type, number, etc.) and surfacelet (shape, orientation, location) are pre-selected in the current work. In future, by the combination of the wavelet approximation for 1D distribution and the surface boundary approximation, the boundary domain can be represented as:

$$y(\mathbf{r}) = \sum_{a_l} \sum_{b_m} \sum_{m_n} \sum_{a_j} \sum_{b_k} j_{a_j, b_k}(r_{a_l, b_m, m_n}(\mathbf{r}))$$

Optimization will be conducted for the parameters of  $m_n$ ,  $a_l$ ,  $b_m$ ,  $a_j$ ,  $b_k$ , with the objective of minimizing approximation errors. The numerical approaches need to be further explored.

## **CHAPTER 6**

### **A MULTI-SCALE MATERIALS DESIGN METHOD WITH SEAMLESS ZOOMING CAPABILITY**

In Chapter 3, Chapter 4, and Chapter 5, feature identification and modeling methods for material microstructures and compositions based on 3D material images from experiments are developed, which can be used in reverse engineering. In this chapter, the focus is on the *design* of material microstructures and compositions according to the specification. That is, the microstructural specification method for materials design from scratch will be developed.

As stated in Section 2.5, currently, there is no mechanism of microstructural modeling that supports multi-scale materials specification and visualization. In this chapter, a new multi-scale materials specification scheme that supports interactive design based on microstructural features is proposed. In a multi-scale design environment, a design engineer needs to specify material microstructures, compositions, and properties at certain regions of interest. Thus, a specification scheme that captures the designer's intended material distributions (microstructures, compositions, and properties) with ease of use is required. In the proposed scheme, microstructural features are used as the building blocks to allow the designer to quickly specify the material distributions. Most importantly, the proposed materials specification scheme for design has a seamless zoom-in and zoom-out capability such that materials information at multiple scales can be modeled and exchanged.

In the surfacelet based design environment, the designer can perform design specifications in both image (real) space and surfacelet (reciprocal) space. As mentioned

in Section 1.3, images are commonly used as the medium in materials design and characterization. Thus images are used to visualize specified material distributions. The image representation of materials in the image space is called *visualization model*. Surfacelet space on the other hand is used for the ease of specifying microstructural features. The most of design specification procedure is done in the surfacelet space. A user can specify the values of microstructures, compositions, or properties at discrete locations or called *collocation points* in the region of interest within the surfacelet space. The local property distribution within the domain can then be created based on a continuous *distribution model*, which is the result of interpolation from the specification. The visualization model in the image space is an evaluation of the distribution model in the surfacelet space for a particular image resolution. Since the collocation points could be selected at any locations based on the designer's need whereas regular spacing is required to generate the interpolated distribution model, a regular grid in the region of interest will be generated based on the collocation points. The regularly generated locations on the grid are called *grid points*. Some of the grid points are the specified collocation points as a result of spatial overlapping. The additional grid points are generated from the collocation points by interpolation or extrapolation.

Figure 77 illustrates the general procedure of the proposed materials specification scheme. The designer starts with specifying some collocation points in the surfacelet space. The material distributions then are generated in the image space accordingly. The specification in the surfacelet space provides the basic feature information that quickly creates the distribution. Yet, some special artifacts such as impurity, defects, and discontinuity cannot be specified easily in the surfacelet space. Therefore, the use of the



image space for specification is also necessary. After the specification of the special artifacts, a surfacelet transform can generate the corresponding specification in the surfacelet space. The special artifacts in the surfacelet space after the surfacelet transform may be continuous and represented by many discrete collocation points in the implementation. With the specified collocation points, the grid and grid points are generated. The continuous distribution model then is created by interpolation. The final specification in the image space is then generated by the inverse surfacelet transform from the evaluated distribution model in the surfacelet space. The detailed numbered steps will be explained in Section 6.2.2.

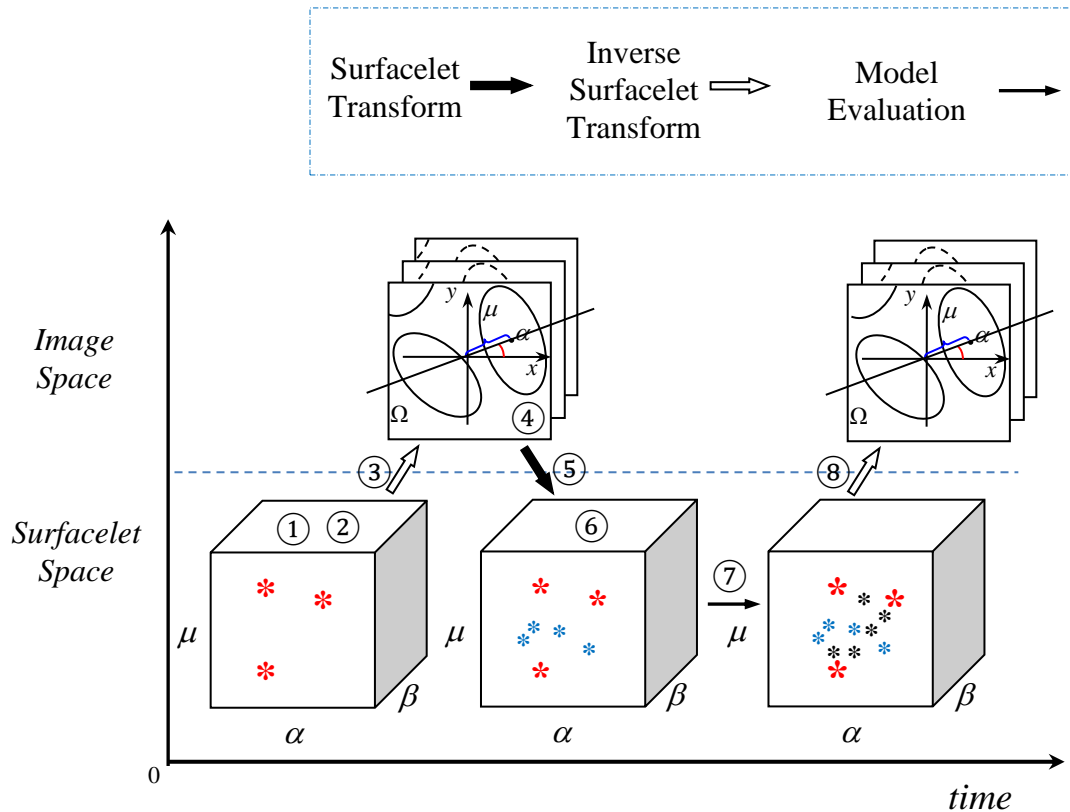


Figure 77 The general procedure of the proposed materials specification method

If the user would like to inspect the modeled materials in a specific region with finer details, he or she can perform a zoom-in operation. A smaller scale model of the region will be generated based on his or her specifications. To show the effect in a larger region as a result of the design procedure, a zoom-out operation can be performed. The operation is straight-forward. Some collocation points will be selected to generate a coarser-grid interpolation model at a larger scale. Therefore, compared to zoom-out, the zoom-in operation is more complex in a multi-scale modeling method.

In the rest of this chapter, Section 6.1 describes a collocation method that selects necessary collocation points and generates grid points in the surfacelet space at different scales during the zoom-in operation. Not all collocation points will be used in generating the distribution model at one scale. Rather, they are assigned to different levels of grids based on their spatial relationships. Only those collocation points at a particular grid level are used for a distribution model for the corresponding scale. From the specified values at the collocation points for a particular grid level, the interpolation procedure is applied to predict the values at the grid points. In Section 6.2, the details of specification scheme shown in Figure 77 will be described. During the interactive specification process, two models are kept in the design environment. One is the continuous distribution model in the surfacelet space that specifies the material distribution. The other is a discrete visualization model in the image space that shows the evaluated distribution on screen. Section 6.3 demonstrates the proposed specification scheme with examples. Section 6.4 illustrates how the proposed scheme can be integrated with material property prediction for an iterative design process.

## ***6.1 The Collocation Method for Zoom-in Operation***

The collocation method proposed here is to effectively and efficiently use the specified collocation points for interpolation at different scales. In a multi-scale modeling environment, interpolation and extrapolation are conducted based on the collocation points at different scales to generate necessary grid points in the surfacelet space. A continuous distribution model is an interpolation from the grid points. Therefore, the representation of the material distribution based on the collocation method is efficient.

The feasibility of interpolation and extrapolation in the surfacelet space is studied and discussed in Section 6.1.1. The results show that the interpolation can provide good predictions of grid points from the collocation points. In addition, the specified collocation points need to be organized to form a multi-level grid. Generally speaking, coarser collocation points covering a larger domain are utilized at a larger scale, whereas denser collocation points covering a smaller domain are utilized at a smaller scale. A mechanism to organize the collocation points into different levels based on their spatial relationships is introduced in Section 6.1.2.

### **6.1.1 Interpolation and extrapolation in the surfacelet space**

Although collocation in the image space is possible in implementing a multi-scale modeling environment, it is not efficient in capturing material distributions because the pixel values representing microstructural and compositional information are independent from each other and the interpolation or extrapolation of pixel values loses the feature information. In contrast, the interpolation or extrapolation in the surfacelet space retains feature information and provides good continuity. The idea is to predict the surface integral values in a domain from some specified ones with an interpolation model.

Adjacent surfacelets have some pixels in common, and therefore their surface integral values are dependent with each other. The interpolation thus can have good accuracy. In the interpolation model, surface integral values are functions of position and orientation parameters. Some surfacelets with selected positions and orientations are used to predict the others.

In this chapter, an example 3D image of fiber-based composite, as shown in Figure 78, is used for the demonstration of the proposed approach. Here it is also used to demonstrate the advantage of interpolation in the surfacelet space.

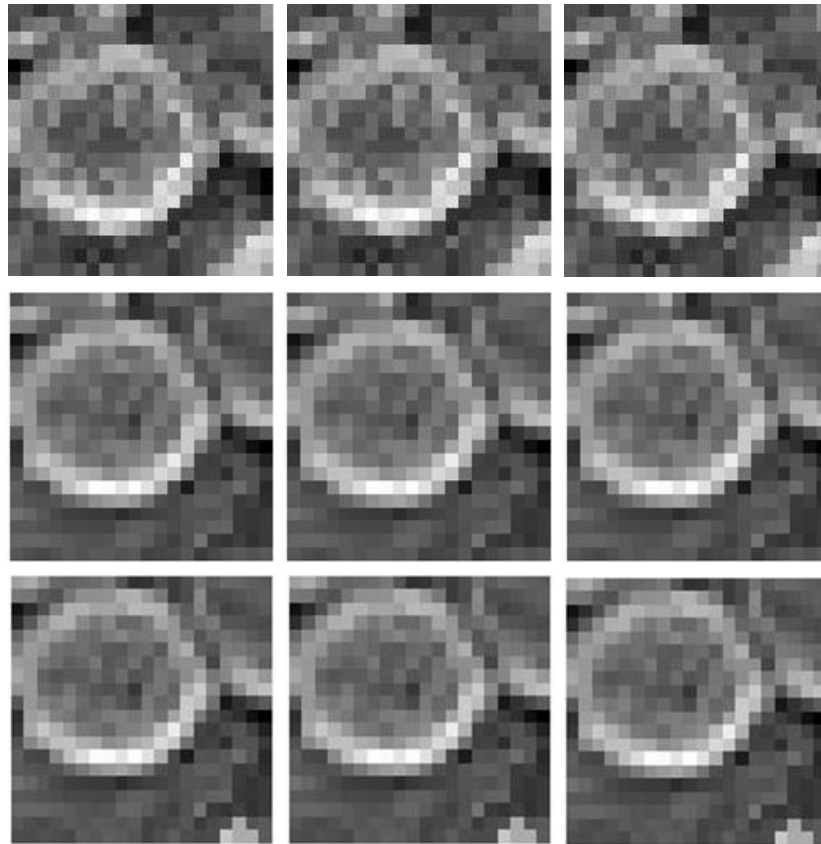


Figure 78 An example 3D image of fiber-based composite

To illustrate the interpolation in the surfacelet space, a surfacelet transform is first applied to the images in Figure 78. The ranges of the orientation parameters are set to be

$\mu \in (-D/2, D/2) = (-14.84, 14.84)$ ,  $\alpha \in [0, 2\pi)$  and  $\beta \in [-\pi/2, \pi/2]$  to ensure that the surfacelets cover all of the pixels, where  $D = \sqrt{20^2 + 20^2 + 9^2}$  is the diagonal length of the 3D images. Suppose that the numbers of discretized  $\mu$ ,  $\alpha$ , and  $\beta$  are  $u$ ,  $f$ , and  $g$  respectively. The number of surfacelets  $Q = u \times f \times g = 11 \times 11 \times 3$  is used to predict the number of surfacelets  $Q = u \times f \times g = 22 \times 22 \times 3$ . Since it is unnecessary to approximate cylindrical surfacelets in the axial direction, the interpolation of  $\beta$  is not shown.

#### 6.1.1.1 1D interpolation in the surfacelet space

Suppose that there are  $n$  surfacelets available and the prediction of other surfacelets along the direction of rotational angle  $\alpha$  is conducted. Here cubic spline interpolation is used. The cubic spline interpolation can be mathematically represented as

$$I(\alpha) = I_k + I'_k t + t^2(3(I_{k+1} - I_k) - 2I'_k - I'_{k+1}) + t^3(2(I_k - I_{k+1}) + I'_k + I'_{k+1}) \quad (6.1)$$

$(k = 1, \dots, n-1)$

where  $t = (\alpha - \alpha_k) / (\alpha_{k+1} - \alpha_k)$ ,  $\alpha_k$  is the  $k^{\text{th}}$  discretized parameter  $\alpha$ ,  $I_k$  is the surface integral corresponding to  $\alpha_k$ ,  $I'_k$  is the first-order derivative of the surface integral with respect to parameter  $\alpha$  at  $\alpha_k$ . It has the continuity of first-order derivative at the connection point between two pieces of curves.

The resulting cubic spline interpolation for parameter  $\alpha$  is shown in Figure 79, where  $\beta = \pi/90$  and  $\mu = 0$  are fixed, the ‘\*’ indicates the data point values used for the interpolation. The interpolated curve is then used to predict the values of some new surface integrals corresponding to the dots. Here both ‘\*’ and dots are evenly spaced.

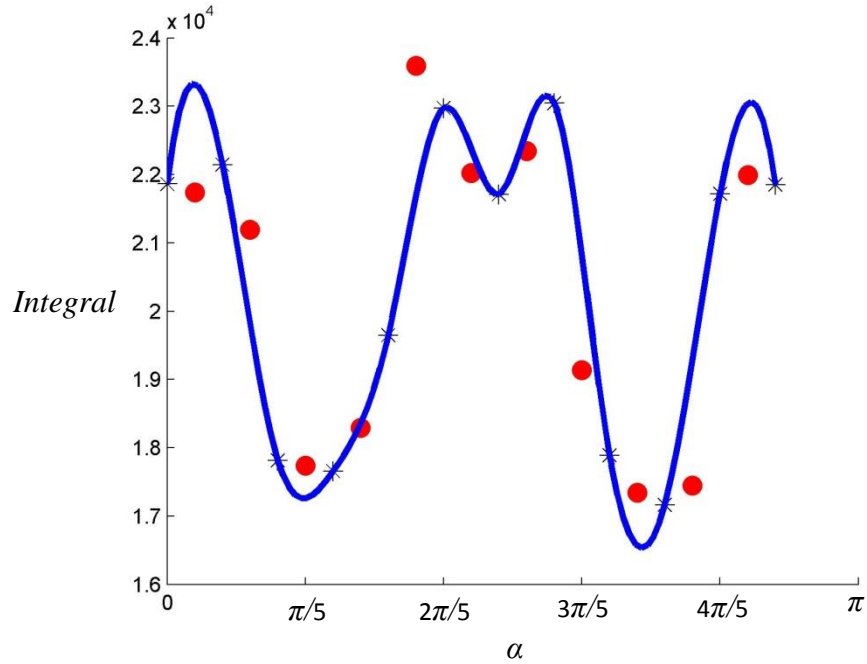


Figure 79 Result of cubic spline interpolation for parameter  $\alpha$

A piecewise cubic Hermite interpolation is also used. It is mathematically represented as

$$I(\alpha) = (2t^3 - 3t^2 + 1)I_k + (t^3 - 2t^2 + t)I'_k + (-2t^3 + 3t^2)I_{k+1} + (t^3 - t^2)I'_{k+1} \quad (6.2)$$

where  $t = (\alpha - \alpha_k) / (\alpha_{k+1} - \alpha_k)$ ,  $\alpha_k$  is the  $k^{\text{th}}$  discretized parameter  $\alpha$ ,  $I_k$  is the surface integral corresponding to  $\alpha_k$ ,  $I'_k$  is the first-order derivative of the surface integral with respect to parameter  $\alpha$ . Although Eqn. (6.1) and Eqn. (6.2) have the same results for one curve piece, the curves for entire domain are different, because the cubic Hermite interpolation does not have the continuity of first-order derivative.

With the same  $\beta$  and  $\mu$  values, the result of piecewise cubic Hermite interpolation for parameter  $\alpha$  is shown in Figure 80. It can be seen that the piecewise cubic Hermite method has better interpolation result than the cubic spline method. The smoothness of

the interpolated curve maintained by the cubic spline becomes not important in the prediction of values.

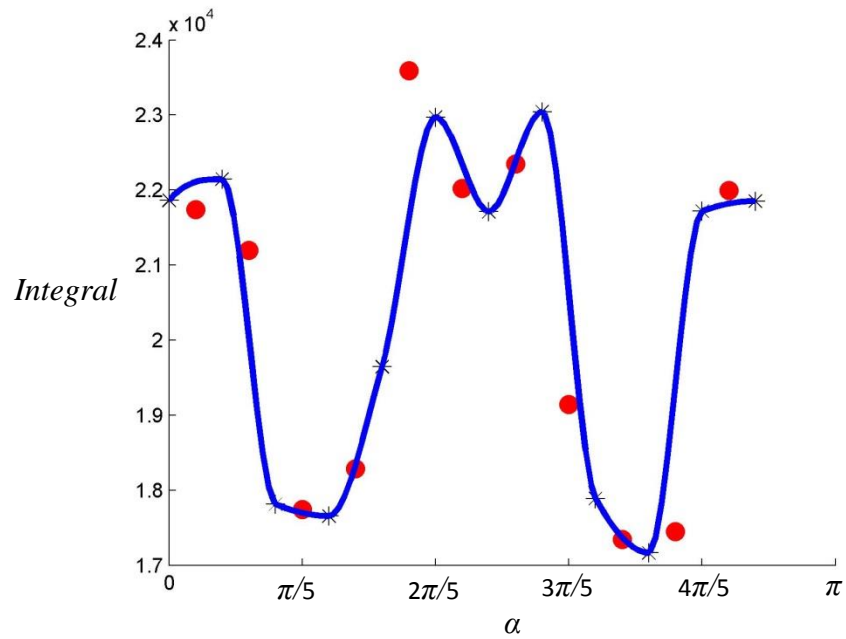


Figure 80 Result of piecewise cubic Hermite interpolating polynomial for parameter  $\alpha$

When interpolation is performed along the translation direction  $\mu$ , the result of the cubic spline interpolation for parameter  $\mu$  is shown in Figure 81, where  $\alpha=0$  and  $\beta=\pi/90$  are fixed.

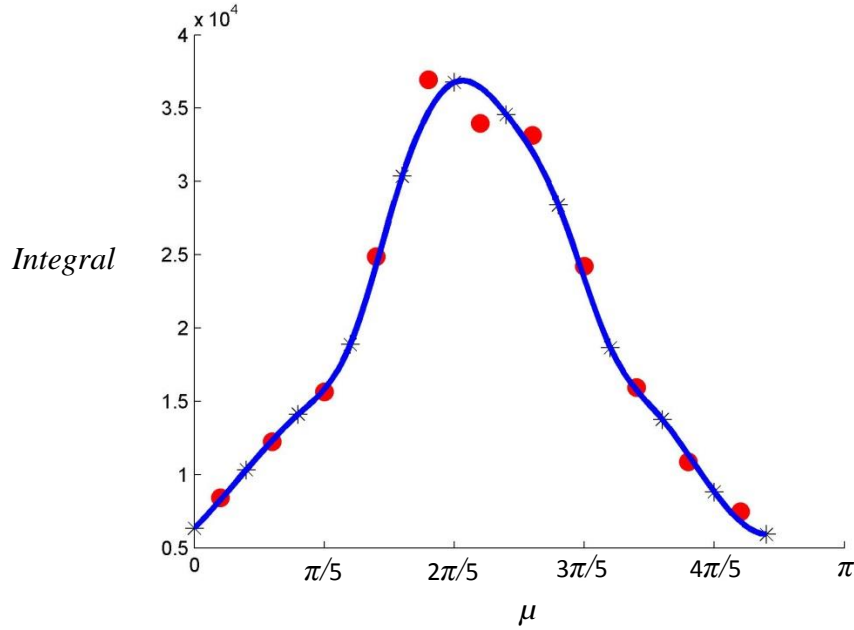


Figure 81 Result of cubic spline interpolation for parameter  $\mu$

#### 6.1.1.2 2D interpolation in the surfacelet space

The 2D interpolation in the surfacelet space is also conducted to show the feasibility of surface integral prediction. The 2D cubic spline interpolation is mathematically represented as:

$$I(x, y) = \sum_{i=0}^3 \sum_{j=0}^3 a_{ij} x^i y^j$$

where the  $x$  coordinate is the value of parameter  $\alpha$ , and the  $y$  coordinate is the value of parameter  $\mu$ , and  $a_{ij}$  are the coefficients of the polynomial.

When  $\beta=\pi/90$  is fixed, and the interpolation for both rotation  $\alpha$  and translation  $\mu$  is applied, the result of the cubic spline interpolation for parameter  $\alpha$  and  $\mu$  is shown in Figure 82. In Figure 82, ‘\*’ indicates the data point values used for the interpolation. The interpolated curve is used to predict the values of some new surface integrals that correspond to the red dots. Both types of dots are evenly spaced. It can be seen from the



figure that, the red dots are very close to the interpolated surface. Therefore, the interpolation of both rotation  $\alpha$  and translation  $\mu$  can well predict surface integral values.

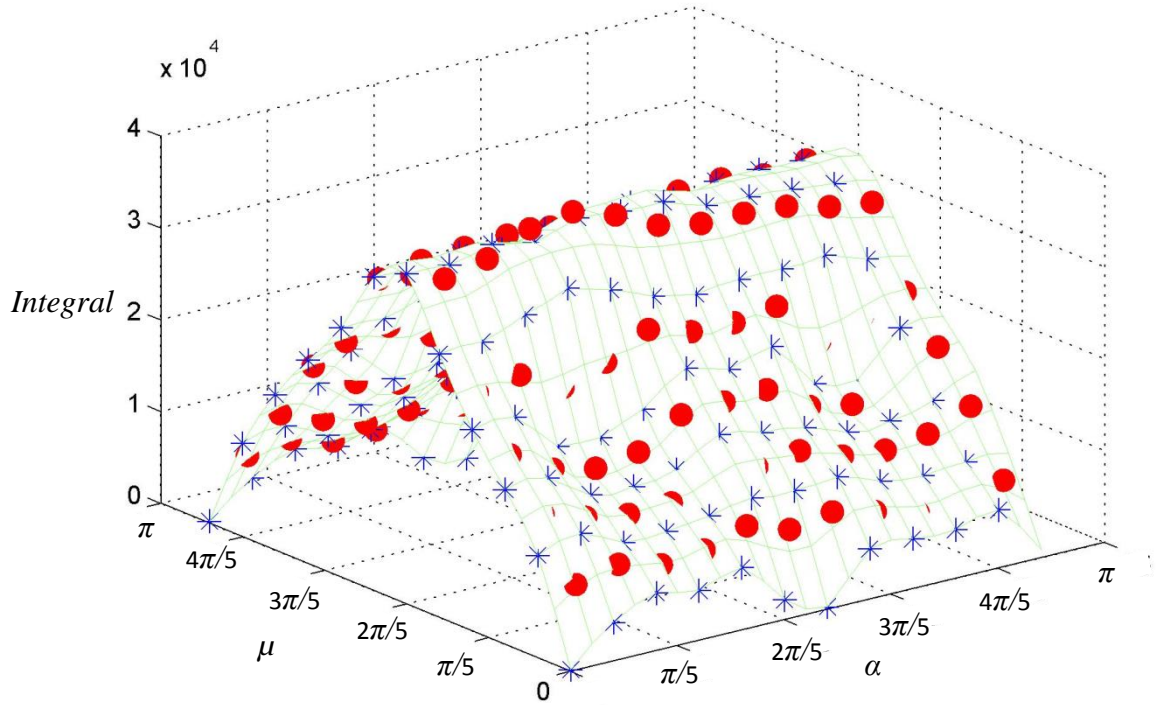


Figure 82 Result of 2D cubic spline interpolation for parameter  $\mu$  and  $\alpha$

From the results of both 1D and 2D interpolation, it can be seen that the true value can be predicted by the interpolated curves or surfaces. The interpolation of surface integral values provides a good prediction without losing feature information. Throughout the process, the information of spatial correlation among pixels that form the feature is maintained.

### 6.1.2 Collocation for zoom-in and zoom-out operations

In this subsection, the proposed collocation method for zoom-in and zoom-out operations is described. The proposed method is general enough for all interpolation or extrapolation basis functions. The general principle for 2D cases is described as follows.

### 6.1.2.1 Collocation grid

From user specified data points, a regular collocation grid needs to be determined such that the spatial relationship of the data points is determined, and spatially organized collocation points can be generated for interpolation. The grids represent levels of data, whereas the collocation points are selected for interpolation and extrapolation at different levels. The general rule of grid generation is that grids should be oriented to cover all collocation points in the domain but with the smallest grid area. The subdivision patterns used to generate multi-level grids used in this research are *bi-sectional* and *golden-ratio*, although other patterns can also be applied for the proposed zoom operations. Bi-sectional pattern just simply divides each side of the domain by halves with one additional grid point introduced (as shown in Figure 83), whereas golden-ratio pattern introduces two additional grid points for each side with the golden ratio of distances (as shown in Figure 85).

A 1D example of the bi-section collocation scheme is shown in Figure 83(a), and a 2D case is shown in Figure 83(b). In Figure 83(a), ‘\*’ represents a first-level collocation point, and ‘o’ represents a second-level collocation point between the two first-level collocation points. As shown in Figure 83(b), the collocation points are formed at different levels, which are used in the zoom operation. All collocation points are specified by the user. The collocation points of the first level are predetermined, which are the four corner points in the whole domain. The point located at the middle of the line formed by two first-level collocation points, as the result of bi-section, is at the second level. Similarly, the point at the middle of the line formed by a pair of second-level collocation points is at the third level. It is possible that the collocation points cannot be

categorized in adjacent levels, such as the example in Figure 83(b) where no collocation points are at level 2. When a point is specified in the surfacelet space, the level where the point belongs to can be calculated. When a collocation point has a distance to a grid point that is within a given tolerance, it is moved to the corresponding grid point as the quantization to reduce the total number of levels in the problem.

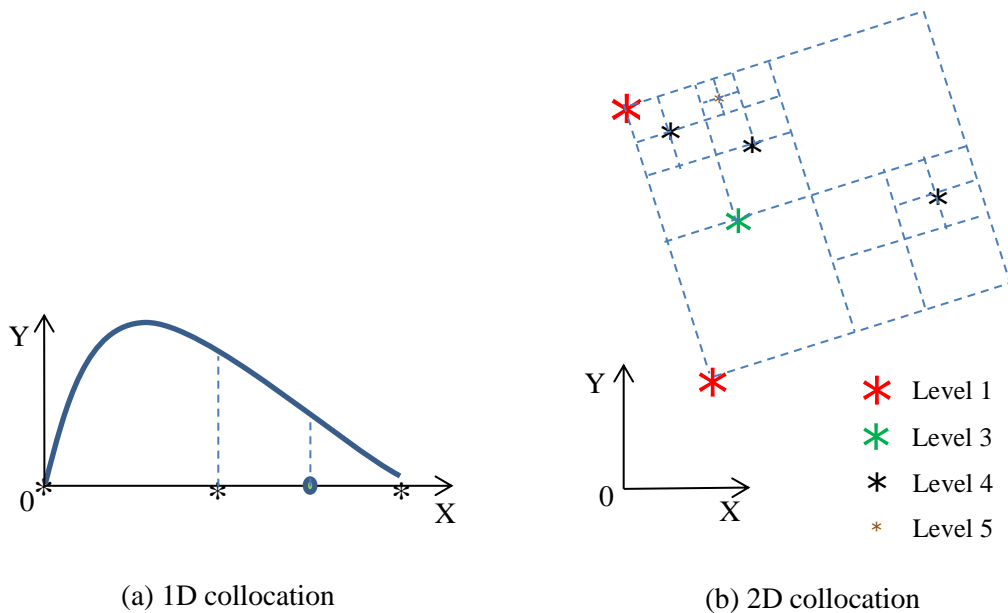
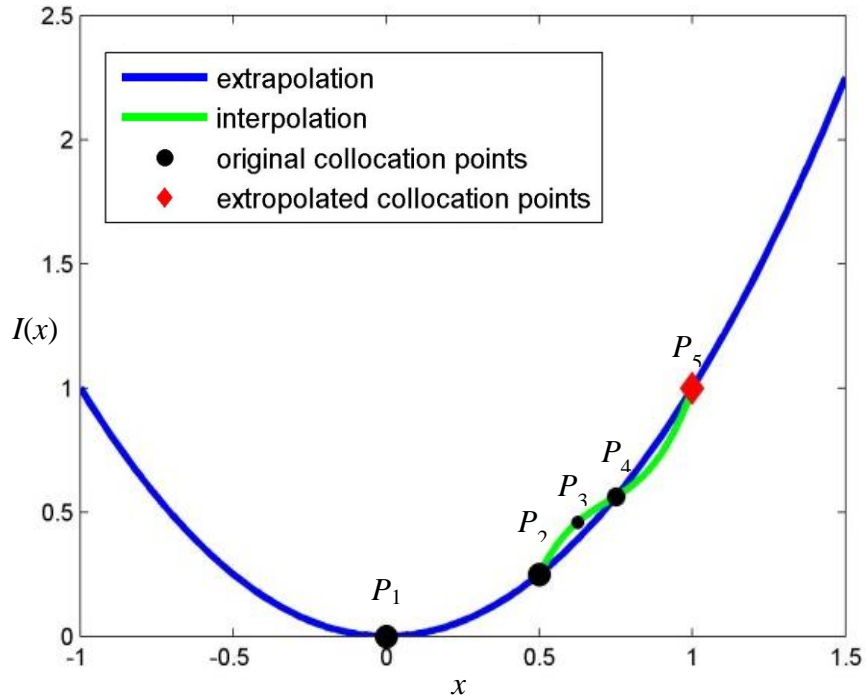


Figure 83 Determination of the levels of collocation points

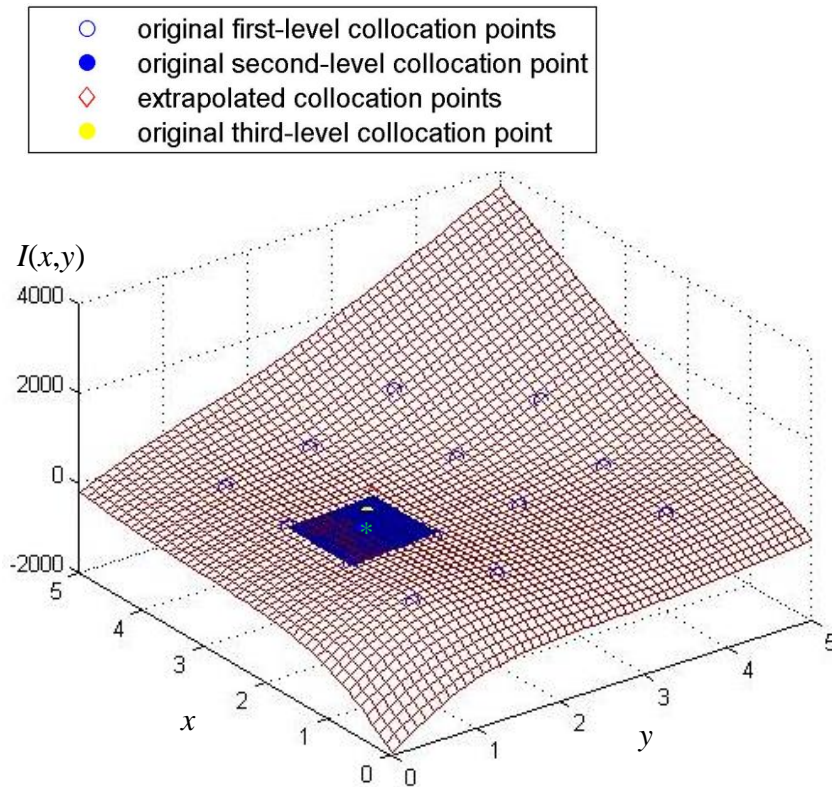
### 6.1.2.2 Zoom-in operation

For a material region that the user is interested in specifying the details, a zoom-in operation is conducted. The zoom-in operation is realized by interpolation in the surfacelet space. For the interpolation, three adjacent levels of collocation points are needed to ensure the smoothness of zoom-in operation. At the lowest level among the three used in the zoom-in operation, a complete set of grid points in the region of interest is required for the operation. If the values of some of the grid points are missing, extrapolation from other known grid points is needed. The extrapolation procedure is

illustrated in Figure 84(a). In this 1D example, the grid is bi-sectional. The original collocation points correspond to the value pairs at  $P_1=[0, 0]$ ,  $P_2=[0.5, 0.25]$ ,  $P_3=[0.625, 0.39]$ , and  $P_4=[0.75, 0.5625]$ , where the first value is the  $x$  coordinate and the second one is its surface integral value  $I(x)$ . The first-level grid points are those at  $x=0.5N$ , where  $N$  is an integer, such as  $P_1$  and  $P_2$ . The second-level grid points include the first-level ones as well as those grid points between the first-level ones by bi-section, such as  $P_1$ ,  $P_2$ , and  $P_4$ . Similarly, the third-level grid points include the first-level, second-level, as well as those between the second-level grid points, such as  $P_1$ ,  $P_2$ ,  $P_3$ , and  $P_4$ . To zoom into the sub region of  $x \in [0.5, 1]$ , a new grid point  $P_5$  at  $x=1$  is needed. The surface integral value of  $P_5$  is estimated by extrapolation from  $P_1$ ,  $P_2$ , and  $P_4$ . In this example, a cubic spline is used. The result  $P_5=[1, 1]$  is obtained. Then  $P_2$ ,  $P_3$ ,  $P_4$ , and  $P_5$  are utilized to generate an interpolation model that can be used to describe other intermediate points in the region of  $x \in [0.5, 1]$ . The interpolation is the resulting model after the zoom-in operation. Similarly, a 2D example is shown in Figure 84(b). Notice that extrapolation is always conducted based on the data points on two adjacent levels of grid points, and the extrapolated grid points are always on the lower level grid.



(a) A 1D zoom-in example



(b) A 2D zoom-in example

Figure 84 1D and 2D zoom-in examples

### 6.1.2.3 Zoom-out operation

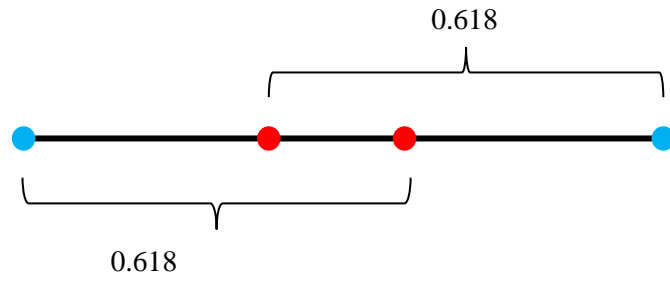
After the user specifies the detailed material information at small scales with the zoom-in operation, the user usually wants to zoom out to check the overall microstructure and material distribution, or move to another region to perform the zoom-in operation. In the zoom-out operation, there are two approaches to create grid points of a larger scale model. The first approach is to choose some existing grid points that also belong to a smaller scale so that the larger scale model can be generated. The second approach is a homogenization approach where the surface integral value at a grid point of the larger scale is the average of the values at some adjacent grid points in the smaller scale model. After the grid points of the larger scale model are chosen, the interpolation scheme is applied to predict any unknown position following the same procedure in the zoom-in operation. For instance, in Figure 84(a), if the user wants to visualize the entire material domain, the grid points  $P_1$ ,  $P_2$ , and  $P_5$  can be chosen for a larger scale model from the original small one. The larger scale model is the interpolated model based on  $P_1$ ,  $P_2$ , and  $P_5$ .

### 6.1.2.4 The golden-ratio pattern for zoom-in and zoom-out operations

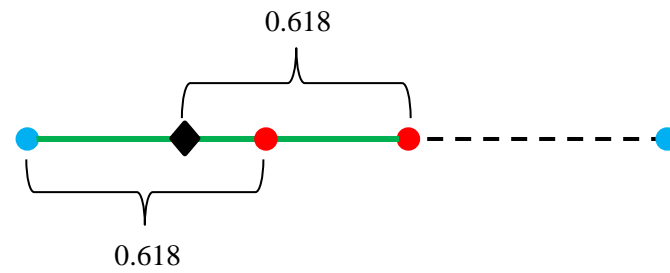
Multiscale zoom-in and zoom-out operations are usually conducted with uniform grids, such as in Wang et al. [4]. In this collocation grid scheme, the size of the domain in the next finer scale is restricted to one half of the current scale. As a result, domains at other scales in-between are neglected. This makes the zoom-in and zoom-out operations not as flexible and smooth as the users want. Therefore, zoom-in and zoom-out operations with other grid schemes are desirable. In this research, a golden-ratio based collocation grid method is proposed for more flexible zoom operations to support

multiscale design. The golden ratio is widely used in optimization, esthetics, and music. It has the capability of scaling down to a smaller scale with only one additional point, as shown in Figure 85. The ratio is utilized as the basis of a new zooming scheme. Similar to the uniform grid, the golden ratio grid pattern ensures that the relative distances among the grid points are not changed for each zoom operation. Therefore the interpolation basis functions can remain the same. This provides numerical convenience during the zoom operations.

As shown in Figure 86, the next finer scale based on the golden-ratio collocation grid scheme has a larger domain than the one based on the uniform grid scheme. In each zoom-in operation, the dimension of the domain shrinks 50% for the uniform grid but only 38.2% for the golden ratio grid. Therefore, the zoom-in operation of the golden ratio grid is smoother than that of the uniform grid. At the same time, the number of the additional grid points is relatively smaller. For a 2D domain, 7 new grid points out of a total of 16 in the complete grid need to be inserted for each zoom operation, whereas in the uniform grid scheme 5 new grid points out of a total of 9 need to be inserted. The number of the additional grid points for the uniform grid in 3D is 19 out of a total of 27, while the number of the additional grid points for the golden ratio grid in 3D is 37 out of a total of 64. The relatively grid point addition is 70.4% for the uniform grid and 57.8% for the golden ratio grid.

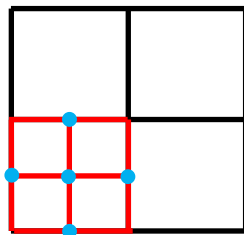


(a) The golden ratio

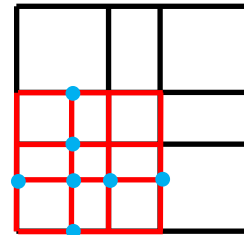


(b) The scale-down with golden ratio

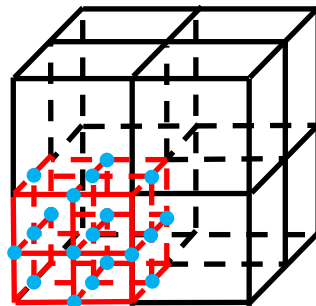
Figure 85 The illustration of golden ratio



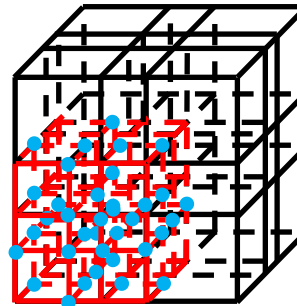
(a) Uniform grid in 2D



(b) Golden ratio grid in 2D



(c) Uniform grid in 3D



(d) Golden ratio grid in 3D

Figure 86 Comparison between uniform and golden ratio grid in zoom-in operations for 2D and 3D domains



## ***6.2 Multi-scale Materials Design Process***

### **6.2.1 The combination of the distribution model in the surfacelet space and the visualization model in the image space**

Here the visual zoom operations are differentiated from the material model zoom operations. During the material model zoom operations in the surfacelet space, the underlying material distribution models are created or modified. In contrast, the zoom operations in the image space only provide different visualization models without affecting the distribution models in the surfacelet space.

Because the size of 3D material images is usually large, in order to improve computational efficiency, it is desirable to use images with the resolution as low as possible in the design process. During the visual zoom-in and zoom-out operations, images at different visual scales have the same underlying material distribution model in the surfacelet space, although more pixels may be shown for a region of interest with more detailed material information to be visualized. The visual zoom-in and zoom-out operations can be simply conducted through changing the image resolution and re-evaluating the underlying material distribution model in the surfacelet space.

### **6.2.2 Detailed design steps**

The general procedure of the multi-scale design process is shown in Figure 77. The detailed steps are listed in Figure 87 and described as follows.

In Step 1, appropriate types and shape parameters of surfacelets are decided to represent the geometry of the microstructural features. The determined surfacelet forms affect the data exchange between the image and surfacelet spaces. It should be noted that

the type of the surfacelet is not limited to the existing surfacelet primitives. It can also be composite surfacelets that are combined with those surfacelet primitives.

In Step 2, the location and orientation of a feature are specified as a point in the surfacelet space. Once the type and size of a surfacelet are determined, a microstructural feature in the image space can then be created based on the specified point in the surfacelet space. This makes the design process easier and more accurate than directly creating features in the image space.

In Step 3, the visualization model in the 3D material image space can be obtained through the inverse surfacelet transform of the intermediate result from Step 2 in the surfacelet space. Since only the boundaries need to be reconstructed, the general optimization based approach for the inverse surfacelet transform, as illustrated in Chapter 3, is not necessarily applied. Instead, a simple scheme that set the pixels on the boundaries to be equal can be used.

In Step 4, more detailed material microstructural information, i.e. special artifacts, is specified in the image space across different visual scales. The microstructural information specified in this step is usually irregular, such as cracks or impurities, which are not efficient to be specified in the surfacelet space.

In Step 5, the forward surfacelet transform is applied so that the surfacelet representation of the resulting material images from Step 4 is obtained.

In Step 6, the interpolation or extrapolation is applied to build the grid based on the specified collocation points from Step 5. The continuous material distribution model is then constructed in the surfacelet space.

In Step 7, the continuous distribution model constructed in Step 6 is evaluated first in the surfacelet space so that the desirable resolution is obtained by introducing more surfacelets.

In Step 8, the inverse surfacelet transform is applied to the evaluated distribution model in the surfacelet space and the final material distribution as the result of specification process is obtained in the image space.

If zoom-in or zoom-out operations are needed, the above eight-step specification process can be repeatedly applied. Based on the zoom procedures in Sections 6.1.2.2, 6.1.2.3, and 6.1.2.4, new specified collocation points in the new scale are obtained. Then these collocation points in the surfacelet space will be used as the initial specification for Step 1 of the above process. The zoom-in and zoom-out operations can be applied repeatedly.

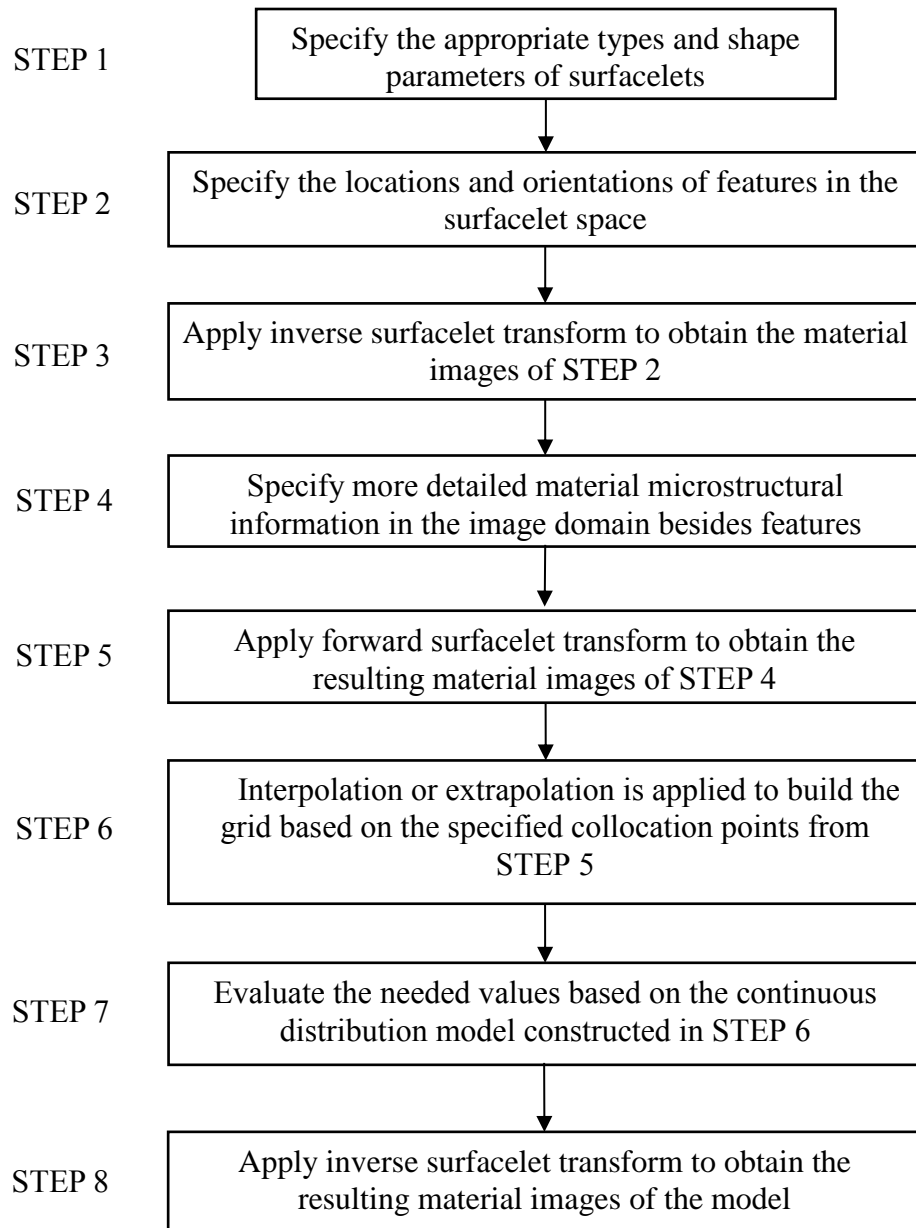


Figure 87 The general procedure of the computer-aided material microstructure design process

## 6.3 Examples and Results

### 6.3.1 Bi-sectional grid

In this section, an example of fiber-based composites is used to demonstrate the proposed multi-scale materials specification method. In this example, a representative

volumetric element (RVE) of the fiber composite is used, which contains three fibers with different locations and orientations. The composite has three regions: the fiber, the matrix, and the fiber-matrix interphase. The interphase is the gradient mixture between the fiber and matrix materials in the fiber boundaries. Both the fiber and the matrix materials are homogeneous. The fiber-matrix interphase is also of the interest for multi-scale material specification in addition to the fiber and the matrix. In this example, all images that show the intermediate results during the design specification process have the same resolution. The image size is chosen as  $20 \times 20 \times 9$  pixels. The origin of the image space is at the middle of the 3D image. The size of the image domain is  $x, y, z \in [-1, 1]$  for all visual scales.

In the first step, the shape parameters of the fibers are specified. In this example, the only shape parameters, which are the radii of fibers, are set to be 0.5. It should be noted that this number is proportional to the image domain, which is  $[-1, 1]$  for all  $x$ ,  $y$ , and  $z$  directions.

In the second step, the locations and orientations of the three fibers are specified in the surfacelet space. As discussed in Section 3.2, the dimension of the surfacelet space generally corresponds to the number of orientation and position parameters used in the surfacelets. However, for this example, the fourth parameter, the radius  $r$ , is introduced as the shape parameter in addition to  $\alpha$ ,  $\beta$ , and  $\mu$  in order to model the gradient of the interphase region.

In this example, the size of the surfacelet domain is  $u \times f \times g \times s = 30 \times 30 \times 4 \times 6$ . The ranges of the orientation parameters are set to be  $\mu \in (0, D/2) = (0, 1.73)$ ,  $\alpha \in [0, 2\pi)$ ,  $\beta \in [-\pi/2, \pi/2]$  and  $r \in [0, 3]$  to ensure that the surfacelets cover all of the

possible surfacelet positions and orientations, where  $D = \sqrt{2^2 + 2^2 + 2^2}$  is the diagonal length of the 3D images. The user specified coordinates for the three collocation points in the surfacelet space are [0.692, 1.257, 0.5], [1.386, 1.885, 0.5], and [0.693, 4.398, 0.5], or at the indices of [12, 6, 6], [24, 9, 6], and [6, 21, 6] respectively. They are shown in Figure 88. The surfacelet space is 4D. Because the three fibers have the same parameter value of  $\beta$ , only the subspace of  $\alpha$ ,  $\mu$ , and  $r$  is shown in the figure. The three collocation points have the same value for parameter  $r$ , which indicates that the three surfacelets have the same radius.

In the third step, by the inverse surfacelet transform, the 3D material images can be obtained. The pixel values on the boundaries are set to be equal. In this example, all pixel values are set to be 255. The result is shown in Figure 89. To show the contrast with the result in a higher resolution (more discrete values in the image space), an image with the resolution of  $50 \times 50 \times 9$  with the same material distribution model is shown in Figure 90. It can be seen from Figure 90 that the position and orientation, as well as the boundary information of the fibers, are visually very clear. In contrast, in Figure 89, because the image resolution is low, only the position and orientation information of the fibers is identifiable, and the boundary information is not clear. Therefore, the visual zoom-in operation is typically required for specifying the interphase of fiber composites. The zoom-in ratio is 4 in this example. The result of the visual zoom-in operation is shown in Figure 91 (b).

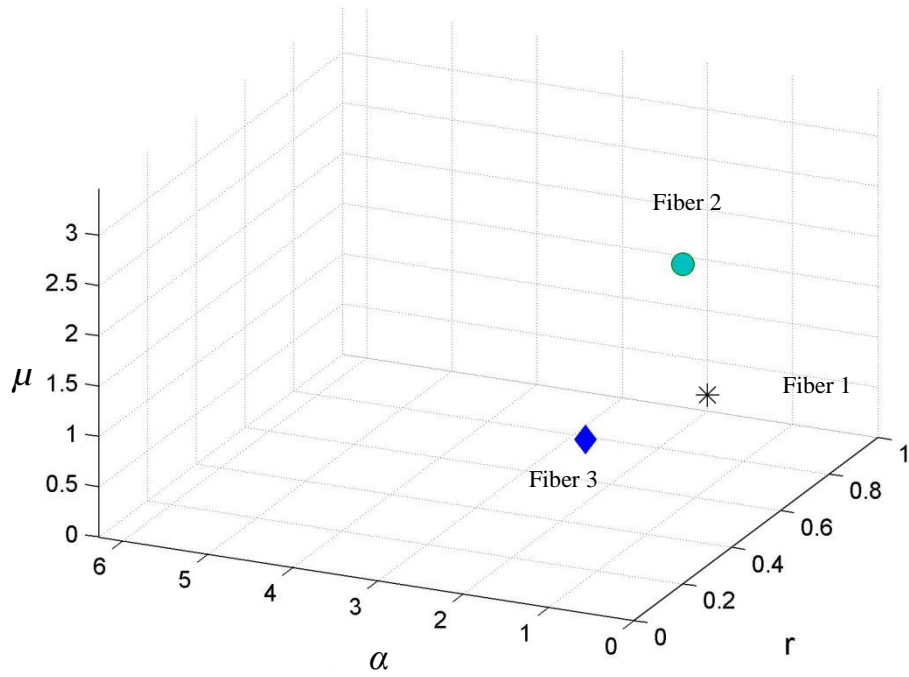


Figure 88 The specification result of locations and orientations of the three fibers in the surfacet domain at STEP 2

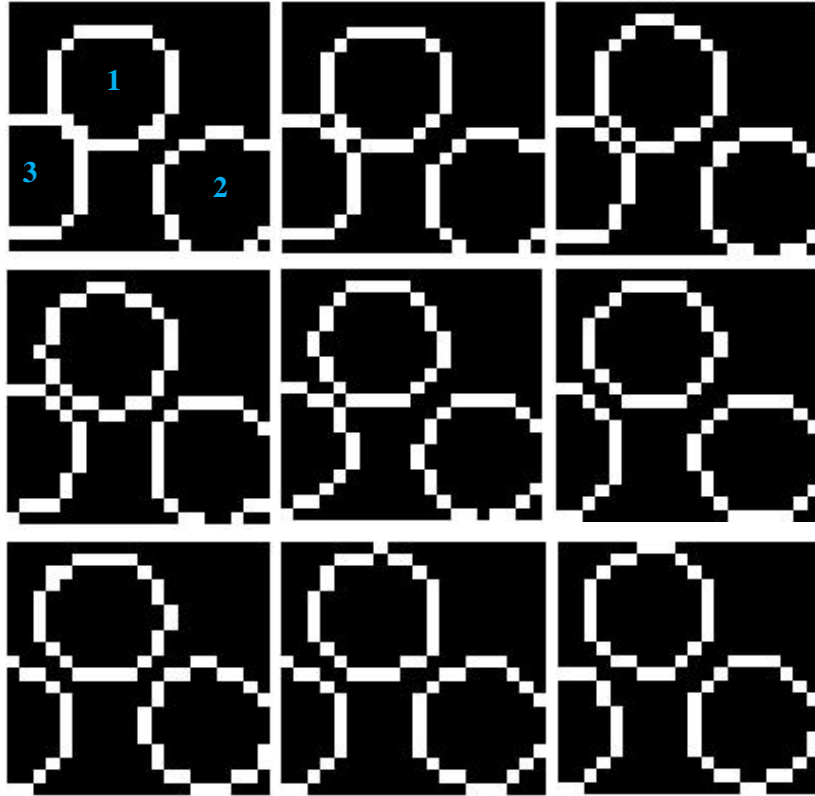


Figure 89 The result of inverse surfacelet transform at STEP 3 (the size of the 3D image is  $20 \times 20 \times 9$ )

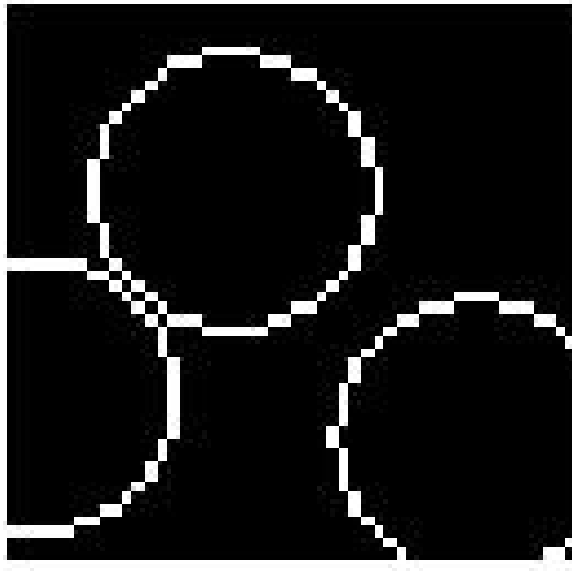


Figure 90 The first slice of the resulting image of inverse surfacelet transform at Step 3 with enhanced resolution (the size is  $50 \times 50 \times 9$ )



In the fourth step, more detailed material microstructural information is specified in the image space. This is essential for specifying a nonlinear gradation of material composition. In this example, four additional isosurfaces are specified with two for the interphase region and the other two for the internal region of the fiber. There is no crack or impurity specified in this example. The four additional isosurfaces for Fiber 2 are specified in the image space with four different isovalues of the surfacelet, which are - 0.2, -0.1, 0.05 and 0.1 respectively, in order to model the interphase and internal region of Fiber 2. As an example, for the interphase region, the pixel values on the isosurface with the isovalue of 0.03 are set to be 173, and the ones with the isovalue of 0.06 are set to be 32. For the internal region, the pixel values on the two additional isosurface are all set to be 255, assuming a uniform composition inside the fibers. It should be noted that the direct specification of the four additional isosurfaces on the resulting image of Step 3 is technically feasible. However, since the interphase regions are usually thin compared to the radius of the fibers, and one pixel represents a large region in the low-resolution images, it is likely to be inaccurate and inconvenient to specify with these images. The first slice of the result is shown in Figure 91 (c) for comparison. The full 3D image is shown in Figure 92.

In the fifth step, the forward surfacelet transform is applied so that the surfacelet representation of the material images from Step 4 is obtained. Since the origin of the image space is always in the middle of the 3D image at the current visual scale, the coordinate system is changed during the visual zoom-in operation, and the parameters and all of the coordinates for all five surfacelets are changed. When there is no crack or impurity specified in STEP 4, the new parameters and coordinates of the surfacelets can

either be obtained through coordinate system transformation or feature identification in the forward surfacelet transform. In this chapter, to demonstrate the general method, the method of feature identification is utilized. The result is shown in Figure 94, where the sizes of the circular markers indicate the surface integral values. To show the accuracy of the feature identification result, the surfacelets are shown in the image space by the inverse surfacelet transform. The result is shown in Figure 91 (d) for comparison. The full 3D image is shown in Figure 93. It can be seen that there is only slight difference between the results in Figure 91 (c) and (d), and also between Figure 92 and Figure 93.

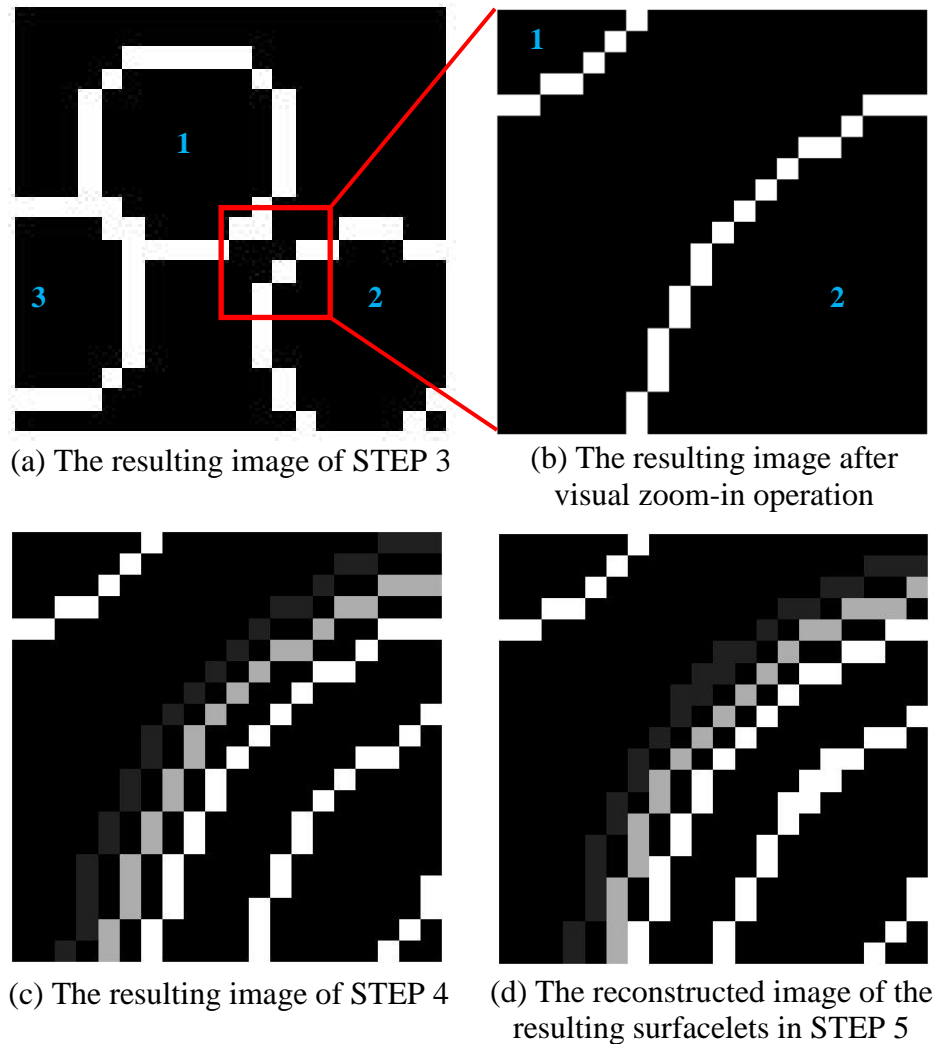


Figure 91 Zoom-in and details design of fiber-matrix interphase

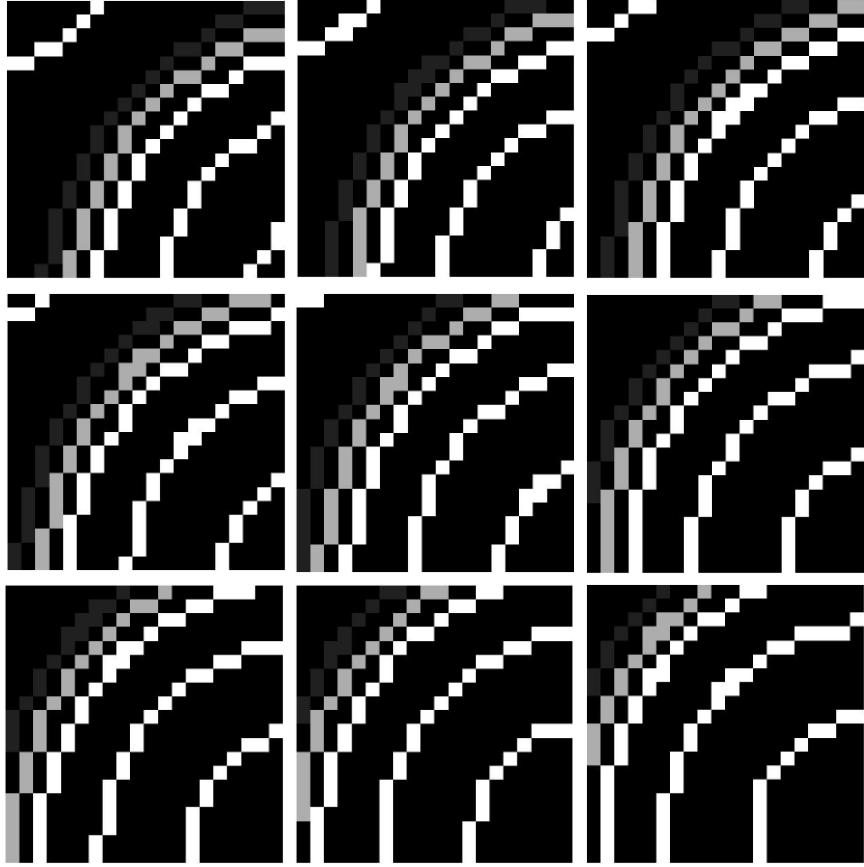


Figure 92 The full resulting 3D image of STEP 4

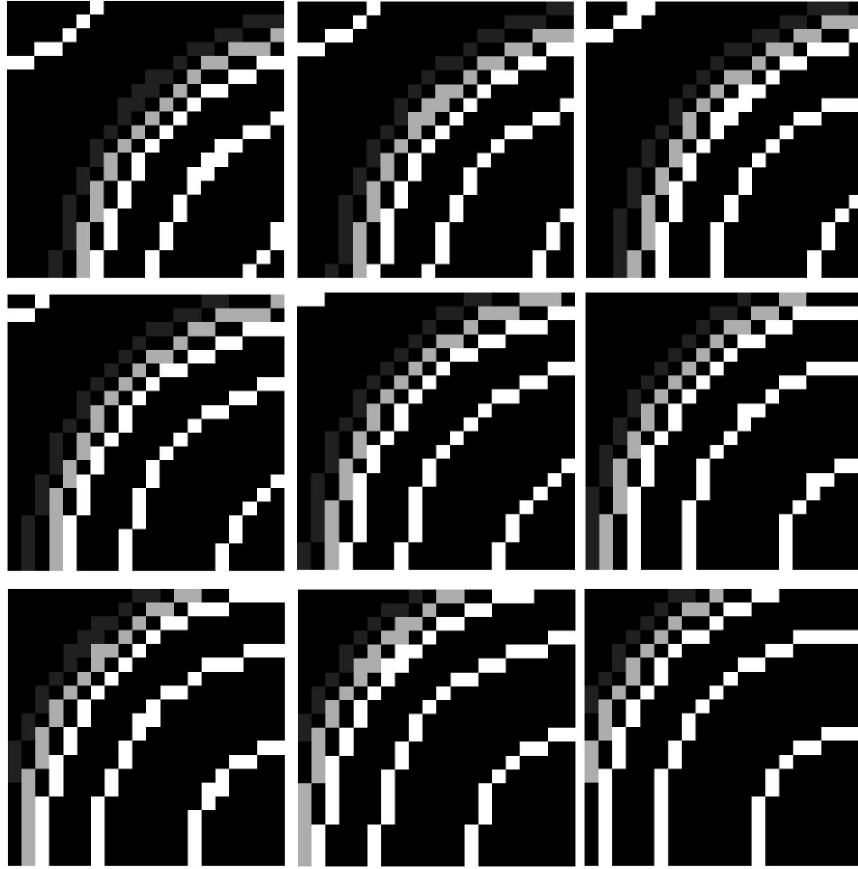


Figure 93 The full reconstructed 3D image of the resulting surfacelets in STEP 5

In the sixth step, the continuous material distribution model is constructed by interpolating the five collocation points in the surfacelet space for fiber 2 as a result of the previous step. A cubic spline is used in this example.

In the seventh step, the continuous distribution model constructed in the sixth step is evaluated in the surfacelet space. Surface integral values of the surfacelets between the five specified ones in the surfacelet space are predicted with from the cubic spline. The result is shown in Figure 95.

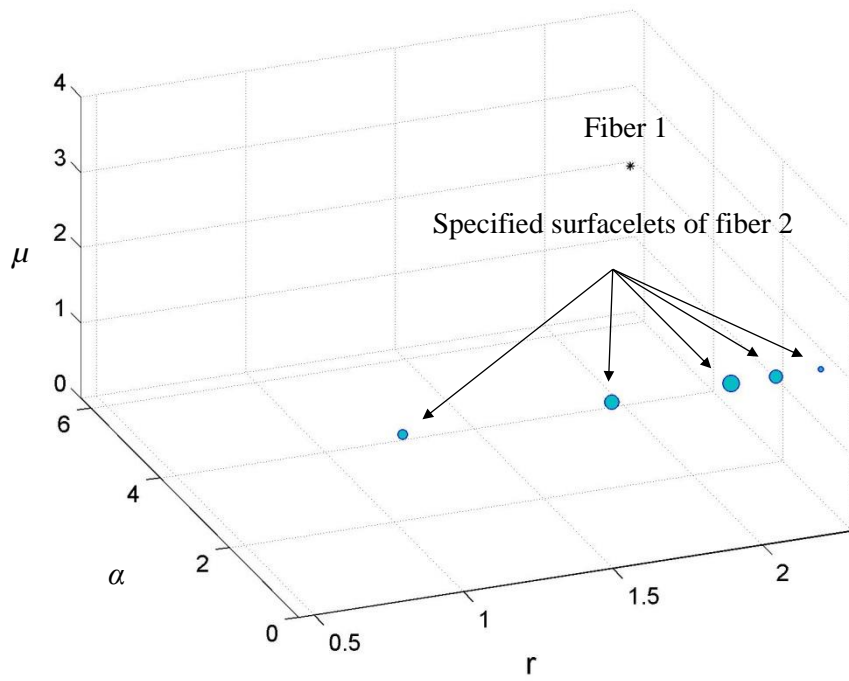


Figure 94 The result of STEP 5

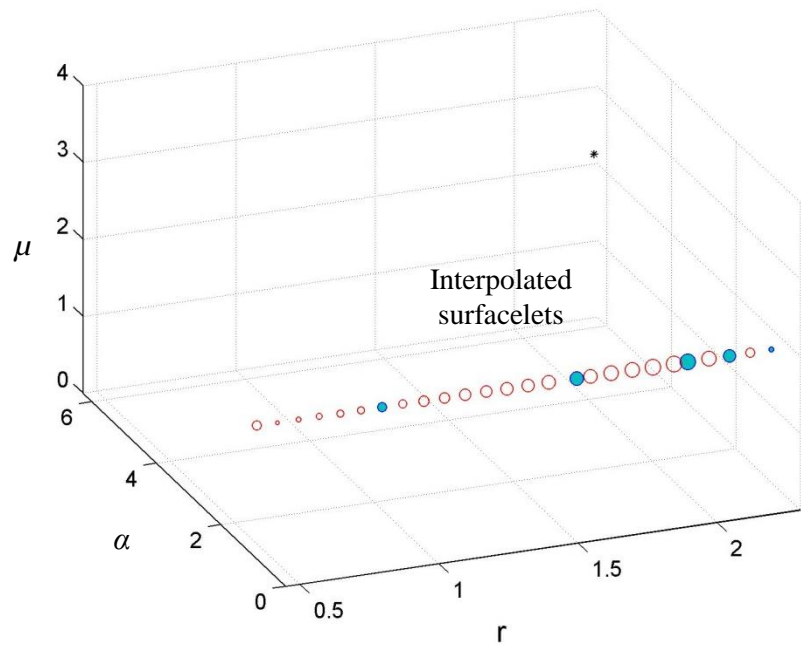


Figure 95 The result of STEP 7

In the last step, the visualization model in the image space is obtained through the inverse surfacelet transform from the evaluation of the distribution model from the seventh step. The pixel values on the same surfacelet are assumed to be the same in this example. When a pixel is on two surfacelets at the same time, the pixel value is the average of the two possible values. The full reconstruction result is shown in Figure 96. Some of the detailed pixel values of the resulting image after the model zoom-in operation in the box region indicated in Figure 96 are listed in Table 18. It is seen that a continuous distribution of materials in the interphase region is obtained.

After the specification of the detailed interphase information of Fiber 2, a zoom-out operation can be conducted for the visualization of the overall microstructure. In this example, the image is zoomed out by 4 times of the original visual scale. The surface integral value at the specified middle collocation point in Figure 94 is used. The result of the zoom-out operation is shown in Figure 97. It is seen that the interphase region has no continuous distribution any more. Suppose that the designer would like to zoom into the interphase region further from the result in Figure 96, the new set of collocation points can be generated either by new specifications in the smaller region from the designer, or by evaluating the distribution model created in the above procedure at the user-specified locations. The new set of collocation points then are used to create the more detailed distribution model, following the same procedure in Figure 77.

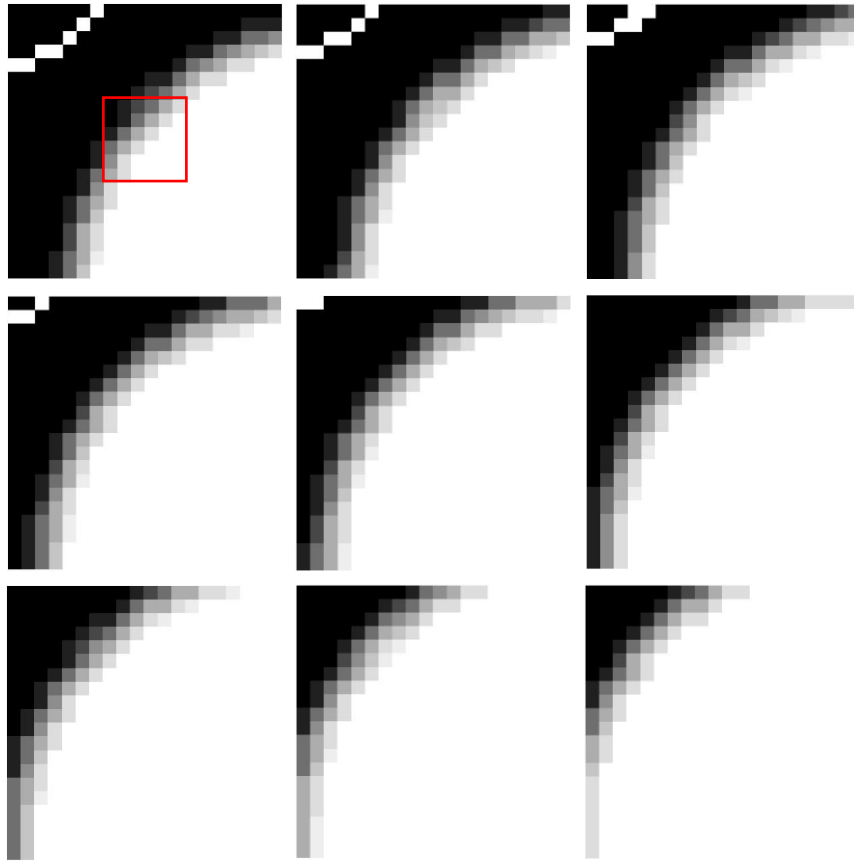


Figure 96 The image reconstruction result in STEP 8

Table 18 Pixel values of the box region indicated in Figure 96

		Pixel number in the horizontal direction					
		<b>8</b>	<b>9</b>	<b>10</b>	<b>11</b>	<b>12</b>	<b>13</b>
Pixel number in the vertical direction	<b>7</b>	0	0	32	71.4	110.8	173
	<b>8</b>	0	32	71.4	110.9	173	220.4
	<b>9</b>	0	32	110.9	173	220	225
	<b>10</b>	32	110.9	173	220	255	255
	<b>11</b>	110.9	173	220	255	255	255
	<b>12</b>	141.9	220.4	255	255	255	255



Figure 97 The resulting image of the zoom-out operation (the first slice only)

### 6.3.2 Golden-ratio grid

In this subsection, the scheme of golden-ratio grid is demonstrated with an example of ellipsoidal surfacelet. Still, material composition is modeled in this example. The image size is chosen as  $20 \times 20 \times 9$  pixels. The origin of the image space is at the middle of the 3D image. The size of the image domain is  $x, y, z \in [-1, 1]$  for all visual scales.

The equation of an ellipsoidal surfacelet is shown in Eqn. (2.3) in Section 2.1.2. In order to simplify the description and emphasize on the collocation, the steps before Step 5 are neglected. In this example, only the boundary portion or the interphase region is modeled. Similar to the example in Section 6.3.1, the radius parameter is interpolated. The shape parameters of the ellipsoidal surfacelet are  $r_1 = 1.7$ ,  $r_2 = 9$ , and  $r_3 = 3$ . The identified position and orientation of the particle are  $\alpha = 0.5712$ ,  $\beta = 0.0873$ , and  $b = -0.4724$ .



Four isosurfaces with golden-ratio radius distribution are specified. They are 255, 193, 100 and 32 respectively. The user-specified isosurfaces for an ellipsoidal particle are shown in Figure 98. After the surfacelet transform, the surfacelets for the isosurfaces are obtained, as shown in Figure 99. After interpolation, the intermediate isosurfaces with interpolated surface integrals are obtained. The result is shown as the hollow circles in Figure 100. With the inverse surfacelet transform, the resulting images of the interpolation can be obtained, as shown in Figure 101. As seen in the result, there are only 5 additional points required to specify the distribution in the domain. However, in the bi-sectional example in Section 6.3.1, 15 additional are needed to interpolate the boundary region. Therefore, the golden-ratio grid scheme requires few evaluation points from the interpolated distribution model to specify the distribution in the domain.

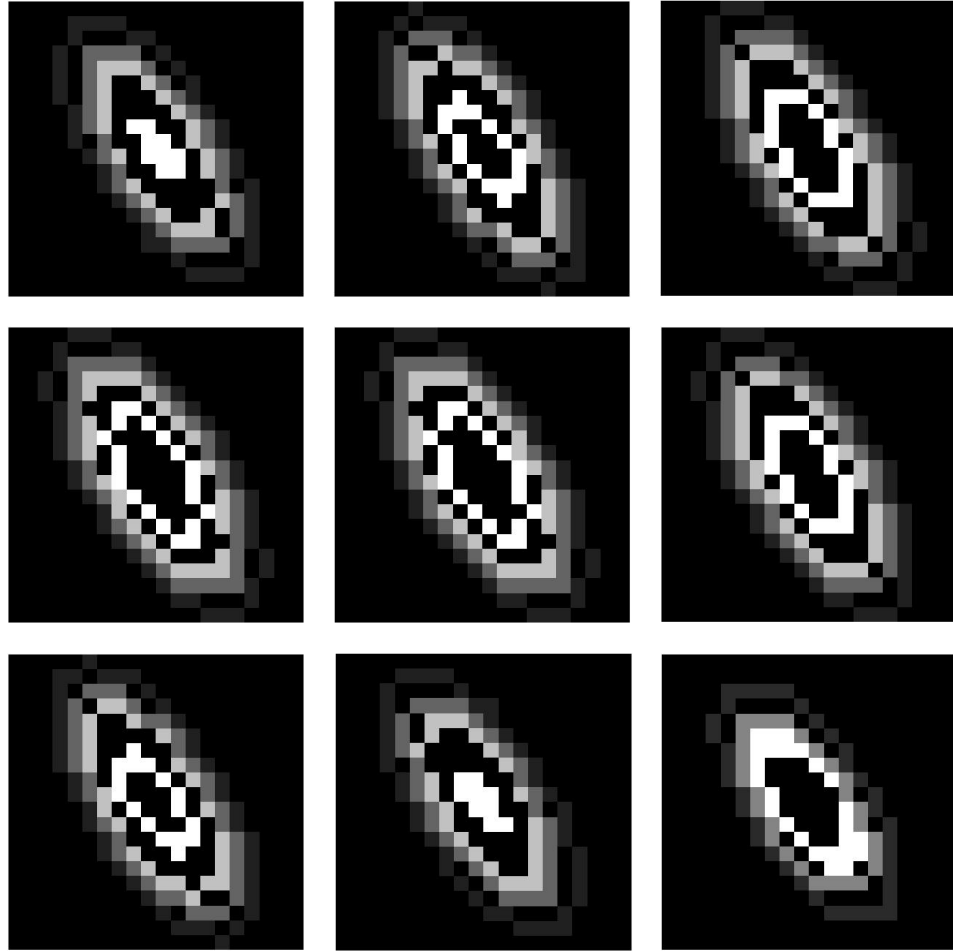


Figure 98 The user-specified isosurfaces for an ellipsoidal particle

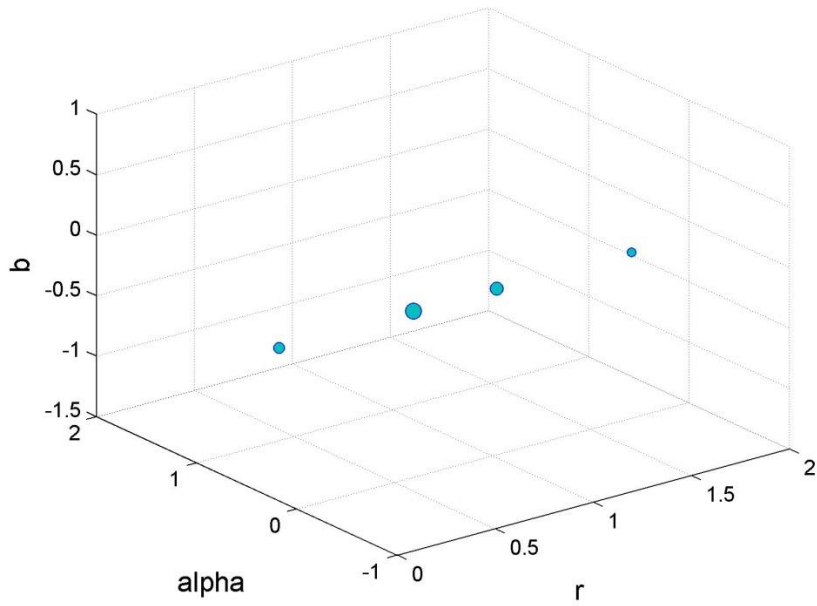


Figure 99 The user-specified isosurfaces in the surfacelet space with golden-ratio grids

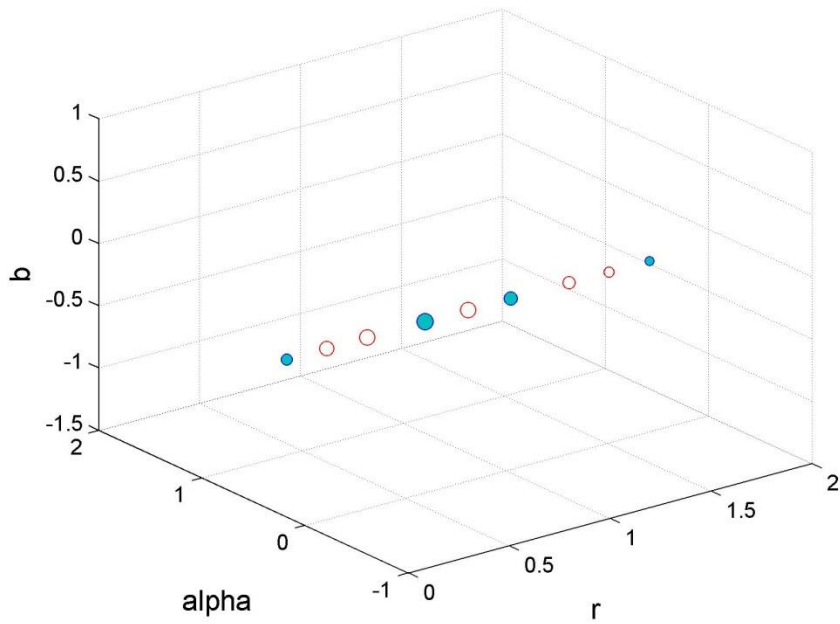


Figure 100 The interpolation of surface integrals with golden-ratio grids

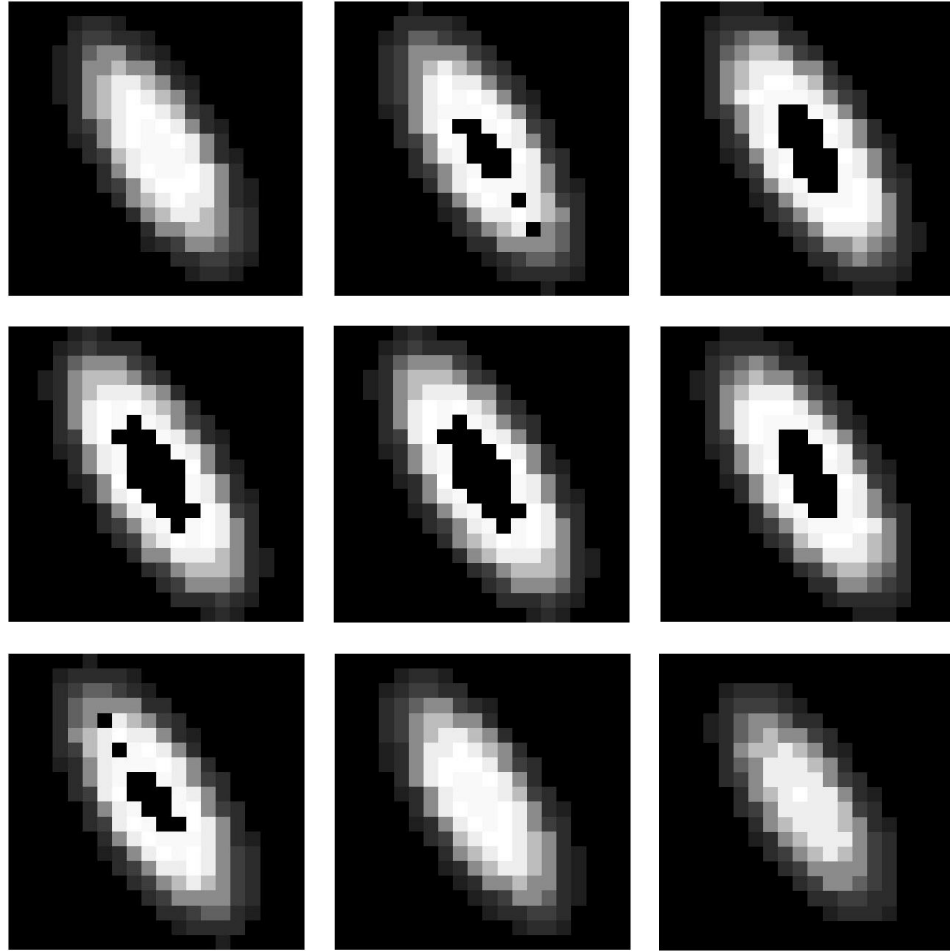


Figure 101 The resulting image of the specification process

#### ***6.4 A Property-Oriented Materials Design Process based on the Proposed Specification Scheme***

The ultimate goal of the multi-scale material specification method proposed in the previous sections of this chapter is to provide a geometry-material composition distribution design specification tool. This design specification tool is supposed to be integrated with prediction methods or tools for physical properties of material so that engineers are able to design materials based on the desired material properties. In this

section, a concept of property-oriented materials design and reverse engineering processes is proposed based on the developed specification scheme.

#### **6.4.1 The general process of property-oriented materials design**

The general process of property-oriented materials design should be a closed-loop process so that the design result can be evaluated in terms of the physical properties and direct the modification of the material microstructures and compositions. The flow chart of the process is shown in Figure 102, and the detailed steps are explained as follows.

First of all, based on the desired material properties and prior knowledge of the general microstructure-property relationship, the multi-scale material design is conducted such that the material microstructures and compositions can be created. It has been demonstrated that this step can be done with the proposed method in the previous sections of this chapter. The outputs of this step are 3D material images showing the material microstructures and compositions.

In the second step, based on these 3D images, the effective physical properties are predicted. The corresponding methods of prediction will be discussed in Section 6.4.2.

In the third step, the difference between the desired properties and the effective properties of the designed materials are evaluated. If the difference is satisfied, the design process is complete, and the resulting surfacelet model is the output of the process. Otherwise, if the difference is unsatisfied, the microstructures and compositions are modified, and the prediction of properties and evaluation are conducted again. This process is iterated until the result is satisfied.

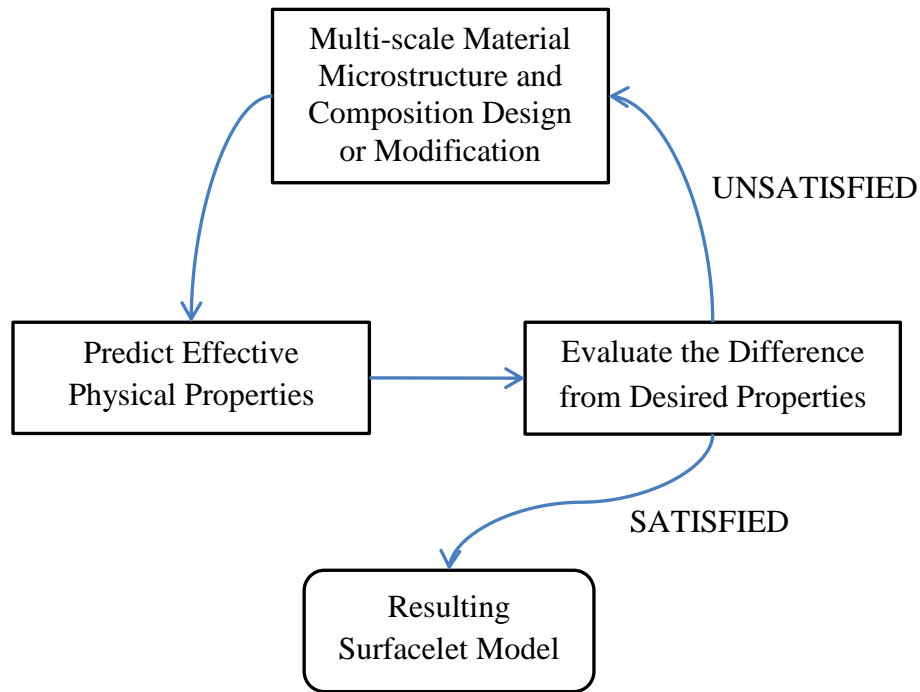


Figure 102 A property-oriented materials design process

The reverse engineering process is aimed at the modification of existing materials. Therefore, the initial surfacelet model of the design process is not created by the users. Instead, it is constructed from the 3D images of existing materials. The flow chart of the process is shown in Figure 103, and the detailed steps are explained as follows.

First of all, 3D material imaging is conducted so that 3D material images can be obtained. This step is also called material characterization.

In the second step, the 3D images are preprocessed. This may include the decomposition of the original 3D images to component images so that the relative compositions of multiple material components can be obtained.

In the third step, the surfacelet transform is conducted so that the surfacelet model of the existing materials is constructed as the initial model of the design process.

In the last step, the property-oriented material design process, as described at the beginning of this section is conducted.

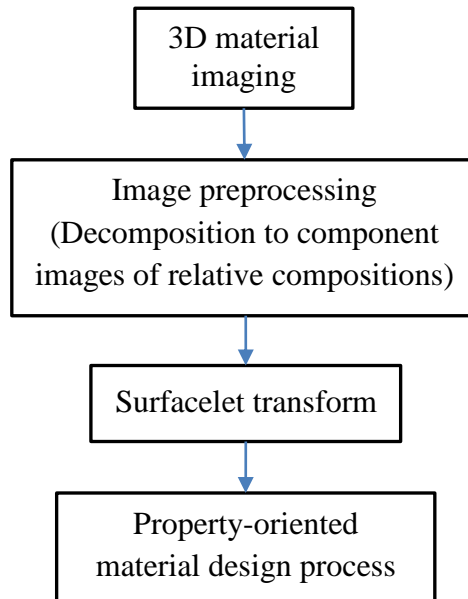


Figure 103 The reverse engineering of the design process

#### **6.4.2 Prediction of effective physical properties of heterogeneous materials**

In the proposed general process of property-oriented materials design, once the 3D material images are obtained from the multi-scale material design, theoretical prediction of effective properties is conducted. The effective physical properties of heterogeneous materials can be conducted either by analytical models or Finite Element Analysis (FEA).

##### **6.4.2.1 Analytical method**

In material physical properties, some are structure-sensitive, such as yield strength, while others are structure-insensitive such as elastic constants. Some properties of composites are linearly dependent on the mass or volume fraction, such as elastic modulus and conductivity, while others are nonlinearly dependent, such as strength. For


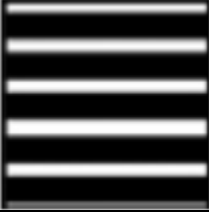

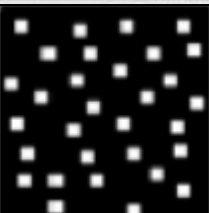


the structure-insensitive properties, some existing analytical models for effective properties of two-component materials are shown in Table 19 [111]. In this table,  $\lambda_1$  is the property of the continuous phase,  $\lambda_2$  the property of the dispersed phase,  $\lambda_e$  the corresponding effective property,  $\phi$  the volume fraction of the dispersed phase,  $\alpha$  the property ratio ( $\alpha = \lambda_2 / \lambda_1$ ),  $n$  the shape factor of the dispersed phase.

#### 6.4.2.2 Numerical method

Besides analytical models, numerical methods, such as FEA, can also be done to compute the physical properties of materials based on 3D images. Lewis et al. [112] generated an FEA mesh that consists of eight-node brick elements, with each element corresponding to one voxel in the sampled microstructure. This method will be utilized in the FEA of 3D material images designed with the proposed method in the previous sections of this chapter.



Table 19 Existing analytical models for effective properties of two-component materials

Model	Microstructure Schemes	Expression
Parallel model		$\lambda_e = (1 - \phi)\lambda_1 + \phi\lambda_2$
Series model		$\lambda_e = \left[ \frac{1 - \phi}{\lambda_1} + \frac{\phi}{\lambda_2} \right]^{-1}$
EMT model		$(1 - \phi) \frac{\lambda_1 - \lambda_e}{\lambda_1 + 2\lambda_e} + \phi \frac{\lambda_2 - \lambda_e}{\lambda_2 + 2\lambda_e} = 0$
Maxwell model		$\frac{\lambda_e}{\lambda_1} = 1 + \frac{3(\alpha - 1)\phi}{(\alpha + 2) - (\alpha - 1)\phi}$
Hamilton model		$\frac{\lambda_e}{\lambda_1} = \frac{\alpha + (n - 1) + (n - 1)(\alpha - 1)\phi}{\alpha + (n - 1) + (1 - \alpha)\phi}$
Reciprocity model		$\frac{\lambda_e}{\lambda_1} = \frac{1 + (\sqrt{\alpha} - 1)\phi}{1 + (\sqrt{1/\alpha} - 1)\phi}$

## ***6.5 Discussions and Future Work***

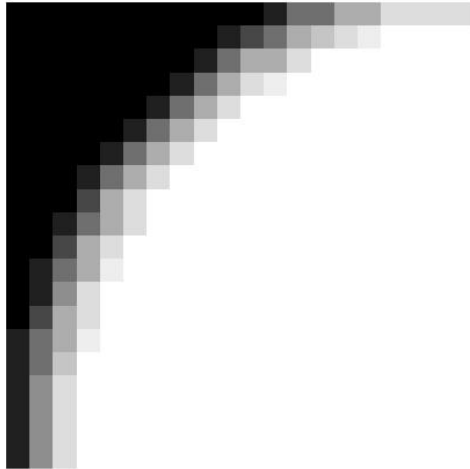
In this chapter, a multi-scale materials modeling and specification scheme is proposed for design and visualization of material microstructures at multiple levels of details. The combination of the visual and model zooming mechanism is able to support seamless zoom-in and zoom-out operations. The two-scale zoom-in method is developed based on collocation in the surfacelet space. A golden-ratio grid mechanism is proposed to reduce the percentage of additional new grid points. Two collocation schemes of bisectional and golden-ratio grids are demonstrated with an example of the design of fiber-based composite microstructure, and an example of the interphase region of an ellipsoidal particle. The proposed method is general enough for all zoom-in operations during the design process. This method allows for seamless zooming operations without the artificial separation of scales.

The surfacelets created for the main microstructural features at the beginning of the design process can not only be specified by users, but also be obtained from the forward surfacelet transform of existing material images. Therefore, this proposed multi-scale material modeling method also supports the reverse engineering process.

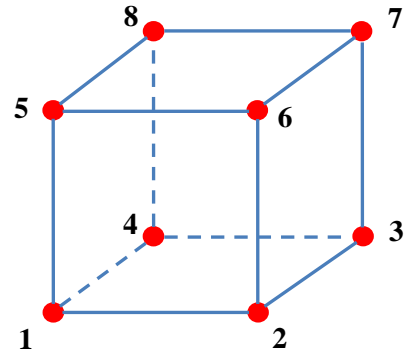
For a complete materials design based on the proposed specification scheme, a concept of property-oriented materials design and reverse engineering processes is also proposed. As a key step in the two processes, the methods for the prediction of effective physical properties of heterogeneous materials, including analytical models and the FEA method, are introduced.

The future extension of this work will include: 1) The design process with the collocation in 2D and other higher dimensions in the surfacelet domain will be

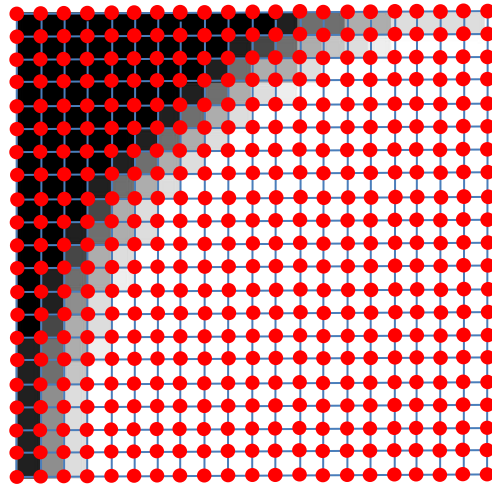
implemented and tested. 2) The deformation of microstructures will also be modeled. 3) The entire design process will be implemented, especially for the FEA portion. The planned scheme of the mesh is shown in Figure 104. 4) With the consideration of process uncertainty, stochasticity or randomness can be introduced into the location and orientation parameters of surfacelets. The sensitivity and robustness of materials properties with respect to the variations need to be assessed.



(a) A slice of an example 3D material image designed with the proposed method in this chapter



(b) An eight-node brick element



(c) The FEA mesh with each eight-node brick element corresponding to one voxel in the designed 3D material image (shown in 2D)

Figure 104 The FEA mesh of an example 3D material image designed with the proposed method in this chapter

## CHAPTER 7

### CONCLUSION AND FUTURE WORK

#### *7.1 Summary of the Dissertation*

This dissertation provides the conceptual and theoretical foundation for a future multi-scale materials design tool that design engineers, analysts, manufacturers, materials scientists, and others can all use. The concepts and theories in this dissertation also enable an integrated CAD/CAE/CAM environment where every artifact that is designed is physically meaningful. This integration will consequently enhance the scientific and technological understanding of the future CAD systems. As such, this dissertation contributes to the Material Genome Initiative (MGI) launched by the White House in June 2011 in the aspects of Computational tools and Digital data.

Specifically, four enabling techniques for surfacelet-based multi-scale heterogeneous materials modeling are developed. First, a method of inverse surfacelet transform is developed such that the original images can be reconstructed from the surfacelets. The prior knowledge of material properties and distributions is applied to solve the under-constrained problems. The coupled forward and inverse surfacelet transform also provides a new method of image compression with an approximately 50% compression rate. Second, composite surfacelets with the combinations of different types of primitive surfacelets are created to increase the flexibility of the surfacelet transform with potentially fewer surfacelets and improved reconstruction accuracy by the capability of identifying complex feature geometries. Third, a general method of approximating material composition and local property distributions with surfacelets is proposed based on the feature identification result of the 3D material images, and wavelet approximation

of the material composition or local property distributions. Fourth, a multi-scale materials modeling method is proposed to support interactive design and visualization of material microstructures at multiple levels of details. The combination of the visual and model zooming mechanism is able to support seamless zoom-in and zoom-out operations. The two-scale zoom-in method is developed based on collocation in the surfacelet space. An example of the design of fiber-based composite microstructure is demonstrated. The proposed method is general enough for all zoom-in operations during the design process. In addition, the scheme of a property-oriented materials design process is also proposed.

## ***7.2 Contributions of the Dissertation***

The technical contributions of this work include:

- A general method of geometric feature identification from 3D material images based on the largest surface integrals is proposed. With this method, the high-level geometric information can be extracted from material microstructural images.
- A method of image data compression based on the forward and inverse surfacelet transform is developed.
- A method of composite surfacelet for the identification of complex feature geometries is proposed.
- A general method of approximating material composition and local property distributions with surfacelets is proposed for the reverse engineering of materials design.
- A generic multi-scale materials modeling method is proposed to support interactive design specification and visualization of material microstructures at multiple levels of details with seamless zooming capability.

### **7.3 Future Work**

#### **7.3.1 Further image compression based on the feasibility of interpolation and extrapolation in the surfacelet space**

It has been demonstrated in Section 6.1.1 that when the interpolation or extrapolation is conducted in the surfacelet space, surface integrals can be well approximated with small errors. It is therefore used in the multi-scale materials design process to generate unspecified surfacelets. In future, this technique will be utilized for the prediction of surface integrals in the inverse surfacelet transform process so that less surfacelets can be used to reconstruct 3D images. This is expected to lead to higher data compression rate.

#### **7.3.2 Multiscale material modeling with multiscale wavelet approximation**

It has been demonstrated in Chapter 5 that surfacelets are able to model the material local property distributions through wavelet approximation. It should be noted that, as stated in Section 1.4, one of the main reasons why wavelet is chosen to construct the surfacelet is that wavelet is multiscale by nature. That is, at larger scales, less wavelets are used for approximation with lower accuracy to show less detailed or global distribution; whereas, at smaller scales, more wavelets are used for approximation with higher accuracy to show more detailed or local distribution. It is desirable that this multiscale nature is utilized in multiscale material modeling. However, in Chapter 5, the wavelet approximation and the resulting surfacelet approximation are only at one single scale, instead of multiple scales. More detailed research and implementation of this idea is not covered in this dissertation. In future, a multiscale material modeling method based

on the feature identification result will be developed, and applied to the same example in Chapter 5.



## REFERENCES

---

- [1] <http://www.whitehouse.gov/mgi>
- [2] G. B. Olson., Computational design of hierarchically structured materials, (1997), *Science*, vol. 277, pp.1237–42
- [3] J. Burress, Solution-Processed Graphene/MnO<sub>2</sub> Nanostructured Textiles for High-Performance Electrochemical Capacitors, *NanoViews.com*, 2011
- [4] Y. Wang, D. W. Rosen, Multiscale heterogeneous modeling with surfacelets, (2010), *Computer-Aided Design and Applications*, vol. 7, pp. 759-776
- [5] D. Donoho, Wedgelets: nearly minimax estimation of edges, (1999), *The Annals of Statistics*, vol. 27, issue 3, pp. 895-897
- [6] E. J. Candès and D. L. Donoho, Recovering edges in ill-posed inverse problems: optimality of curvelet frames, (2002), *The Annals of Statistics*, vol. 30, issue 3, pp.784-842
- [7] E. J. Candès, Ridgelets: theory and applications, (1998), Ph.D. dissertation, Stanford University.
- [8] M. N. Do and M. Vetterli, (2005), The contourlet transform: an efficient directional multiresolution image representation, *IEEE Trans. Image Processing*, vol. 14, issue 12, pp. 2091-2106
- [9] D. L. Donoho and X. Huo, Beamlets and multiscale image analysis, (2001), In T.J. Barth, T. Chan, and R. Haimes (Eds.), *Multiscale and Multiresolution Methods: Theory and Applications* (Springer), pp.149-196
- [10] X. Huo. Beamlets and multiscale modelling, (2005), Entry for the 2nd Edition of *Encyclopedia of Statistical Sciences*, Eds. C. B. Read, N. Balakrishnan, and B. Vidakovic, Wiley & Sons, NJ
- [11] R. M. Willett and R.D. Nowak, Platelets: a multiscale approach for recovering edges and surfaces in photon-limited medical imaging, (2003), *IEEE Trans. Medical Imaging*, vol. 22, issue 3, pp. 332-350
- [12] L. Ying, L. Demanet and Candès, E, 3D discrete curvelet transform, (2005), *Proc. SPIE Conf. Wavelet Applications in Signal & Image Processing*, San Diego, CA, vol. 5914, pp.591413
- [13] Y. M. Lu and M. N. Do, Multidimensional directional filter banks and surfacelets, (2007), *IEEE Trans. Image Processing*, vol. 16, issue 4, pp. 918-931
- [14] Chandrasekaran, V., Wakin, M.B., Baron, D., and Baraniuk, R.G. Representation and compression of multidimensional piecewise functions using surflets, (2009) *IEEE Trans. Information Theory*, vol. 55, issue 1, pp. 374-400
- [15] Radon J, Parks PC (translator), On the determination of functions from their integral values along certain manifolds, (1986), *IEEE Transactions on Medical Imaging*, vol. 5, issue 2, pp. 170–176
- [16] D. Juul Jensen, E. M. Lauridsen, L. Margulies, H. F. Poulsen, S. Schmidt, H. O. Sorensen, G. B. M, Vaughan X-ray microscopy in four dimensions, (2006), *Mater Tod* vol. 9, pp.18–25

- 
- [17] G. E. Ice, X-ray microtomography, (2004), In: Vander Voort GF (ed) ASM Handbook, vol. 9, Metallography and Microstructure, ASM International, Materials Park, OH, pp. 461–464
- [18] T. Link, S. Zabler, A. Epishin, A. Haibel, M. Bansal, X. Thibault, (2006), Synchrotron tomography of porosity in single-crystal nickel base superalloys. *Mat Sci Eng A*, vol. 425, pp. 47–54
- [19] S. Schmidt, S. F. Nielsen, C. Gundlach, L. Margulies, X. Huang, and D. Juul Jensen, Watching the growth of bulk grains during recrystallization of deformed metals, (2004), *Science*, vol. 305, pp. 229–232
- [20] W. Ludwig, P. Reischig, A. King, M. Herbig, E.M. Lauridsen, G. Johnson, T.J. Marrow, J.Y. Buffiere, Three-dimensional grain mapping by x-ray diffraction contrast tomography and the use of Friedel pairs in diffraction data analysis. (2009), *Rev Sci Instrum* vol. 80, issue 3, 033905
- [21] B. C. Larson, W. Yang, G. E. Ice, J. D. Budai, J. Z. Tischler, Three-dimensional X-ray structural microscopy with submicrometre resolution, (2002), *Nature*, vol. 415, pp. 887–890
- [22] G. E. Ice, J. W. L. Pang, R. I. Barabash, Y. Puzrev, Characterization of three-dimensional crystallographic distributions using polychromatic X-ray microdiffraction, (2006), *Scripta Mater*, vol. 55, pp. 57–62
- [23] O. Forsman, Undersökning av rymdstrukturen hos ett kolst<sup>o</sup>a av hypereutektoid sammansättning. (1918), *Jernkontorets Ann.*, vol. 102, pp. 1–30
- [24] A. C. Lewis, A.B. Geltmacher, Image-based modeling of the response of experimental 3D microstructures to mechanical loading, (2006), *Scripta Mater*, vol. 55, pp. 81–85
- [25] R. C. Gonzalez, R. E. Woods, *Digital Image Processing*, 2nd Ed.; Addison-Wesley: Reading, Massachusetts, 2002
- [26] L. A. Shepp and B. F. Logan, The Fourier reconstruction of a head section, (1974), *IEEE Trans. Nucl. Sci.*, vol. NS-21, pp. 21–43
- [27] C. L. Byrne and R. M. Fitzgerald, Reconstruction from partial information, with applications to tomography, (1982), *SIAM J. Appl. Math.*, vol. 42, pp. 933–940
- [28] C. L. Byrne, R. M. Fitzgerald, M. A. Fiddy, T. J. Hall, and A. M. Darling, (1983), Image restoration and resolution enhancement, *J. Opt. Soc. Am.*, vol. 73, pp. 1481–1487
- [29] R. Aster, B. Borchers, and C. Thurber, (2012), *Parameter Estimation and Inverse Problems*, Second Edition, Elsevier
- [30] A. N. Tikhonov, Solution of incorrectly formulated problems and the regularization method, (1963), *Soviet Math. Dokl.*, vol. 4, pp. 1035–1038
- [31] H. W. Engl, M. Hanke and A. Neubauer, *Regularization of Inverse Problems*, Kluwer, Dordrecht 1996.
- [32] M. Hanke, *Conjugate Gradient Type Methods for Ill-Posed Problems*, Pitman Res. Notes Math., Longman, Harlow, Essex, 1995
- [33] M. Hanke and M. P. C. Hansen, Regularization methods for large-scale problems, (1993), *Surveys Math. Indust.* vol. 3, pp. 253–315

- 
- [34] P. C. Hansen, Analysis of discrete ill-posed problems by means of the L-curve, (1992), *SIAM Review*, vol. 34, issue 4, pp. 561–580
- [35] P. C. Hansen, Rank-Deficient and Discrete Ill-Posed Problems. Numerical Aspects of Linear Inversion, SIAM, Philadelphia 1997
- [36] A. Neumaier, Solving ill-conditioned and singular linear systems: A tutorial on regularization, (1998), *SIAM Review*, vol. 40, issue 3, pp. 636–666
- [37] G. L. Zeng, Image reconstruction - a tutorial, (2001), *Computerized Medical Imaging and Graphics*, vol. 25, issue 2, pp. 97–103
- [38] G. T. Herman and L. B. Meyer, Algebraic Reconstruction Techniques Can Be Made Computationally Efficient, (1993), *IEEE Transactions on Medical Imaging*, vol. 12, issue 3, pp. 600–609
- [39] K. Mueller, R. Yagel, J. J. Wheller, Fast implementations of algebraic methods for three-dimensional reconstruction from cone-beam data, (1999), *IEEE Transactions on Medical Imaging*, vol. 18, issue 6, pp. 538–48
- [40] K. Mueller, R. Yagel, J. J. Wheller, Anti-Aliased 3D Cone-Beam Reconstruction Of Low Contrast Objects With Algebraic Methods, (1999), *IEEE Transactions on Medical Imaging*, vol. 18, issue 6, pp. 519–537
- [41] H. M. Shieh C. L. Byrne, M. E. Testorf, M. A. Fiddy, Iterative image reconstruction using prior knowledge, (2006), *J. Opt. Soc. Am. A*, vol. 23, issue 6, pp. 1292–300
- [42] A. J. Rockmore and A. Macovski, Maximum likelihood approach to emission image-reconstruction from Projections, (1976), *IEEE Trans. Nucl. Sci.* vol. 23, issue 4, pp. 1428–32
- [43] A. J. Rockmore and A. Macovski, Maximum likelihood approach to transmission image-reconstruction from projections, (1977), *IEEE Trans. Nucl. Sci.* vol. 24, pp. 1929–35
- [44] L. S. Shepp and Y. Vardi, Maximum-likelihood reconstruction for emission tomography, (1982), *IEEE Transactions on Medical Imaging*, vol. MI-1, pp. 113–122
- [45] K. Lange and R. Carson, EM reconstruction algorithms for emission and transmission tomography, (1984), *J. Comput. Assist. Tomogr.*, vol. 8, pp. 306–316
- [46] D. Geman and D. E. McClure, Bayesian image analysis: an application to single photon emission tomography, (1985), *Proc. Stat. Comput. Section, Amer. Stat. Assoc.*
- [47] J. Wang, T. F. Li and L. Xing, Iterative image reconstruction for CBCT using edge-preserving prior, (2009), *Med. Phys.* vol. 36, issue 1, pp. 252–260
- [48] M. Goitein, Three-dimensional density reconstruction from a series of two-dimensional projections, (1972), *Nucl. Instrum. Methods*, vol. 101, pp. 509–518
- [49] T. F. Budinger and G. T. Gullberg, Three-dimensional reconstruction in nuclear medicine emission imaging, (1974), *IEEE Trans. Nucl. Sci.*, vol. 21, issue 3, pp. 2–20
- [50] J. Qi and R. M. Leahy, Iterative reconstruction techniques in emission computed tomography, (2006), *Physics In Medicine And Biology*, vol. 51 pp. 541–578
- [51] K. Sauer and C. Bouman, A local update strategy for iterative reconstruction from projections, (1993), *IEEE Trans. Signal Process.* vol. 41, pp. 534–548

- 
- [52] C. Bouman and K. Sauer, A unified approach to statistical tomography using coordinate descent optimization, (1996), *IEEE Trans. Image Process.* vol. 5, pp. 480–92
- [53] J. A. Fessler, E. P. Ficaro, N. H. Clinthorne and K. Lange, Grouped-coordinate ascent algorithms for penalized likelihood transmission image reconstruction, (1997), *IEEE Trans. Med. Imaging*, vol. 16, pp. 166–75
- [54] J. Zheng, S. S. Saquib, K. Sauer and C. A. Bouman, Parallelizable Bayesian tomography algorithms with rapid guaranteed convergence, (2000), *IEEE Transactions on Image Processing*, vol. 9, pp. 1745–59
- [55] A. P. Dempster, N. M. Laird and D. B. Rubin, Maximum likelihood from incomplete data via the EM algorithm, (1977), *J. R. Stat. Soc. Ser. B*, vol. 39, pp. 1–38
- [56] K. C. Tam and V. Perez-Mendez, Tomographical imaging with limited-angle input, (1981), *J. Opt. Soc. Amer.*, vol. 71, issue 5, pp. 582-592
- [57] J. A. Scales, Tomographic inversion via the conjugate gradient method, (1987), *Geophysics*, vol. 52, issue 2, pp. 179–185
- [58] S. Kawata and O. Nalcioglu, Constrained iterative reconstruction by the conjugate gradient method, (1985), *IEEE Transactions on Medical Imaging*, vol. MI-4, pp. 65-71
- [59] E. L. Piccolomini, F. Zama, Conjugate gradient regularization method in computed tomography problems, (1999), *Applied Mathematics and Computation*, vol. 102, issue 1, pp. 87–99
- [60] Y. Biraud, A new approach for increasing the resolving power by data processing, (1969), *Astron. Astrophys.*, vol. 1, pp. 124-127
- [61] B. R. Freiden, Image enhancement and restoration, in *Picture Processing and Digital Filtering*, T. S. Huang Eds. Berlin, Germany: Springer-Verlag, 1975
- [62] M. H. B. M. Shariff, A constrained conjugate gradient method and the solution of linear equations, (1995), *Computers Math Applic*, vol. 30, pp. 25–37
- [63] D. Ziou, S. Tabbone, Edge detection techniques: An overview, (1998), *International Journal of Pattern Recognition and Image Analysis*, vol. 8, issue 4, pp. 537–559
- [64] J. M. Park, Y. Lu, Edge detection in grayscale, color, and range images, (2008), *Wiley Encyclopedia of Computer Science and Engineering*, pp. 1-16
- [65] V. F. Leavers, J. F. Boyce, The Radon transform and its application to shape parameterization in machine vision, (1987), *Image and Vision Computing*, vol. 5, issue 2, pp.161-166
- [66] N. Jeong, D. W. Rosen, Y. Wang, (2013), A Comparison of surfacelet-based method for recognizing linear geometric features in material microstructure, *Proc. IDETC2013*, Portland, Oregon, DETC2013-13370, August 4-7
- [67] D. W. Rosen, N. Jeong, Y. Wang, A Method for Reverse Engineering of Material Microstructure for Heterogeneous CAD, (2013), *Computer-Aided Design*, vol. 45, issue 7, pp. 1068–1078
- [68] S. R. Niezgodna, S. R. Kalidindi, Applications of the phase-coded generalized Hough transform to feature detection, analysis, and segmentation of digital microstructures, (2010), *Computers, Materials, & Continua*, vol. 14, issue 2, pp.79-98

- 
- [69] X. Y. Kou, and S. T. Tan, (2007), Heterogeneous object modeling: A review. *Computer-Aided Design*, vol. 39, pp. 284-301
- [70] S. Bhashyam, K. H. Shin, and D. Dutta, An integrated CAD system for design of heterogeneous objects, (2000), *Rapid Prototyping Journal*, vol. 6, issue 2, pp. 119-135
- [71] O. Koenig and G. Fadel, Application of Genetic Algorithms in the Design of Multi-Material Structures Manufactured in Rapid Prototyping, *Proc. Solid Freeform Fabrication Symposium*, pp. 209-217, Austin, TX, August 9-11, 1999
- [72] Z. Wu, S. H. Soon, and L. Feng, NURBS-based Volume Modeling, (1999), *International Workshop on Volume Graphics*, pp. 321-330
- [73] V. Adzhiev, E. Kartasheva, T. Kunii, A. Pasko, and B. Schmitt, Hybrid Cellular-Functional Modeling of Heterogeneous Objects, (2002), *ASME J. of Computing and Information Science in Engineering*, vol. 2, pp. 312-322
- [74] V. Kumar, D. Burns, D. Dutta, and C. Hoffmann, A framework for object modeling, (1999), *Computer-Aided Design*, vol. 31, pp. 541-556
- [75] X. Qian and D. Dutta, (2003), Physics-based Modeling for Heterogeneous Objects, *ASME Transactions Journal of Mechanical Design*, vol. 125, pp. 416-427
- [76] H. Liu, T. Maekawa, N.M. Patrikalakis, E.M. Sachs, W. Cho, Methods for Feature-Based Design of Heterogeneous Solids, (2003), *Computer-Aided Design*, vol. 36, pp. 1141-1159
- [77] S. T. Tan, and Y. K. Siu, Source-based heterogeneous solid modeling, (2002), *Computer-Aided Design*, vol. 44, issue 1, pp. 41-55
- [78] T. Martin, E. Cohen, R. M. Kirby, Volumetric parameterization and trivariate B-spline fitting using harmonic functions, (2009), *Computer Aided Geometric Design*, vol. 26, pp. 648-664
- [79] M. Ganter, J. Wahlborg, D. Schwartz, D. Storti, H-ISM: An Implementation of Heterogeneous Implicit Solid Modeling, *Proceedings of ASME Design Automation Conference*, paper #DETC2002/DAC-34139, Montreal, Sept 29 – Oct. 2, 2002.
- [80] V. L. Rvachev, T. I. Sheiko, V. Shapiro, I. Tsukanov, Transfinite Interpolation over Implicitly Defined Sets, (2001), *Computer-Aided Geometric Design*, vol. 18, pp. 195-220
- [81] A. Pratap and R.H. Crawford, Implementation of a Functionally Gradient Material modeling and Design System, *Proc. Solid Freeform Fabrication Symposium*, pp. 150-161, Austin, TX, Aug. 4-6, 2003
- [82] J. H. Panchal, S. R. Kalidindi, D. McDowell, Key computational modeling issues in Integrated Computational Materials Engineering, (2013), *Computer-Aided Design*, vol. 45, issue 1, pp. 4-25
- [83] D. T. Fullwood, S. R. Niezgoda, B. L. Adams, S. R. Kalidindi, Microstructure sensitive design for performance optimization, (2010), *Progress in Materials Science*, vol. 55, pp. 477–562
- [84] S. R. Niezgoda, Y. C. Yabansu, S. R. Kalidindi, Understanding and visualizing microstructure and microstructure variance as a stochastic process, (2011), *ActaMaterialia*, vol. 59, pp. 6387–400

- 
- [85] B. L. Adams, A. Henrie, B. Henrie, M. Lyon, S. R. Kalidindi, H. Garmestani, Microstructure-sensitive design of a compliant beam, (2001), *Journal of the Mechanics and Physics of Solids*, vol. 49, pp. 1639–1663
- [86] G. Saheli, H. Garmestani, and B. L. Adams, Microstructure design of a two phase composite using two-point correlation functions, (2004), *Journal of Computer-Aided Materials Design*, vol. 11, issue 2-3, pp. 103-115
- [87] B. L. Adams, G. Xiang, S. R. Kalidindi, Finite approximations to the second-order properties closure in single phase polycrystals, (2005), *Acta Materialia*, vol. 53, pp. 3563–77
- [88] G. Proust, S. R. Kalidindi, Procedures for construction of anisotropic elastic-plastic property closures for face-centered cubic polycrystals using first-order bounding relations, (2006), *Journal of the Mechanics and Physics of Solids*, vol. 54, pp.1744–62
- [89] M. Baniassadi, H. Garmestani, D. S. Li, S. Ahzi, M. Khaleel, and X. Sun, Three-phase solid oxide fuel cell anode microstructure realization using two-point correlation functions, (2011), *Acta materialia*, vol. 59, issue 1, pp. 30-43
- [90] G. Jefferson, H. Garmestani, R. Tannenbaum, A. Gokhale, E. Tadd, Two-point probability distribution function analysis of Co-polymer nano-composites, (2005), *International journal of plasticity*, vol. 21, issue 1, pp. 185-198
- [91] J. R. Houskamp, G. Proust, S. R. Kalidindi, Integration of microstructure-sensitive design with finite element methods: elastic-plastic case studies in FCC polycrystals, (2007), *International Journal for Multiscale Computational Engineering*, vol. 5, pp. 261–272
- [92] M. Knezevic, S. R. Kalidindi, R. K. Mishra, Delineation of first-order closures for plastic properties requiring explicit consideration of strain hardening and crystallographic texture evolution, (2008), *International Journal of Plasticity*, vol. 24, pp. 327–42
- [93] D. T. Fullwood, B. L. Adams, S.R. Kalidindi, Generalized Pareto front methods applied to second-order material property closures, (2007), *Computational Materials Science*, vol. 38, pp. 788–99
- [94] X. Wu, G. Proust, M. Knezevic, S. R. Kalidindi, Elastic-plastic property closures for hexagonal close-packed polycrystalline metals using first-order bounding theories, (2007), *Acta Materialia*, vol. 55, pp. 2729–37
- [95] J. B. Shaffer, M. Knezevic, S. R. Kalidindi, Building texture evolution networks for deformation processing of polycrystalline FCC metals using spectral approaches: applications to process design for targeted performance, (2010), *International Journal of Plasticity*, vol. 26, pp. 1183–94
- [96] T. Fast, S. R. Niezgod, S. R. Kalidindi, A new framework for computationally efficient structure-structure evolution linkages to facilitate high-fidelity scale bridging in multi-scale materials models, (2011), *Acta Materialia*, vol. 59, pp. 699–707
- [97] S. R. Kalidindi, S. R. Niezgod, G. Landi, S.Vachhani, A. Fast, A novel framework for building materials knowledge systems, (2009), *Computers Materials & Continua* vol.17, pp.103–26

- 
- [98] G. Landi, S. R. Kalidindi, Thermo-elastic localization relationships for multi-phase composites, (2010), *Computers, Materials & Continua*, vol. 16, pp. 273–93
- [99] G. Landi, S. R. Niezgoda, S. R. Kalidindi Multi-scale modeling of elastic response of three-dimensional voxel-based microstructure datasets using novel DFT-based knowledge systems, (2009), *ActaMaterialia*, vol. 58, pp. 2716–2725
- [100] T. Fast, S. R. Kalidindi, Formulation and calibration of higher-order elastic localization relationships using the MKS approach, (2011), *ActaMaterialia*, vol. 59, pp. 4595–605
- [101] Y. Liu, M. S. Greene, W. Chen, D. A. Dikin, W. K. Liu, Computational microstructure characterization and reconstruction for stochastic multiscale material design, (2013), *Computer-Aided Design*, vol. 45, issue 1, pp. 65–76
- [102] H. Xu, Y. Li, L. C. Brinson, W. Chen, Descriptor-based methodology for designing heterogeneous microstructure materials system, *Proc. ASME IDETC/CIE 2013*, Portland, Oregon, DETC2013-12232, August 4-7, 2013
- [103] K. Wu, M. J. Dijke, G. D. Couples, Z. Jiang, J. Ma, K. S. Sorbie, J. Crawford, I. Young, X. Zhang, 3D Stochastic Modelling of Heterogeneous Porous Media – Applications to Reservoir Rocks, (2006), *Transport in Porous Media*, vol. 65, issue 3, pp. 443–467
- [104] X. Y. Kou, S. T. Tan, Modeling Functionally Graded Porous Structures with Stochastic Voronoi Diagram and B-Spline Representations, (2010), *International Conference on Manufacturing Automation*, Hong Kong, China, pp. 99–106
- [105] M. H. B. M. Shariff, A constrained conjugate gradient method and the solution of linear equations, (1995), *Computers Math Applic*, vol. 30, issue 11, pp. 25–37
- [106] V. L. Rvachev. *Theory of R-functions and Some Applications*. (Naukova Dumka, 1982). In Russian.
- [107] V. Shapiro, Real functions for representation of rigid solids, (1994), *Computer Aided Geometric Design*, vol. 11, issue 2, pp. 153–175
- [108] K. Konopka, A. Olszówka-Myalska, M. Szafran, Ceramic–metal composites with an interpenetrating network, (2003), *Materials Chemistry and Physics*, vol. 81, issue 2–3, pp. 329–332
- [109] TEM image of nano-C60 particle, available at <http://www.britannica.com/EBchecked/media/137390/transmission-electron-microscopy-can-be-used-to-detect-and-characterize>.
- [110] Y. Gu, M. Li, J. Wang, Z. Zhang, Characterization of the interphase in carbon fiber/polymer composites using a nanoscale dynamic mechanical imaging technique, (2010), *Carbon*, vol. 48, issue 11, pp. 3229–3235
- [111] M. Wang, N. Pan, Predictions of effective physical properties of complex multiphase materials, (2008), *Materials Science and Engineering*, vol. 63, pp. 1–30
- [112] [http://www.nrl.navy.mil/content\\_images/10\\_FA2.pdf](http://www.nrl.navy.mil/content_images/10_FA2.pdf)

## VITA

### WEI HUANG

Wei was born in Yantai, Shandong Province, China. He received a B.S. in 2007 and a M.S. in 2010 both in Mechanical Engineering from Beihang University (BUAA), Beijing, China before coming to Georgia Tech to pursue a doctorate in Mechanical Engineering.

### PUBLICATIONS DURING PH.D. STUDY

**Wei Huang**, Yan Wang, David W. Rosen. “A Multi-scale Materials Design Method with Seamless Zooming Capability Based on Surfacelets”. 2014 ASME International Design Engineering Technical Conferences & The Computer and Information in Engineering Conference (IDETC2014), August 17-20, 2014, Buffalo, New York, Paper No. DETC2014-34435 (Accepted)

**Wei Huang**, Yan Wang, David W. Rosen. 2014, “Inverse Surfacelet Transform for Image Reconstruction with Constrained Conjugate Gradient Methods”. Journal of Computing and Information Science in Engineering. vol. 14, issue 2 (In Press)

**Wei Huang**, Sima Didari, Yan Wang, Tequila A.L. Harris, 2014, “Generalized Periodic Surface Model and Its application in Designing Fibrous Porous Media”. Engineering Computations: International Journal for Computer-Aided Engineering and Software. (In Press)

**Wei Huang**, Yan Wang, David W. Rosen. “Inverse Surfacelet Transform for Image Reconstruction with Prior Knowledge”. 2013 ASME International Design Engineering Technical Conferences & The Computer and Information in Engineering Conference (IDETC2013), Aug. 4-7, 2013, Portland, Oregon, Paper No. DETC2013-12739

**Wei Huang**, Yan Wang, Sima Didari, Tequila A.L. Harris, 2012, “Modeling Fibrous Porous Media with Periodic Surfaces”. Proceedings of TMCE 2012, Karlsruhe, Germany, vol. 1, issue 4, pp. 697-710

Sima Didari, Tequila. A.L. Harris, **Wei Huang**, Sean M. Tessier, Yan Wang, 2012, “Feasibility of Periodic Surface Models to Develop Gas Diffusion Layers: A Gas Permeability Study”, International Journal of Hydrogen Energy, vol. 37, issue 19, pp. 14427–14438

Sima Didari, Tequila. A.L. Harris, **Wei Huang**, Yan Wang, “Characteristics of the Gas Diffusion Layers’ Microstructure,” 2012 ASME 10<sup>th</sup> International Conference on Fuel Cell Science, Engineering and Technology, July 23-26, 2012, San Diego, California, Paper No. ESFuelCell2012-91438



Sima Didari, Tequila A.L. Harris, **Wei Huang**, Sean M. Tessier, Yan Wang, 2011, “Transport Phenomena in Carbon Paper Gas Diffusion Layers”, *Electrochemical Society Transactions*, vol. 41, issue 1, pp. 499-512

Sima Didari, **Wei Huang**, Sean M. Tassier, Yan Wang, Tequila A. L. Harris, “Numerical Prediction of Permeability Through Gas Diffusion Layers”, 220th The Electrochemical Society Meeting, October 9-14, 2011, Boston, Massachusetts, Abstract No. MA2011-02(16): 789